A Liquid-Shear-Stress Sensor Using Wafer-Bonding Technology

by

Kay-Yip Ng

B.S.E., University of Pennsylvania (1988)
B.S.Econ., University of Pennsylvania (1988)

Submitted to the Department of Electrical Engineering and Computer Science
in partial fulfillment of the requirements for the degree of

Master of Science

at the

MASSACHUSETTS INSTITUTE OF TECHNOLOGY

September 1990

Signature of Author ______________________________
Department of Electrical Engineering and Computer Science
September 4th, 1990

Certified by ______________________________ 9/6/90
Martin A. Schmidt
Assistant Professor of Electrical Engineering and Computer Science
Thesis Supervisor

Accepted by ______________________________
Arthur C. Smith
Chairman, Departmental Committee on Graduate Students

A Liquid-Shear-Stress Sensor Using Wafer-Bonding Technology

by

Kay-Yip Ng

Submitted to the Department of Electrical Engineering and Computer Science
on September 4th, 1990, in partial fulfillment of the
requirements for the degree of
Master of Science

Abstract

The development of a microfabricated shear-stress sensor suitable for use in a liquid environment is reported in this thesis. The design is targeted to measure shear-stresses in the range of 1kPa – 100kPa, at temperatures of up to 200°C and a hydrostatic pressure of up to 1MPa. A direct measurement method is used which consists of a $5\mu m$ thick silicon floating-element sized $120\mu m \times 120\mu m$ and suspended $1.4\ \mu m$ above the substrate by 4 tethers of dimensions $30\mu m \times 10\mu m$.

The transduction mechanism makes use of the silicon tethers acting as piezoresistors to detect the strain with metal interconnects routed out from the floating-element to bonding pads. Analytical calculations and finite-element analysis were used to study the mechanical response of the sensor. The sensors were fabricated using wafer-bonding technology and the device wafer was chemically thinned, resulting in a thin($5\mu m$) single-crystal-silicon film dielectrically isolated from the substrate. The process requires four mask steps and each chip has dimensions of 5.5mm × 4mm. A layer of amorphous silicon is deposited over the surface for passivation and to protect the aluminum lines during the release process. Diagnostic structures on the chip are used to determine the residual stress of the composite layer.

Cantilevers with patterned resistors were fabricated to measure the gage factors of dielectrically isolated piezoresistors at room temperature. Three types of silicon-on-insulator technologies were investigated: bonding and chemically etched wafers, bonding and mechanically polished wafers and zone-melt-recrystallized wafers.

Two categories of sensor testing are reported. An experiment was conducted to determine the structural integrity of the mechanical parts when exposed to elevated temperatures and pressures in an extruder. Testing done at 220°C and a pressure of 27MPa showed no damage to these structures. An experiment was also designed to calibrate the sensor in a cone-and-plate viscometer. A $400\mu V$ signal was detected for a shear-stress of 10kPa at room temperature.

Thesis Supervisor: Martin A. Schmidt

Title: Assistant Professor of Electrical Engineering and Computer Science

Acknowledgments

The completion of this thesis would not have been possible without the assistance and support of numerous individuals whom I would now like to acknowledge.

The faculty in the microsensors group not only introduced me to their field of expertise but were also instrumental in my professional development. Professor Martin Schmidt has provided key suggestions and advice in this work. As a thesis supervisor, he was patient during the many hours of discussions and created an environment conducive to research. The close interaction made the project interesting and enjoyable. Professor Stephen Senturia's teaching skills helped me think critically and integrated the understanding of science and technology with experimental skills.

Special thanks go to the people involved in the wafer-bonding process. Peter Gravesen and Theresa Lober did the necessary groundwork, Mike Huff qualified me on most of the equipment in the clean room, devoted a lot of his time refining the process and constructed the infrared characterization system and Dan Sobek was my lab partner during the bonding process. Wafer-thinning is a substantial part of the work and Vince McNeil provided a lot of technical expertise and helped me prepare some of the device wafers. He was also responsible for the general well being of the group laboratory and he carried out his responsibility diligently. Dr. Simon Wang of General Motors Research Laboratory was a source of help in the understanding of the theory behind chemical etching. Successful fabrication requires experience and thanks go to Mehran Mehregany who helped me overcome some of the obstacles. Craig Keast and David Volfson gave useful suggestions. Curtis Tsai was also kind enough to be my lab partner on some of those critical nights.

Other group members have contributed in some significant way. Aleks Nikolich helped in the backfilling experiment. Javad Shajii's assistance during the last month was invaluable. Jeff Pan, Mark Lubratt, Albert Young, Pinyen Lin and Bob Harris

helped in the presentation of this thesis. Scotti Fuller was efficient in sorting the paperwork and kept the office functioning systematically.

The sensor testing was done in the Combustion Laboratory in the Chemical Engineering Department and I am grateful to Sarakorn Gerjurasak and Professor Jack Howard for their generosity and assistance in the use of their equipment.

I would like to thank the staff of the Microsystems Technology Laboratory for maintaining the facility, especially Joe Walsh, Octavio Hurtado, Rob Cuikay, Brian Foley and Velma McClure.

This work has been sponsored by 3M and the 3M Sensor Fellowship. Dr. John Huizinga was helpful in providing information and collaborated in the failure testing. The Department of Justice funded the FEM work. The device wafers were provided by Jody Lapham and Susan Feindt of Analog Devices. Dr. Paul Zavracky of Kopin provided the ZMR wafers and Dr. John Matlock and Dr. T. Abe of SEH provided the mechanically polished wafers.

Through the years, my family has been a source of support and encouragement. My parents gave me the opportunity to come to the United States and protected me from the harsh realities of life so that I can concentrate on my studies. For my friend Pat, whose patience and understanding have been exceptional, I offer thanks as well. Finally, I thank God for his providence and faithfulness.

> The Lord has been mindful of us;
> He will bless us.
>
> Psalms 115:12

Contents

List of Figures

List of Tables

1

Introduction

This thesis reports on the development of a shear-stress microsensor suitable for elevated temperatures and pressures in a liquid environment. The device is a microfabricated version of a floating-element and represents an extension of the work done by Schmidt [1]. In this chapter, we will first discuss the nature of shear stresses in the context of a viscous flow, followed by a summary of the measurement techniques that are commonly employed, with particular emphasis on the floating-element. Finally, we will describe briefly the bonding and wafer-thinning process which is integral in the development of the sensor.

1.1 Shear Stresses in Fluids

In most applications of fluid mechanics a knowledge of the drag created by fluid flowing over a solid surface is essential to the understanding of the performance of a system whether it be a ship, an aircraft, or flow through a pipe. For a pipe flow, this drag or shear stress results in pressure losses and influences the design of the system. In some manufacturing environments, the shear stress is a parameter of interest for the purpose of process control since it gives an idea of the property of the fluid.

In order to describe shear stress in terms of the physical properties of a fluid, consider two large parallel plates of area A with a fluid (gas or liquid) contained between them (Figure 1-1). If the lower plate is set in motion in the x-direction at a constant velocity, the fluid gains momentum and attains a constant velocity profile, shown in the lower part of Figure 1-1. In order to maintain the constant velocity V

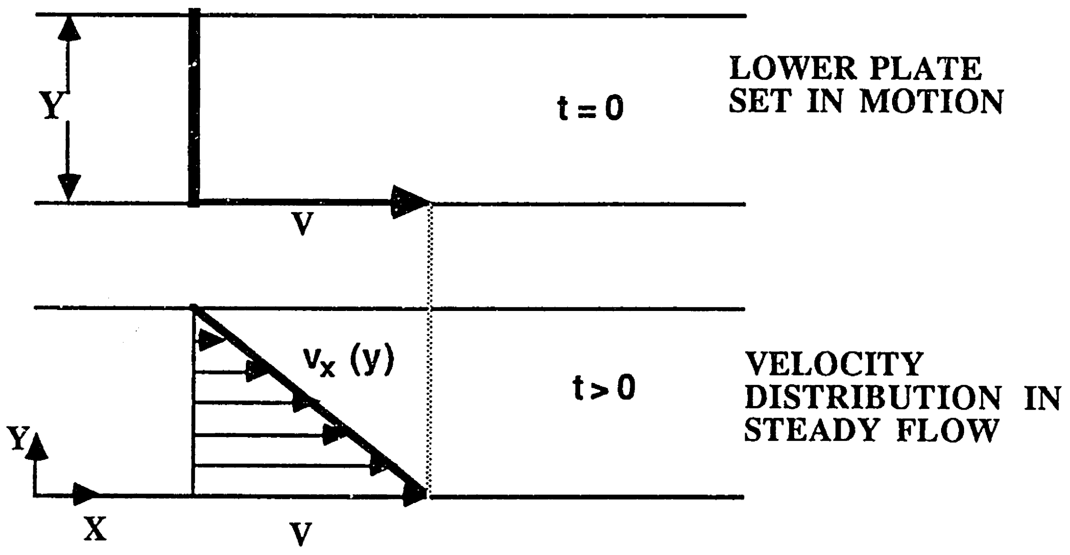

FIGURE 1-1: Velocity Profile of Fluid Contained Between Two Plates

of the plate, a force F is continuously applied to the plate. In laminar flow, the force may be expressed as

$$\frac{F}{A} = \mu \frac{V}{Y} \tag{1.1}$$

where μ is the fluid viscosity. $\frac{F}{A}$ is called the shear stress and in the illustration above is the stress exerted in the x-direction, written as τ_{yx}, the first subscript giving the direction of the normal of the plane in which it lies and the second subscript is the direction parallel to which it points. The velocity V is designated as v_x since it is the x-component of the fluid velocity. Equation 1.1 can also be rewritten as

$$\tau_{yx} = -\mu \frac{dv_x}{dy} \tag{1.2}$$

with the negative sign indicating that the momentum of flux is in the direction of the negative velocity gradient. If μ is a constant, the fluid is considered Newtonian but in general, μ is non-linear.

1.2 Methods of Measurements

A variety of techniques have been employed to measure the drag or skin friction such as

a) The Stanton tube

b) Thermal methods

c) The Preston tube

d) The sublayer fence

e) Electrochemical methods

f) Direct measurements

These methods are outlined below and are described in detail by Hanratty *et al* [2] and Winter [3]. The Stanton tube consists of a rectangular Pitot tube that has the wall of the pipe as one of its sides. The difference between the pressure measured with this Pitot tube and the static pressure is used to determine the velocity at the center of the tube.

A typical thermal method measurement consists of a heating element, for example nickel, placed near the wall. A current is passed through the strip and the power required to maintain a constant temperature is then related to the heat that is dissipated by the fluid flow from which the shear-stress is inferred.

The Preston tube consists of round Pitot tube resting on the inner wall of the pipe where measurement is made of the impact pressure of the fluid and the shear stress is indirectly determined.

A sublayer fence usually consists of a sharp edge projecting above the surface but still deep within the boundary layer. The difference in pressure before and behind the projection is related to the wall shear-stress. The advantage of this measurement is the ability to give readings for both forward and reverse flows due to the symmetry of the structure.

The direct measurement schemes are known as skin-friction balances or floating-element balances. A typical floating-element balance is shown in Figure 1-2. The local tangential force on a surface tends to displace the element and measurements are made of the displacement of the element or the force required to keep it in a

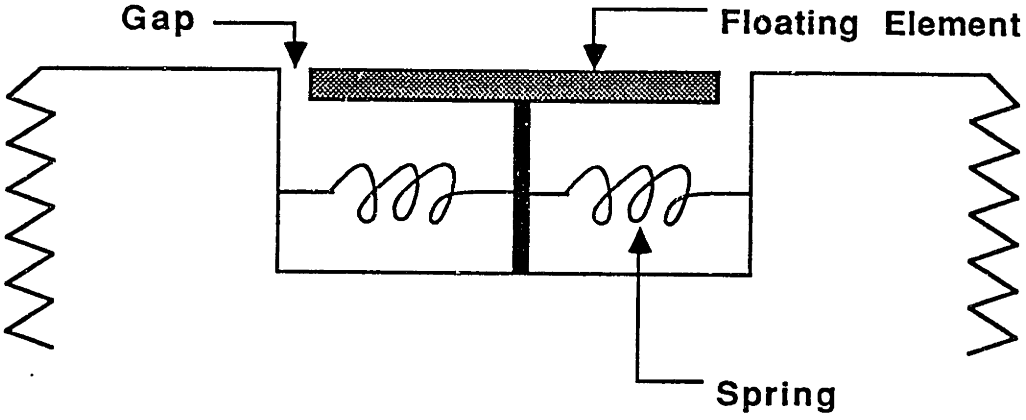

FIGURE 1-2: Floating-Element Balance.

null position. There are problems associated with this scheme that would result in erroneous measurements and they are summarized in the paper by Winter [3]. These include

a) The compromise between the requirement to measure local properties and the necessity of having an element of sufficient size that the force on it can be measured accurately

b) The effects of the necessary gaps around the floating element.

c) The effects of misalignment.

d) The forces arising from pressure gradients.

e) The effects of temperature changes.

f) The effects of leaks.

Nevertheless, most of these complications can be substantially removed by scaling down the size of the element and choosing a transduction mechanism which does not compromise the sensitivity. This motivates the development of a microfabricated version of the floating element. A microfabricated floating-element structure with integrated readout was first reported by Schmidt [1]. This sensor was calibrated in laminar flow using dry compressed air with measured sensitivity to below 1 Pa.

In this work, we would like to extend the capability of microfabricated floating elements to measurements of shear stresses in the range of 1 kPa - 100 kPa at temperatures of up to 300°C and to be tested in a liquid environment. To do so, we need to modify the structure of the element using single crystal silicon as the mechanical material instead of polyimide as was previously used and to choose another transduction mechanism for the provision of conductive liquids.

1.3 Wafer-Bonding and Etch-Back

In addition to the commonly available tools of microfabrication, the fabrication of this sensor requires wafer bonding, a relatively new technique, and wafer-thinning or etch-back. Both of these processes are introduced below but the actual process development issues are discussed in the chapter on fabrication.

1.3.1 Wafer-Bonding

Wafer bonding [4] is a technique whereby two mirror polished wafers are hydrated to form hydrophilic surfaces, brought together at room temperature and cycled to a high temperature to form a permanent bond. One of the wafers will have silicon dioxide grown thermally before the bonding process, thereby electrically isolating the wafers from each other. Figure 1-3 shows the cross section of the wafers before and after bonding. The wafer with the oxide grown on it is called the handle wafer while the other wafer is called the device wafer since the sensor will be formed on it. When the wafers are brought into contact at the end of the hydration step, Van der Waals forces caused by the mutual interaction of all the induced dipoles on both sides of the wafer result in an attractive force and keeps the wafer in contact. Haisma [5] has estimated that for a 1nm separation, this attractive bond strength is about $10^6 N/m^2$ between two 100mm wafers. After contacting, the wafers are placed in a furnace at $1000^o C$ in dry oxygen for an hour. Lasky[4] has proposed that at high temperatures, oxygen between the wafers is converted to SiO_2 and this transformation from a gaseous phase to a solid phase results in a partial vacuum and presses the wafers together even closer. Chemical reactions occur at the interface according to the reaction

$$\equiv SiOH + HOSi \equiv \rightarrow \equiv Si - O - Si \equiv + H_2O \tag{1.3}$$

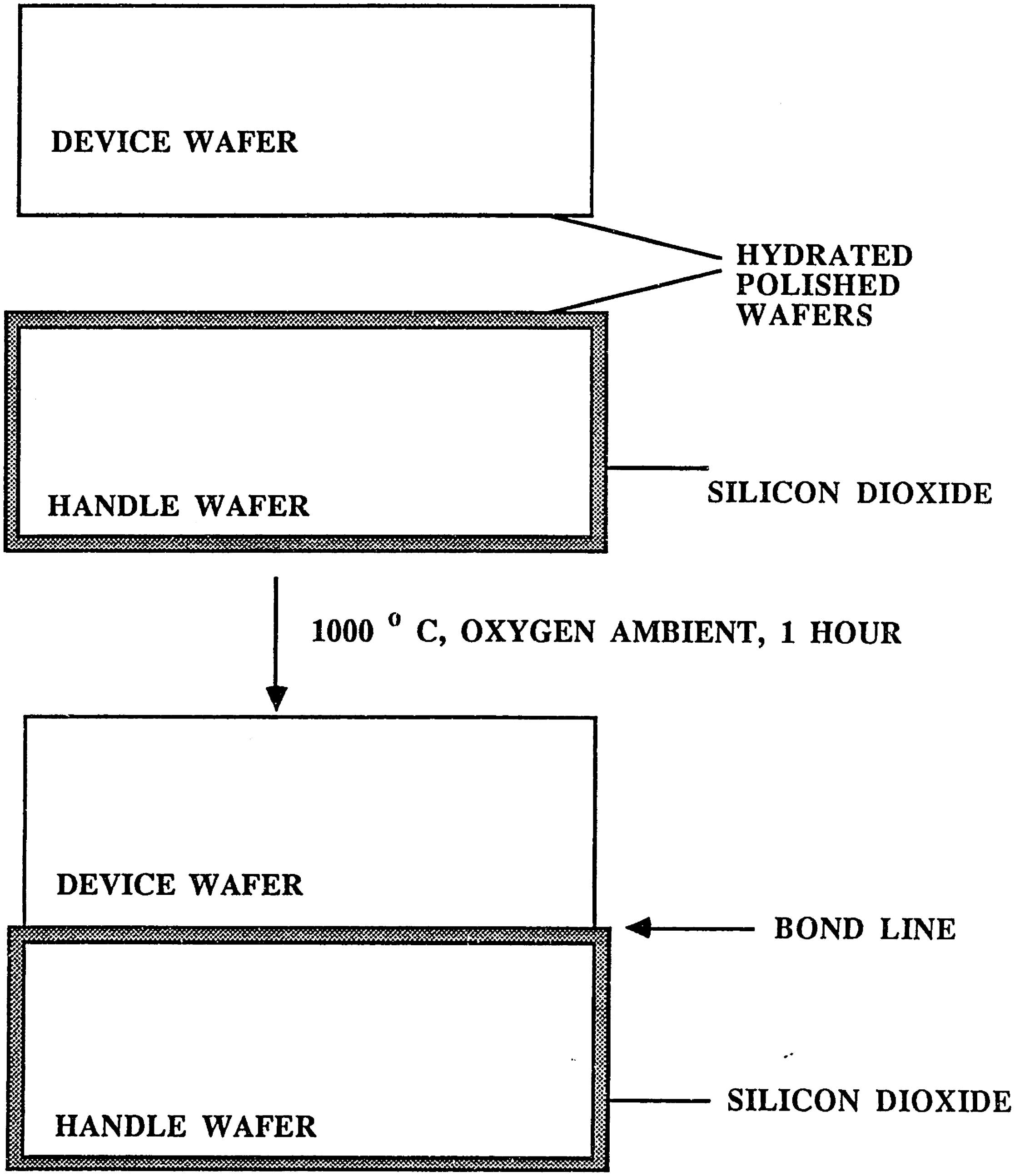

FIGURE 1-3: Cross-Section of Wafers in Bonding Process

which is a much stronger bond than the Van der Waals forces. The oxygen in the water vapor produced by the reaction is converted to SiO_2 and the hydrogen diffuses through the wafer and is dispersed. The strength of the bond between the wafers from room temperature to 1400^oC has been studied by Maszara [6] based on crack propagation theory and they reported that the surface energy of the Van der Waals bonds are between 60 and 85 erg/cm^2 at room temperature and between 600 and 700 erg/cm^2 after the 1000^oC anneal.

1.3.2 Wafer-Thinning

In order to form the thin film of silicon after bonding, one of the following procedures may be employed to thin the wafer:

a) Mechanical Polishing

b) Etching in an alkaline solution with a chemical etch-stop

c) Electrochemical Etch-Stop

Mechanical Polishing

In the mechanical polishing method, the bonded wafer is contacted to a support body of a wafer polishing machine and the device wafer is then mechanically lapped. However, this lapping will result in sub-surface damage of 10-25 mircons in depth. Usually, this sub-surface layer is removed by tribochemical (Syton) polishing which is a chemomechanical polishing technique and does not result in surface damage. The reason why tribochemical polishing is not used throughout the process is the lack of geometrical precisions as to flatness and parallelism of the surfaces of a wafer [5]. The advantages are a smooth surface layer finish and the quality of the silicon-on-insulator (SOI) layer is that of bulk silicon. The disadvantage is the cost since the wafers need to be ultra flat to provide good layer thickness control.

Etching in an Alkaline Solution

Silicon in the <100> and <110> directions can be etched in alkaline solutions of sufficiently high pH [7, 8, 9, 10, 11]. It has been proposed [12, 13] that the etching

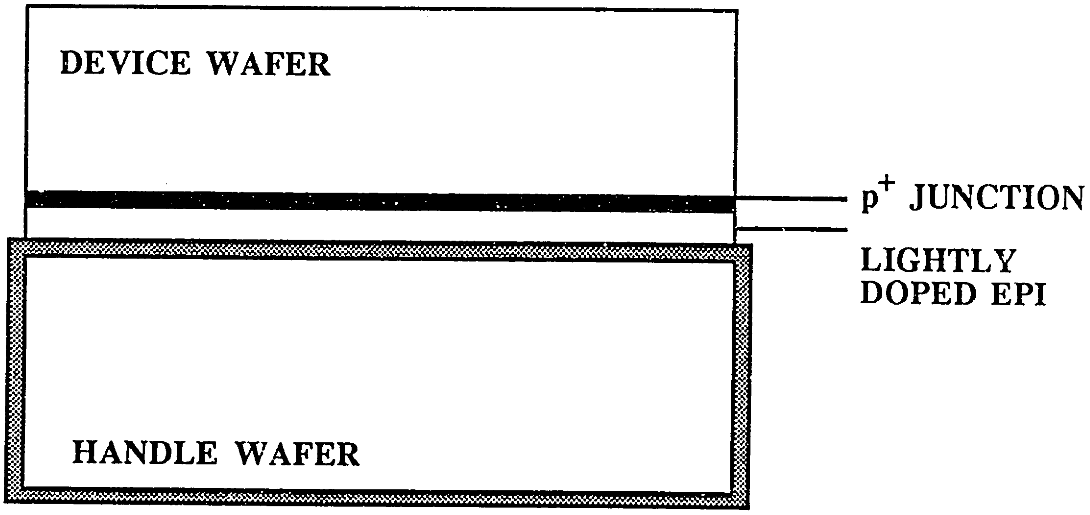

FIGURE 1-4: Lightly Doped Epi on p^+ Diffused Junction

mechanism is a hole driven process which can be summarized by

$$Si + 2OH^- + 2H_2O \rightarrow SiO_2(OH)_2^{--} + 2H_2 \qquad (1.4)$$

A typical etch rate for <100> Si in 20% KOH at 80°C is 80μm per hour. A silicon wafer can be thinned using a timed etch, however, control of the etch due to minor temperature variations and depletion of the electrolyte is a substantial disadvantage. Furthermore, the surface usually has a roughness of 2-3 μm.

These alkaline solutions are also known to exhibit much reduced etch rates for highly doped p^+ surfaces ($> 3 \times 10^{19} cm^{-3}$) At these doping levels, the semiconductor is degenerate with the Fermi level almost at the valence band [12]. The etch ratios for moderately doped and p^+ doped wafers can be of the order of a 1000. Therefore, etching can be selectively stopped at the p^+ layers giving better control and also a smoother surface. In general, however, a highly doped layer cannot be used for circuit applications. A variation of this process would be to grow a lightly doped epitaxial layer on top of the p^+ wafer [6]. This is shown in Figure 1-4. The heavily doped layer can be removed using a chemical mixture leaving just the lightly doped surface. While this method is simple and easily controlled , the disadvantages are the dislocations in the epi that is a print from the p^+ surface and the high cost of the wafers itself. However, for most sensor applications that do not require a high level of circuit integration, this method may be well suited.

Electrochemical Etch-Stop

When silicon is electrically biased positive with respect to a reference electrode (anodic) in an alkaline solution, there is a potential range where silicon can be etched and there is a potential range where it will be passivated with an anodic oxide and not etch [14, 15, 16, 17]. As a result, if a p-n junction is reversed biased at an appropriate potential, the n-type silicon will passivate and the p-type will etch. This property can be used as an etch-stop mechanism, as shown in Figure 1-5. Potential is applied to the bonded wafer and the contact is made to the n-type layer. The counter electrode is used as a return path for the current and the reference electrode provides a consistent way to measure relative potential since all potentials will be referenced to it. When the n-type surface is exposed, the applied voltage will passivate the surface, resulting in a uniform and known thickness of silicon. The advantages are good control and the possibility of batch processing while the disadvantages are the difficulty of making contact and an orange peel surface at the end of the process.

1.4 Outline of Thesis

Chapter 2 will describe the design of the sensor and the transduction mechanism. It will include both analytical and finite-element-analysis results. Chapter 3 will present the fabrication issues and the mechanical and electrical properties of the process. Data on the piezoresistance calibration will be given in chapter 4 and the calibration of the sensor will be discussed in chapter 5. Chapter 6 will be the conclusion.

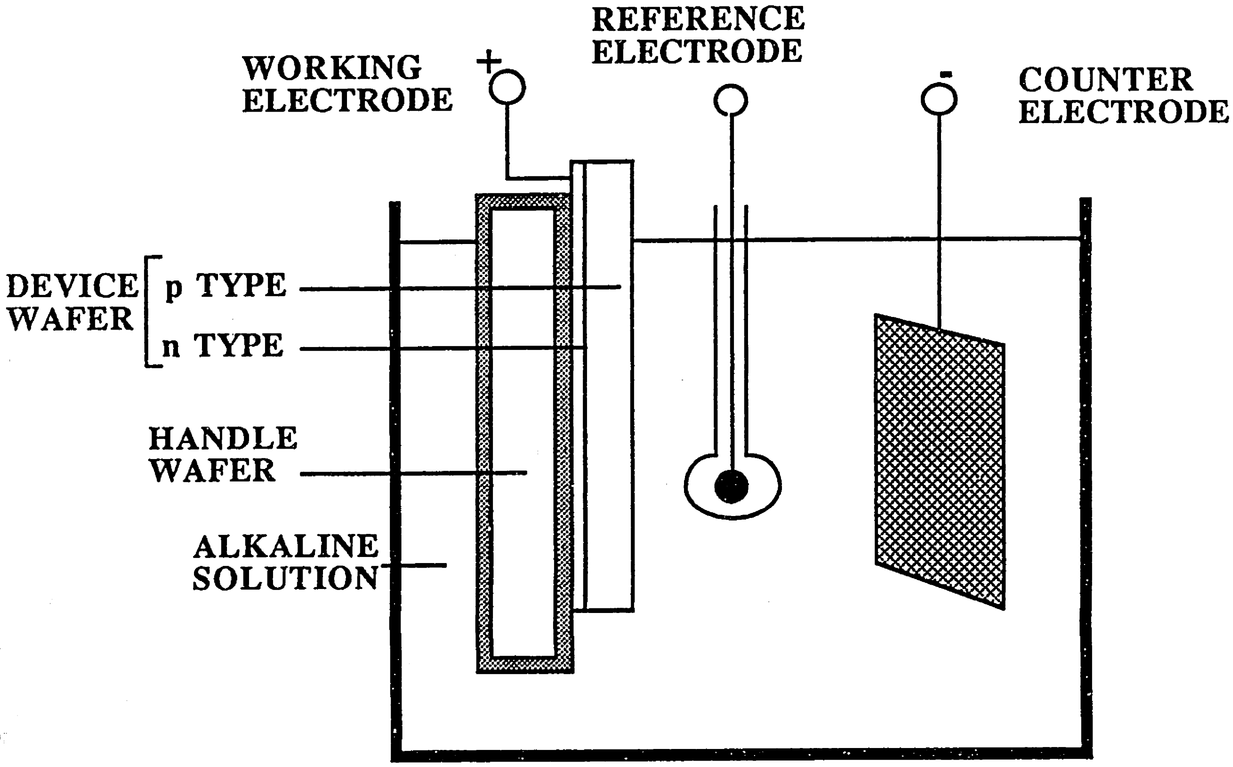

FIGURE 1-5: Electrochemical Etching Setup

2

Sensor Design

In this chapter, we will present the structure of the sensor together with the performance specifications that we have targeted. A brief description of how the sensor would work is given and this is followed by the static analysis of the structure under loading using both hand calculations and finite-element methods. The electrical response of the sensor will be analyzed and the layout of the chip together with the diagnostic structures will be presented.

2.1 Structure of Device

In order to determine the actual structure of the shear sensor, it is desirable to have a performance specification so that the design can be aimed towards a particular environment where it can be tested. 3M Corporation has provided us with these data based on actual industrial environments and one where the sensor can find an immediate application. The specifications are listed below.

Viscosity - 10^4 poise

Temperature - 150°C → 200°C

Pressure - 10 atmospheres

Shear Stress - 1kPa - 100kPa

Both the temperature and shear stress data represent the desired range of operation while the viscosity and pressure data represent a typical situation that is to be expected during operation. From the information given above, we see that the sensor needs to be robust to withstand the elevated temperatures and pressures. Furthermore. the liquid may be conductive and any measurement scheme would have to take that into consideration.

Figure 2-1 shows a 3-dimensional view of the microfabricated floating-element. The material is silicon and the square holes on the plate are meant to provide access for the etchants to remove the sacrificial oxide layer at the end of the process. The plate is 5μm thick and is supported at its four corners by tethers 30μm long and 10μm wide. When the liquid flows over the device, a drag results and the structure will be displaced. The drag from the component of the flow axial to the tethers (y-direction) will result in compressive stresses at the pair of tethers further away form the source of flow and tensile stresses at the pair of tethers nearer to the source of flow. Because of the crystalline nature of silicon, stresses result in changes in resistance, known as the piezoresistive effect. For the case of the n-type silicon, which is what we used, compressive stresses result in an increase in resistance while tensile stresses result in a decrease in resistance and for the same level of stress the magnitude of the change is identical. If each of these tethers represent a resistor the configuration is similar to that of a Wheatstone bridge. Therefore, by bringing in the electrical interconnects to the supports and to the plate, we can measure the change in resistance and hence the shear force. Figure 2-2 shows the top view of the floating-element with the metal interconnects and the circuit schematic. The metal to the square plate will be brought in via one pair of tethers and the resulting circuit is a half-Wheatstone bridge. The plate contact is called the sense electrode and one of the contacts at the support will be the drive electrode while the other represents the ground electrode. The drive electrode provides a fixed voltage while the sense electrode will detect changes in the potential as a function of shear-stress. An advantage of using this readout configuration is its first order insensitivity to lateral and vertical movements, assuming small deflections. When the floating-element is loaded laterally or vertically, the tethers undergo a change in resistance of the same magnitude and sign, thereby nulling the effect.

The purpose of using silicon as a material of choice stems from both its strength as a mechanical material (E_{Si}= 200GPa), providing enough rigidity for the specifications mentioned above, and the knowledge of silicon processing that has been accumulated from the field of microelectronics fabrication. Since the whole tether acts as a thin resistor. there is no charge leakage from the resistor to the bulk material at high

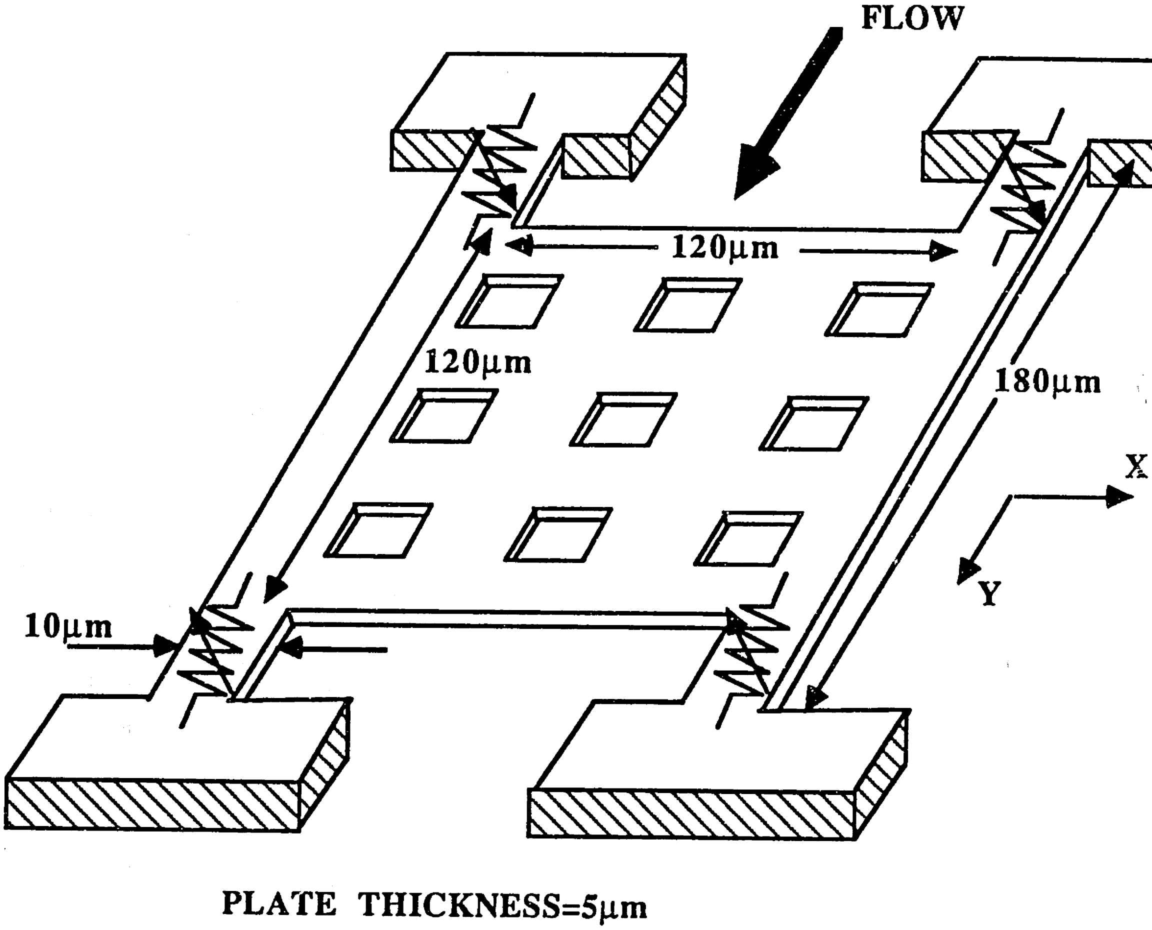

FIGURE 2-1: 3-Dimensional View of Floating-Element

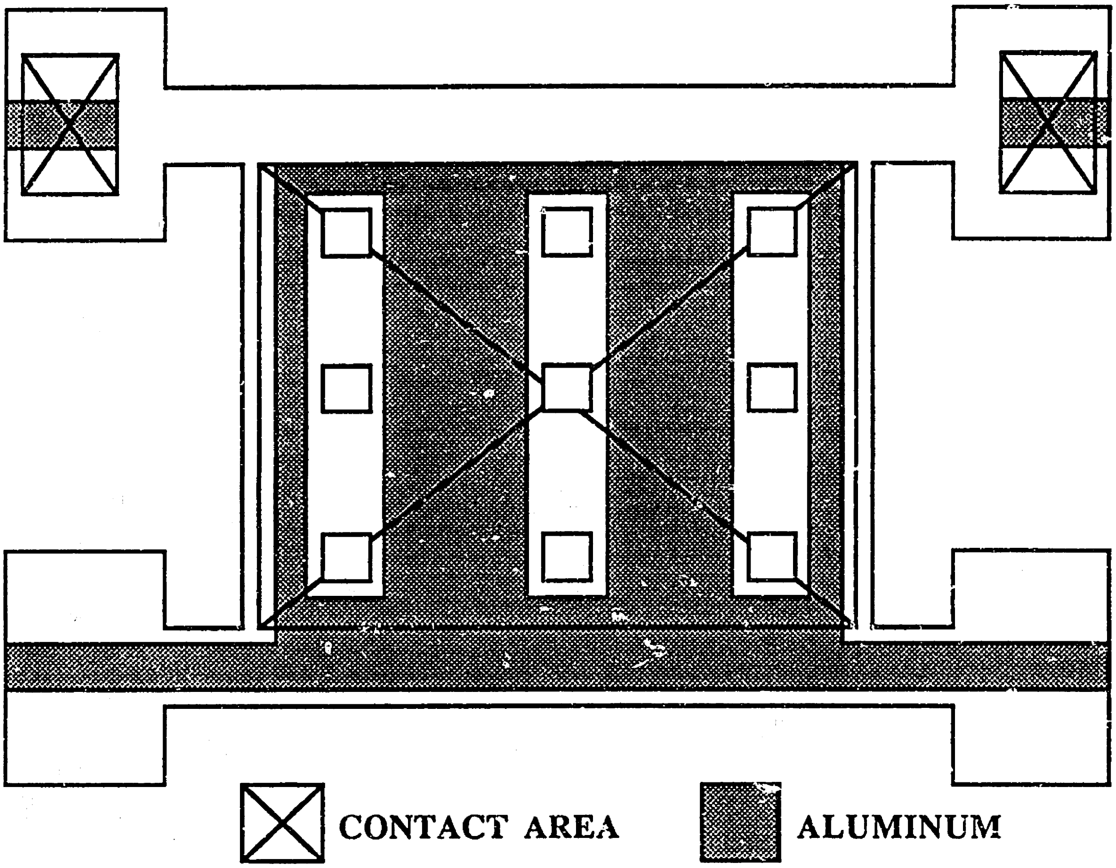

FIGURE 2-2: Floating-Element with Metal Interconnects

temperatures, as is normally the case for piezoresistors diffused into bulk silicon. Fujii [18] showed that with dielectrically isolated piezoresistors, they managed to attain linearity up to 300°C without any circuit compensation. Finally the use of piezoresistors as a transduction mechanism allows the possibility of the liquid being conductive.

2.2 Mechanical Analysis

In order to evaluate the response of the floating-element due to loading, we first derive a stress-strain relationship for the structure in terms of its dimensions and verify the results by simulation using finite- element methods.

2.2.1 Analytical Model

The derivation below assumes

I. Motion is permitted only in the plane of the plate.

II. The liquid flowing underneath the floating-element has negligible velocity.

III. The area of the square plate is large compared to the area of the tethers

IV. The plate is rigid under loading and the material is elastic.

We first consider flow axial to the tethers (y-direction). The shear force F acting on the plate of area A_p is $\tau_{xy}A_p$ which is the shear stress multiplied by the area exposed to the flow. Each tether will now experience a force acting axially and of magnitude

$$F/4 = \frac{\tau_{xy}A_p}{4} \tag{2.1}$$

where the 4 in the denominator assumes that the force is uniformly distributed over each of the four tethers. The stress on the tethers, σ_{yy}, is just equation 2.1 divided by the cross-sectional area of the tethers.

$$\sigma_{yy} = \pm\frac{\tau_{xy}A_p}{4t_t w_t} \tag{2.2}$$

The positive sign indicates tensile stress while the negative sign indicates compressive stress. Assuming that the material is elastic in the range of operation, we can use

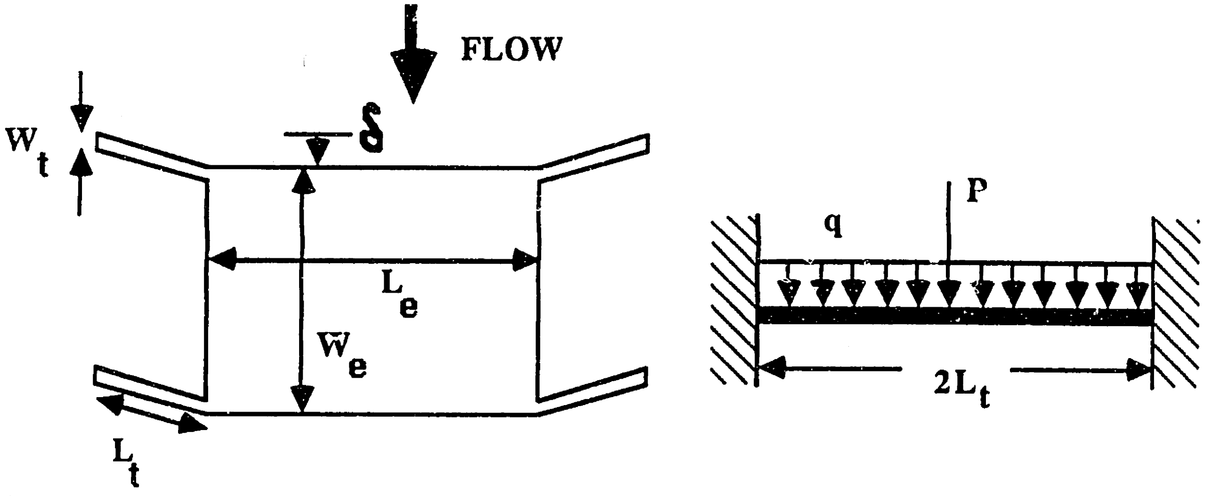

FIGURE 2-3: Model of Clamped-Clamped Bridge Under Lateral Loading

Hooke's Law to relate the stress to strain. Therefore,

$$\varepsilon_{yy} = \pm\frac{\tau_{xy}A_p}{4t_tw_tE_{Si}} \tag{2.3}$$

where E_{Si} is the Young's Modulus for silicon. Furthermore if the length and width of the plate are L_e and W_e respectively

$$\varepsilon_{yy} = \pm\frac{\tau_{xy}L_eW_e}{4t_tw_tE_{Si}} \tag{2.4}$$

Substituting the dimensions of the floating-element as shown in Figure 2-1 and using a Young's Modulus value of 200GPa [19]

$$\varepsilon_{yy} = \pm 3.6 \times 10^{-10}\tau_{xy} \tag{2.5}$$

Equation 2.5 represents the relationship between the shear stress of the liquid on the wall and the strain that results in each of the tether. For the range of shear stress that we are interested in (1kPa - 100kPa), the amount of strain corresponds to 3.6×10^{-7} to 3.6×10^{-5} which is much less than the fracture strength of silicon of around 10^{-2} [19].

For the case of flow perpendicular to the tethers we can use the model of a clamped-clamped bridge of length $2L_t$ [1] shown in Figure 2-3 where $P = \frac{1}{2}\tau_{yx}A_p$ is the concentrated force applied at the center of the bridge. From [20]

$$\delta = \frac{1}{32E_{Si}t_t}\left(\frac{L_t}{W_t}\right)^3 A_p\tau_{yx} \tag{2.6}$$

Using the maximum shear stress of 100kPa, this results in a deflection δ of $1.2 \times 10^{-3}\mu$m. If we compare this value to the displacement of the tether under axial load for the same τ_{xy}, ($\varepsilon_{yy}l_t = 3.6 \times 10^{-4}\mu$m), the perpendicular load has an order of magnitude higher deflection because the floating-element is less rigid in the perpendicular direction. However, the amount of strain is still less that the critical strain and as mentioned in section 2.1 the readout is insensitive to deflections in the perpendicular direction.

2.2.2 Finite-Element Method

Apart from the analytical solution, we have also performed simulation using finite-element methods to confirm the mechanical response. The floating element is divided into solid cubic elements as shown in Figure 2-4 which has altogether 322 elements. There are two different sizes of elements; the region near the tethers have smaller areas (5μm × 10μm) since the stresses are concentrated there while the plate has larger element sizes (10μm × 10μm). Each element consists of 8 nodes corresponding to the corners of the cube. The boundary conditions for the ends of the tethers were simulated as fixed supports while the rest of the structure was allowed to move freely having all six degrees-of-freedom. The flow is from the positive x-direction as shown in Figure 2-4. Because the simulation package did not have a shear load on the face of an element, the loading was done by applying concentrated forces on the nodes. As shown in Figure 2-5, each cubic element had four concentrated forces on the face exposed to the flow. Each element will experience a shear force $F = \tau_{yx}A_e$ where A_e is the area of each element. Each of the four corner nodes will have a force of F/4. Since adjacent elements share common nodes, it is important that the forces are added correctly and in general can be nF/4 where n=2,3 or 4. We have assumed an elastic material with a Young's Modulus of 200GPa. The simulation was performed using ABAQUS as the finite-element package with PATRAN being the graphics interface and a SUN 4 as the computing platform. Each simulation took about five minutes of CPU time. Figure 2-6 shows the deformed structure superimposed on the original structure. It should be noted that the deformations are exaggerated so that distinctions could be

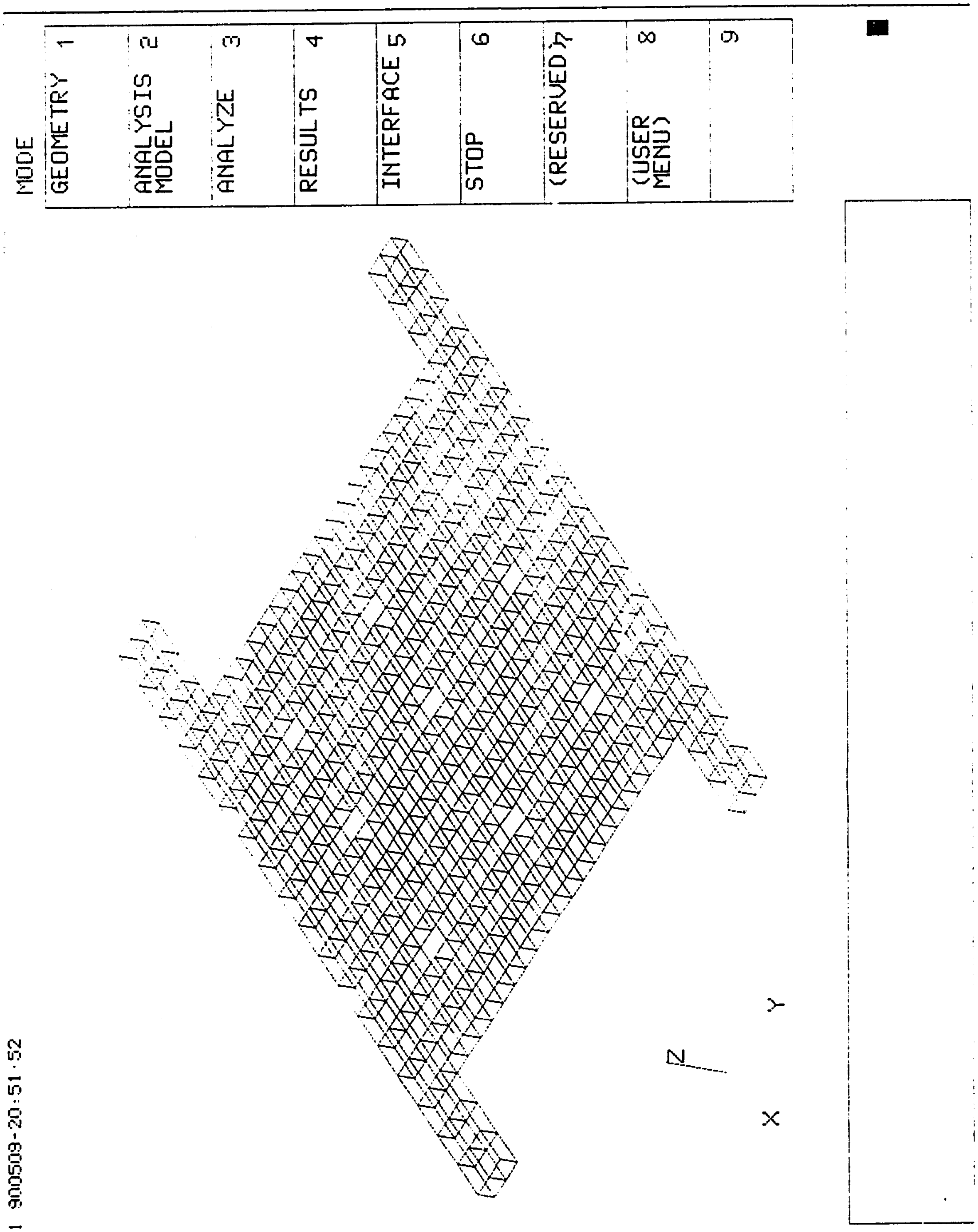

FIGURE 2-4: Finite-Element Mesh

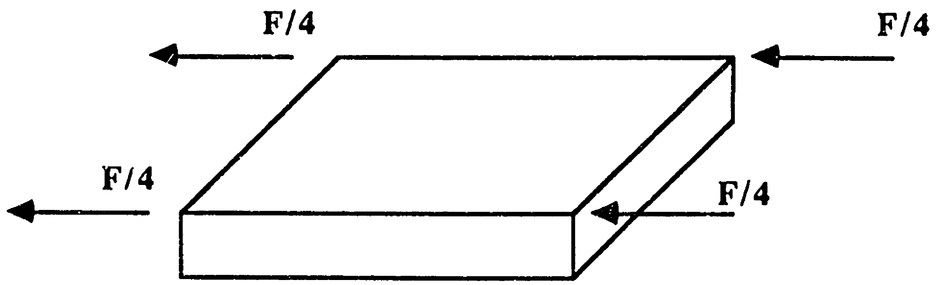

FIGURE 2-5: Loading of Elements

made between the two shapes. The deformed shape is symmetric about the x-axis and it can be observed that the part of the plate on the upper right of the figure is bent up while the part on the bottom left is bent downwards. This represents the reaction of the floating-element to the bending moment that results because the shear force is only present on the top surface where the liquid is flowing. The protrusion however is small and is of the order of $10^{-3}\mu$m which is only about 0.02% of the plate thickness. From Trilling and Hakkinen [21] the pressure acting on the protruding face is $p = 1.2\tau_{yx}$ and is valid if $\frac{\tau_{yx}\rho l^2}{\mu^2} \ll 1$. For a τ_{yx} of 100kPa, a protrusion of $10^{-3}\mu$m, μ of 10^4 poise, the value is $1 \times 10^{-16}\rho$ where ρ is in kg/m^3. For liquids, the density is less than 10^4 kg/m^3 and the expression is very much less than 1. Therefore, the fractional contribution of the pressure force to the total shear force on the element is $1.2\frac{l}{L_e}$ or less than 0.02%. Hence, the protrusion effect is negligible. Figure 2-7 gives a contour plot of the x-displacement of the floating-element due to loading. The maximum displacement is at the center of the edge of the plate since there is no support there. The strain at the tethers are symmetrical and the boundaries at the end are fixed. If we magnify the plot and zoom in on the lower right tether to observe the reaction forces we can determine the magnitude and direction of the forces at each node, as shown in Figure 2-8. Here, the magnitude of the force is proportional to the length of the arrow. The reaction forces are concentrated at the tethers since they act as supports for the floating-element and the direction of some of the arrows are slightly off axis resulting from the bending moment of the plate about the axis of the tether. The angle, however, is small enough to justify the earlier assumption in the analytical model that the stress is uniformly distributed over the cross-section of the tether.

Finally, we can obtain the strain data of the nodes for different shear stresses and Figure 2-9 shows the stress-strain relationship for two of the nodes at the tethers with node 4 representing minimum strain and node 2 representing maximum strain. The slope of the lines are 5×10^{-10} and 4×10^{-10} for node 2 and 4 respectively. This value is close to the 3.6×10^{-10} value that we obtained analytically.

2.3 Electrical Analysis

To detect the mechanical response of the floating-element, various transduction mechanisms can be implemented such as capacitive or piezoresistive sensing. Because of the small area and the possibility of conducting fluids, the capacitive method is less appealing. Piezoresistive sensing can be used for large enough signals and is easier to implement since it is less susceptible to problems with parasitics. Furthermore, with the present design of the floating-element, the tethers are inherently piezoresistive, keeping the fabrication process simple and minimizing the number of masks involved.

2.3.1 Piezoresistive Property of Silicon

When single crystal silicon is stressed, the resistivity is changed. This property is utilized in a variety of applications as a transduction mechanism [22, 23, 24, 25]. For a semiconductor, the electric field can be expressed as a function of stress and current density [26, 23]

$$\mathcal{E}_i = \mathcal{E}_i(j_j, T_{kl}) \quad i, j, k, l = 1, 2, 3 \tag{2.7}$$

where $\mathcal{E}_i$ is the electric field in the i direction, j_j represents the current density along the j axis and T_{kl} represents the stress in the direction kl. By taking a Taylor's expansion series around zero current density and zero stress and retaining the non-zero terms [27]

$$\mathcal{E}_i = \sum_{j=1}^{3}\sum_{k=1}^{3}\sum_{l=1}^{3}(\rho_{ij} j_j + \pi_{ijkl} j_j T_{kl}) \quad i = 1, 2, 3 \tag{2.8}$$

with

$$\rho_{ij} = \frac{\partial \mathcal{E}_i}{\partial j_j} \tag{2.9}$$

and

$$\pi_{ijkl} = \frac{\partial^2 \mathcal{E}_i}{\partial j_j \partial T_{kl}} \tag{2.10}$$

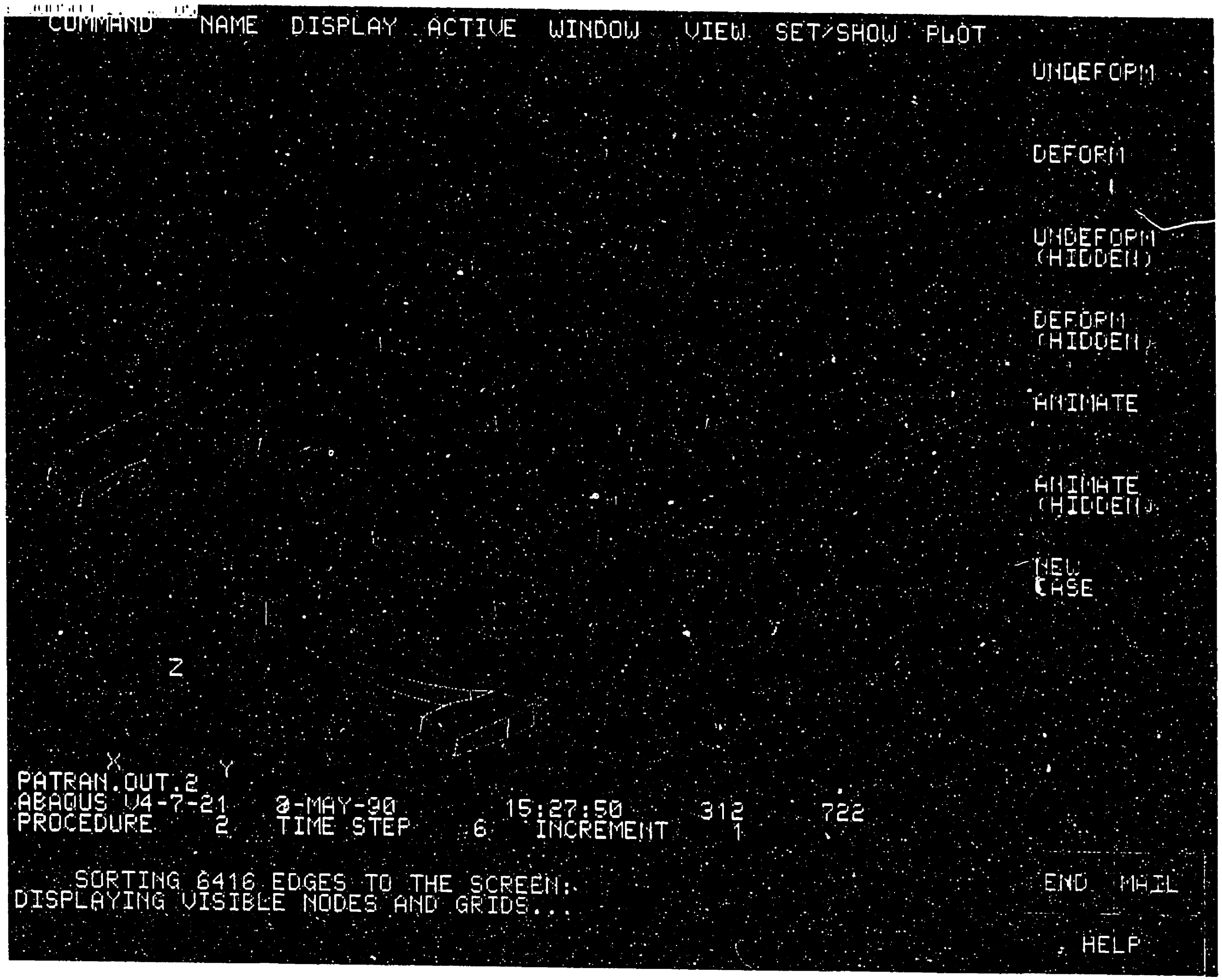

```
PATRAN.OUT.2
ABAQUS V4-7-21    0-MAY-90      15:27:50    312     722
PROCEDURE     2   TIME STEP   6   INCREMENT    1

   SORTING 6416 EDGES TO THE SCREEN:
DISPLAYING VISIBLE NODES AND GRIDS...
```

Figure 2-6: Deformation of Structure

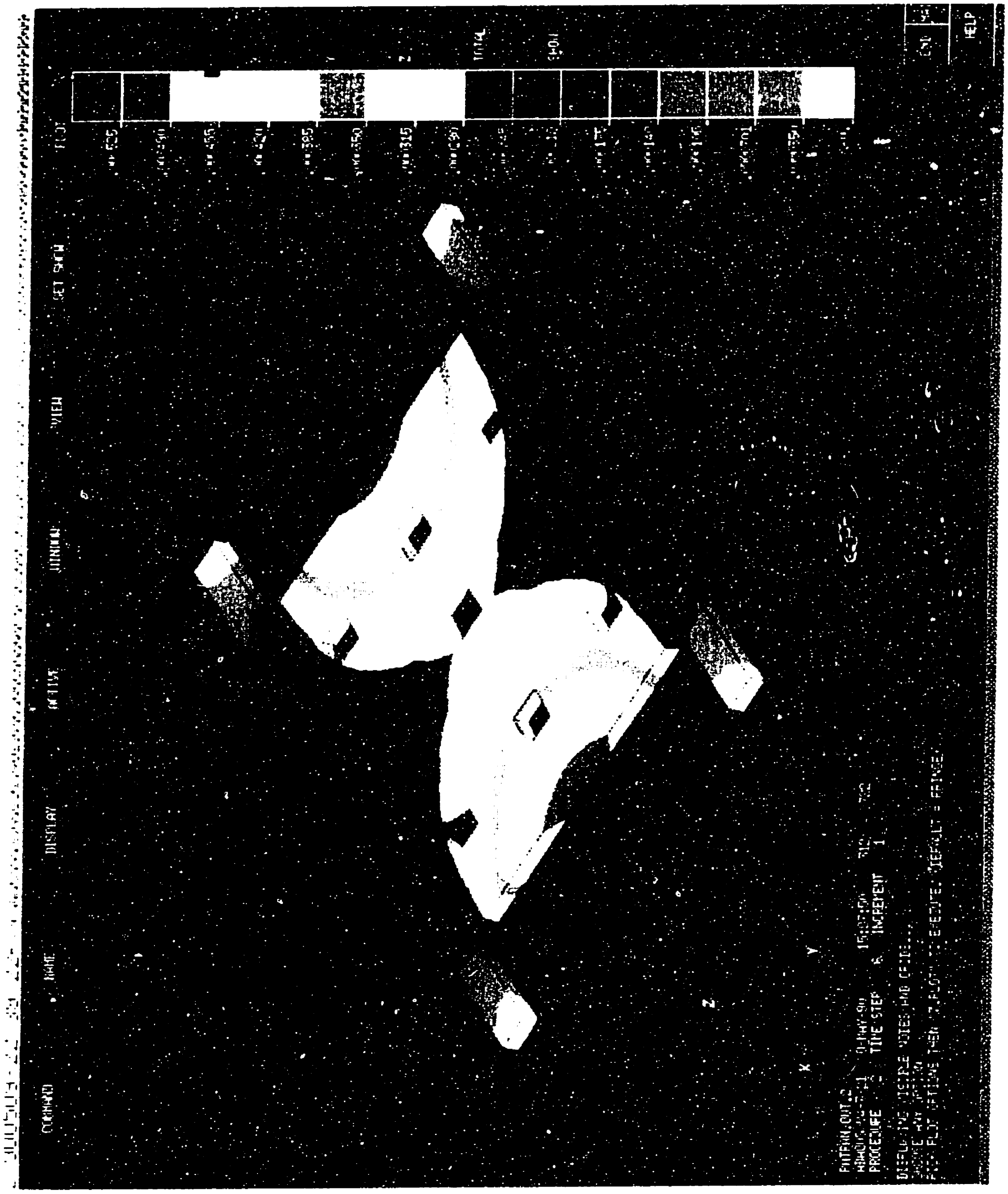

Figure 2-7: Contour Plot of x-Displacement

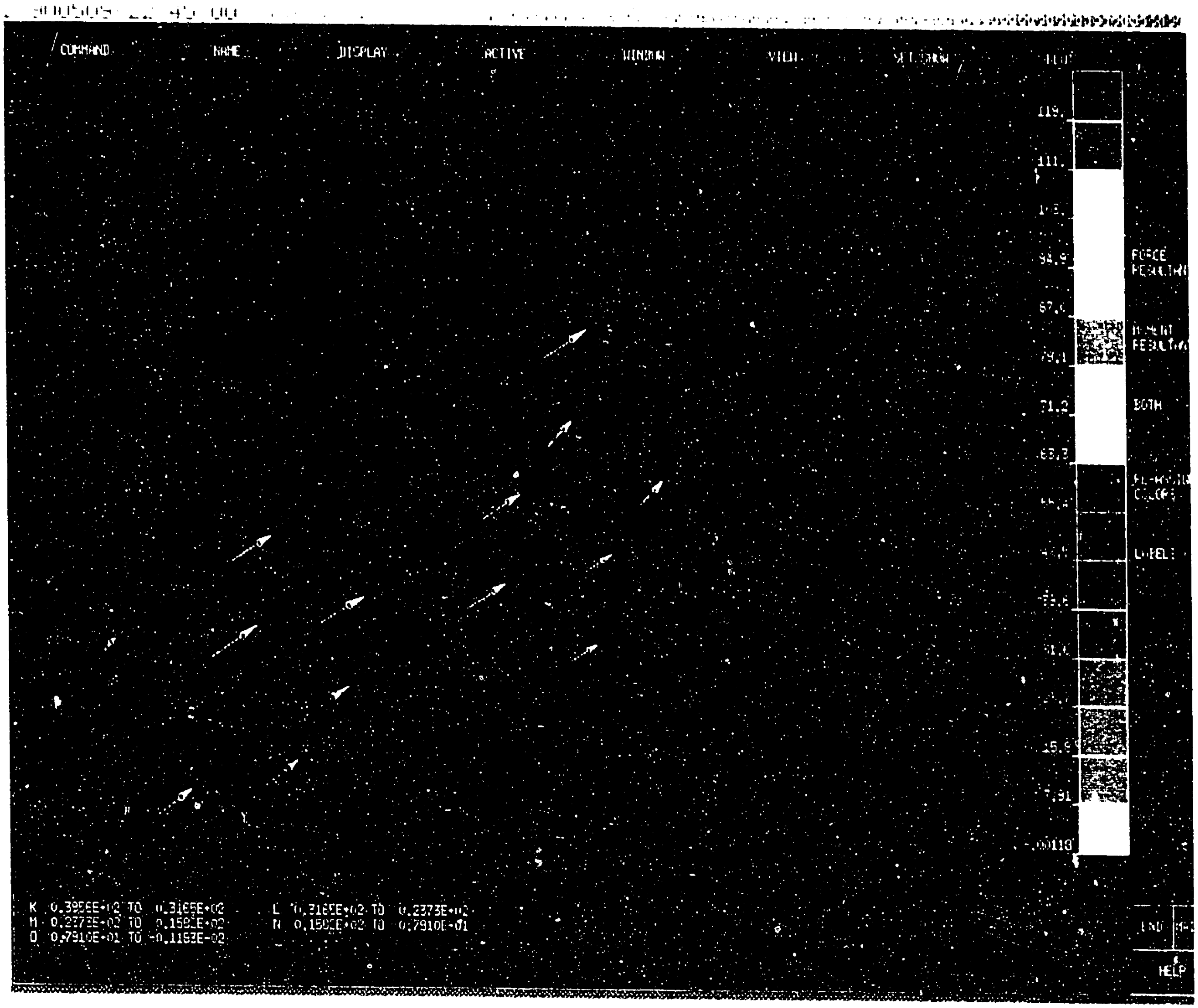

```
K  0.3955E+02 TO  0.3165E+02      L  0.3165E+02 TO  0.2373E+02
M  0.2373E+02 TO  0.1582E+02      N  0.1582E+02 TO  0.7910E+01
O  0.7910E+01 TO -0.1163E-02
```

FIGURE 2-8: Reaction Forces at Tether

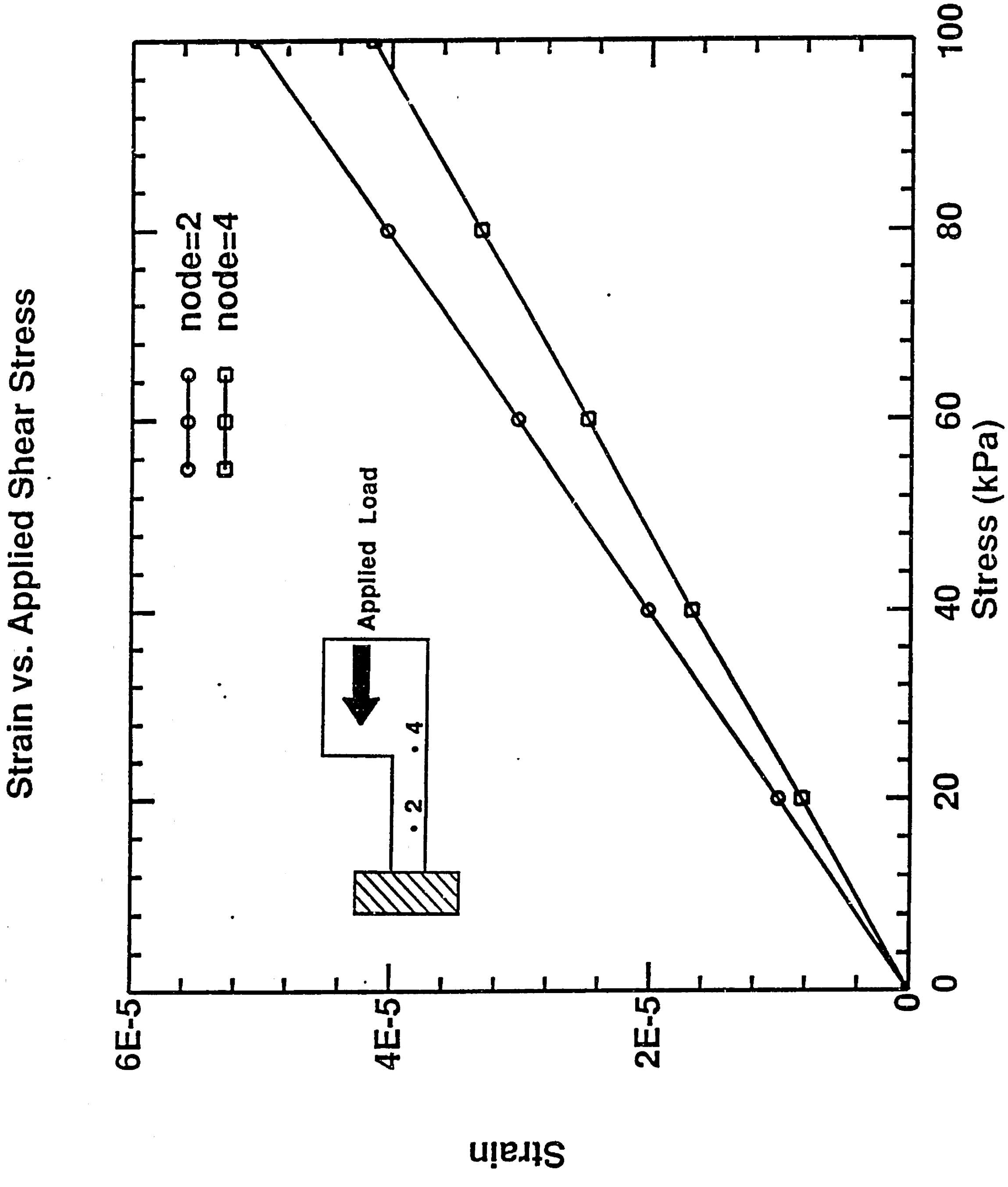

FIGURE 2-9: Plot of Strain vs Stress

Because of the crystal symmetry in silicon, only three parameters are of interest: π_{1111}, π_{1122} and π_{2323}. Furthermore, the resistivity is isotropic and $\rho_{ii} = \rho$ (i=1,2,3). The notations in piezoresistive calculations can now be simplified to:

$$\rho\pi_{11} = \pi_{1111} \tag{2.11}$$

$$\rho\pi_{12} = \pi_{1122} \tag{2.12}$$

$$\rho\pi_{44}/2 = \pi_{2323} \tag{2.13}$$

Therefore, given π_{11}, π_{12} and π_{44}, the change in resistance as a function of stress can be calculated. For the case of a silicon resistor that is uniaxially strained, the change in resistance as a function of strain along the direction of applied stress is

$$\left(\frac{\Delta R}{R}\right)_l = G_l \varepsilon_l \tag{2.14}$$

where

$$G_l = \pi_{11}E + 1 + 2\nu \tag{2.15}$$

E is the Young's Modulus and ν is the Poisson's ratio. The presence of these additional terms take into account the geometric effects of the resistor as it undergoes stress. The measurements of these gage factors G are presented in chapter 4.

2.3.2 Sensor Response

By using two of the tethers in the floating element as the piezoresistors, the sensor can be configured as a half-Wheatstone bridge, shown in Figure 2-10. One of the applied potential to the tether is biased at V_D, the driving voltage, and the other tether is grounded. The potential V_o is tapped by having metal interconnects routed to the plate. When the tethers are stressed, the resistances change according to equation 2.14 with the same magnitude but opposite signs. In the derivation below, we assume R_1 increases and R_2 decreases. Therefore

$$\left(\frac{\Delta R_1}{R_1}\right)_l = G_l \varepsilon_l \tag{2.16}$$

$$\left(\frac{\Delta R_2}{R_2}\right)_l = -G_l \varepsilon_l \tag{2.17}$$

The potential V_o is then given by

$$V_o = \frac{R_2[1 - G_l\varepsilon_l]}{R_2[1 - G_l\varepsilon_l] + R_1[1 + G_l\varepsilon_l]} V_D \tag{2.18}$$

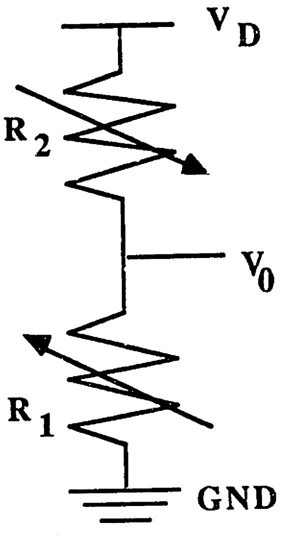

FIGURE 2-10: Half-Wheatstone Bridge Configuration

Ideally, $R_1 = R_2$ and equation 2.18 simplifies to

$$V_o = \frac{[1 - G_l \varepsilon_l]}{2} V_D \tag{2.19}$$

We can define the sensitivity as

$$S = \frac{1}{V_D} \frac{\partial V_o}{\partial \tau} \tag{2.20}$$

Substituting in the stress-strain relationship given by equation 2.5 into equation 2.19 and taking the partial derivative, we have

$$S = G_l (1.8 \times 10^{-7}) \ /kPa \tag{2.21}$$

If the gage factor for n-type silicon that is moderately doped is around 100 [28], the sensitivity of the device is $1.8 \times 10^{-5} \ /kPa$

If we assume that the operation of the device will be above the 1/f noise region and that the Johnson-noise will dominate. The Johnson noise associated with a resistor is given by [29]

$$< v_n^2 >= 4kTBR \tag{2.22}$$

where $< v_n^2 >$ is the mean square voltage, k is the Boltzmann's constant, T is the absolute temperature, B is the bandwidth in Hertz and R is the resistance value. If the measurements are done at 1kHz and using the resistance value of 100kΩ for the device and the operation temperature of 473K, $< v_n >= 1.6 \times 10^{-6} V$. Therefore, the noise voltage of the resistor is $1.6 \times 10^{-6}V$. For a 1V bias the signal to noise ratio for a 1 kPa signal is approximately 20dB and the minimum detectable signal is 0.1 kPa.

Temperature Effects

In a Wheatstone bridge configuration, the signal is a ratio of two resistors and if the nominal resistances are identical, the signal will be independent of the resistor value. This is shown in equation 2.19 , where the resistance does not enter into the output voltage.

On the other hand, the temperature coefficient of gage factor (TCG) of the piezoresistors affects the output voltage and ideally, we would like the TCG to be as small as possible. From [28, 30, 31] we would want increased doping in the silicon but this will reduce the gage factor itself.

Doping

A large value for the gage factor G_l is preferred. In general, for the same level of doping, and along the $< 100 >$ direction, n-type silicon has higher gage factors than p-type silicon. Furthermore, a lower level of doping increases the gage factor but as mentioned in the previous section, the gage factor will be more sensitive to temperature variations for lower dopings.

Misalignment

Differences in the nominal resistances of the tether would result in non-linearity in the transfer function. The dimensions of each pair of tethers are identical since they are defined at the same mask level. Also, the thickness variations of the film can be assumed to be negligible for a small area (120μm × 120μm). The critical alignment is the placement of the contacts to the resistors and this is done in the ion implantation and metal definition step. Any offset would result in differences of resistor value. If we let $R_1 = \beta R_2$, where β is a constant, equation 2.18 can be rewritten as

$$\frac{1 - G_l\varepsilon_l}{(1+\beta) + (\beta - 1)G_l\varepsilon_l} \tag{2.23}$$

If $\beta \rightarrow 1$ the result will be the same as equation 2.19; otherwise the $G_l\varepsilon_l$ factor in the denominator will affect the linearity of the response.

2.4 Sensor Layout

Based on the design discussed above, a set of masks were generated, with the layout done using the software 'kic'. Figure 2-11 shows the layout of the sensor chip with dimensions of 5.5mm × 4mm allowing a total of about 400 chips for 4" wafer. The floating-element is located at the top with a metal interconnect feeding into each tether. There are six bonding pads, numbered 1-6 starting from the left. Pad 1 is the drive electrode, pad 3 the ground electrode and pad 4,5 and 6 being the sense electrode. All these three pads have the same potential and the reason for having two additional ones are to maintain as much symmetry as possible in the chip. Pad 1 is connected to pad 2 via a five square resistor which can be used as a temperature sensor.

The three large boxes at the center are the alignment features for the photolithography and on both sides of the chip are diagnostic tools to help evaluate the process. The mechanical diagnostic tools are the cantilevers on the right and bridges on the left. The cantilevers are $20\mu m$ wide and vary from $25\mu m$ to $100\mu m$ while the bridges are $20\mu m$ wide and range from $100\mu m$ to $500\mu m$. These structures help to determine the residual stress of the silicon film and to observe if there is any buckling in the event that the film is compressive.

The electrical diagnostic tools consist of Van de Pauw structures to measure the film resistivity, contact resistance structures to measure the metal to silicon interconnect resistance and sample tethers to measure the tether resistances. Two of these tethers have metal on it to determine the effect of metal stress on the silicon film.

Apart from the features mentioned above there are diagonal boxes and rectangles of various widths to help adjust for the proper exposure time for each mask layer. Finally, there are four square boxes on each side and these help to determine when the sacrificial oxide layer has been completely etched since the boxes will 'lift-off' once the oxide has been removed from underneath them.

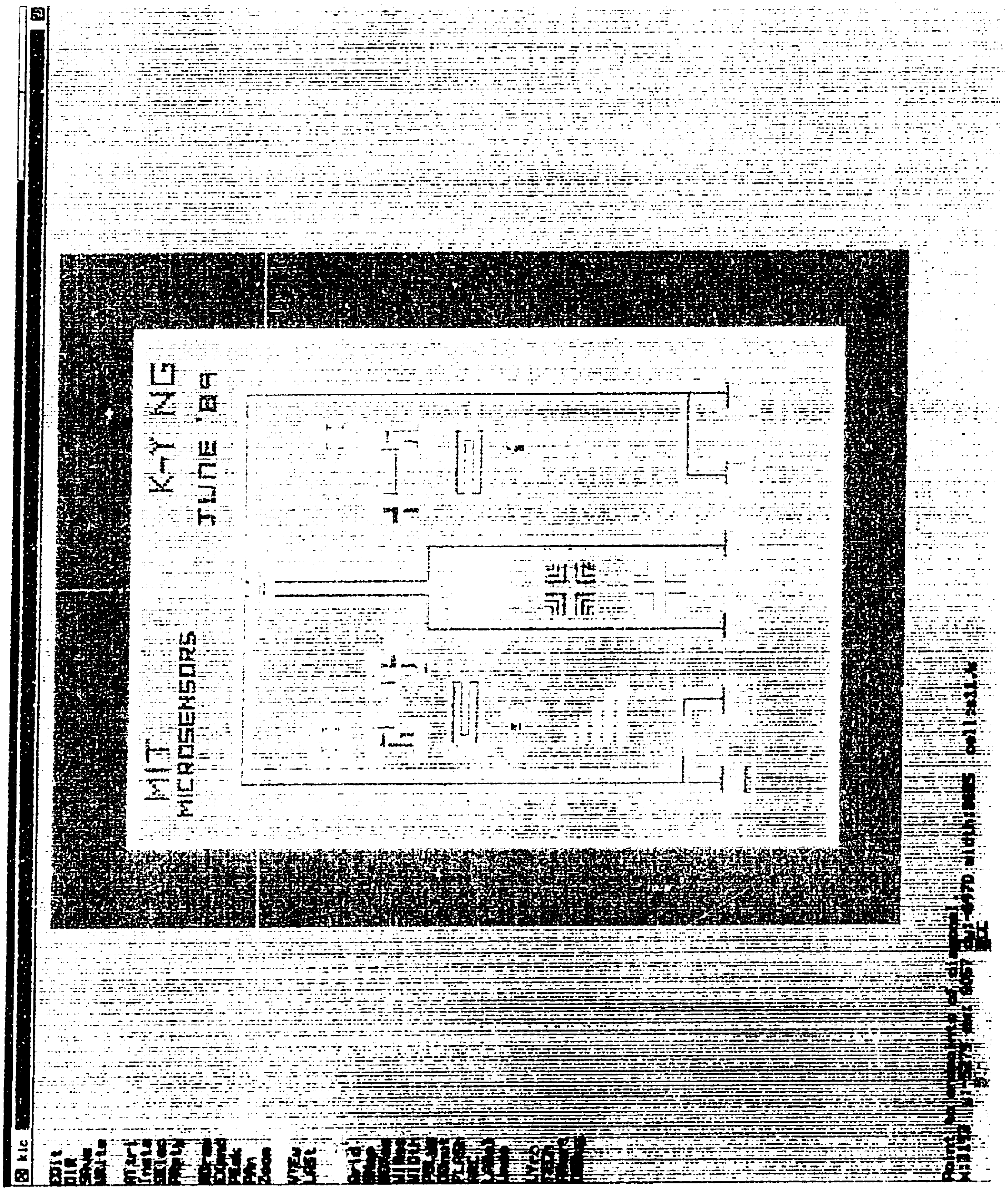

Figure 2-11: Sensor Layout

3

Fabrication and Process Characterization

A detailed description of the fabrication process for the shear- sensor is presented in this chapter. Section 3.1 gives an overview of the process emphasizing the important steps and section 3.2 to 3.8 summarizes the process development issues. In section 3.9, the electrical properties of the process is presented.

3.1 Floating-Element Process

The fabrication sequence for the sensor required four mask levels and the detailed process sequence is given in Appendix A. The description given in this section applies to the whole chip but the diagrams and figures concentrate on the floating-element. Figure 3-1 shows the cross-section of a 4 inch, 10-20Ω-cm n-type $< 100 >$ wafer that is oxidized at 950°C in steam to grow a 1.4μm thick silicon dioxide layer. This is the handle wafer as discussed in section 1.3.1. A photolithography step is then performed to pattern the oxide layer on the polished side of the wafer. The oxide that is exposed is then etched, followed by a timed silicon plasma etch to remove about 3000$\AA$ of exposed silicon. The pattern of the mask and the cross-section of the wafer are shown in Figure 3-2. There are two versions of the mask as observed in the figure. In version A, all the oxide that will be underneath the floating-element is removed while in version B, about 90% of the oxide underneath the element is removed, leaving the stumps. By selectively removing the oxide under the floating-

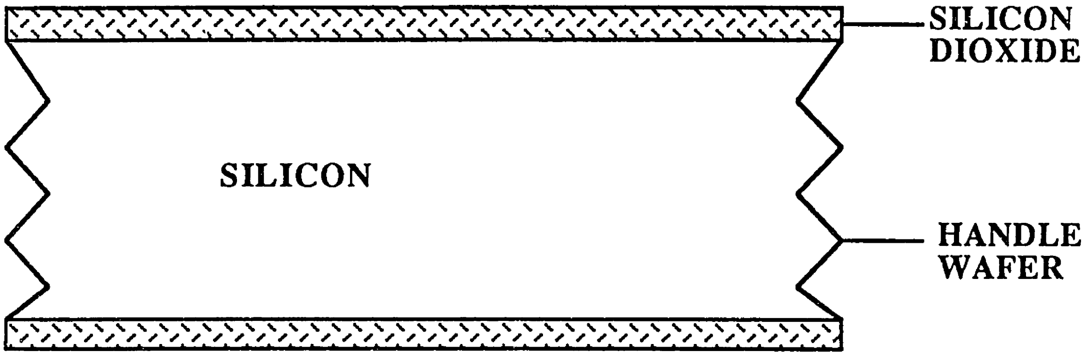

FIGURE 3-1: Oxidized Handle Wafer

element the oxide etching time required to release the floating-element in the final step is reduced significantly. The plasma etch forms steps in the wafer and roughen the surface under the element so as to prevent sticking between the floating-element and the handle wafer during the release process.

The handle wafer is then bonded to a device wafer and this wafer is chemically thinned to a thickness of approximately 5μm, shown in Figure 3-3. Section 3.2 and 3.3 gives the method that is used to bond and etch-back the wafer. The etching process does not affect the handle wafer except to thin the exposed silicon dioxide which is etched at a much slower rate compared to silicon. The wafer is then cleaned and undergoes a second photolithography step which is to ion-implant the wafer to form ohmic contacts. An infrared aligner is used to register the implantation mask to the patterned oxide. The implanted area is shown in Figure 3-4(a) in relation to the patterned oxide and Figure 3-4(b) shows the cross-section of the wafer at the end of the step. The mask used for the implant is the photoresist itself and the implant is electrically activated by a high temperature anneal as described in section 3.4.

The implant and anneal is followed by the deposition of metal to form the interconnects. The metal used for this process is aluminum ($5000\mathring{A}$) with both sputtering and electron-beam deposition successfully attempted. The aluminum film is patterned and etched in the third photolithography step and both the top view and cross section are shown in Figure 3-5. The aluminum is then sintered to form the Al-Si alloy for

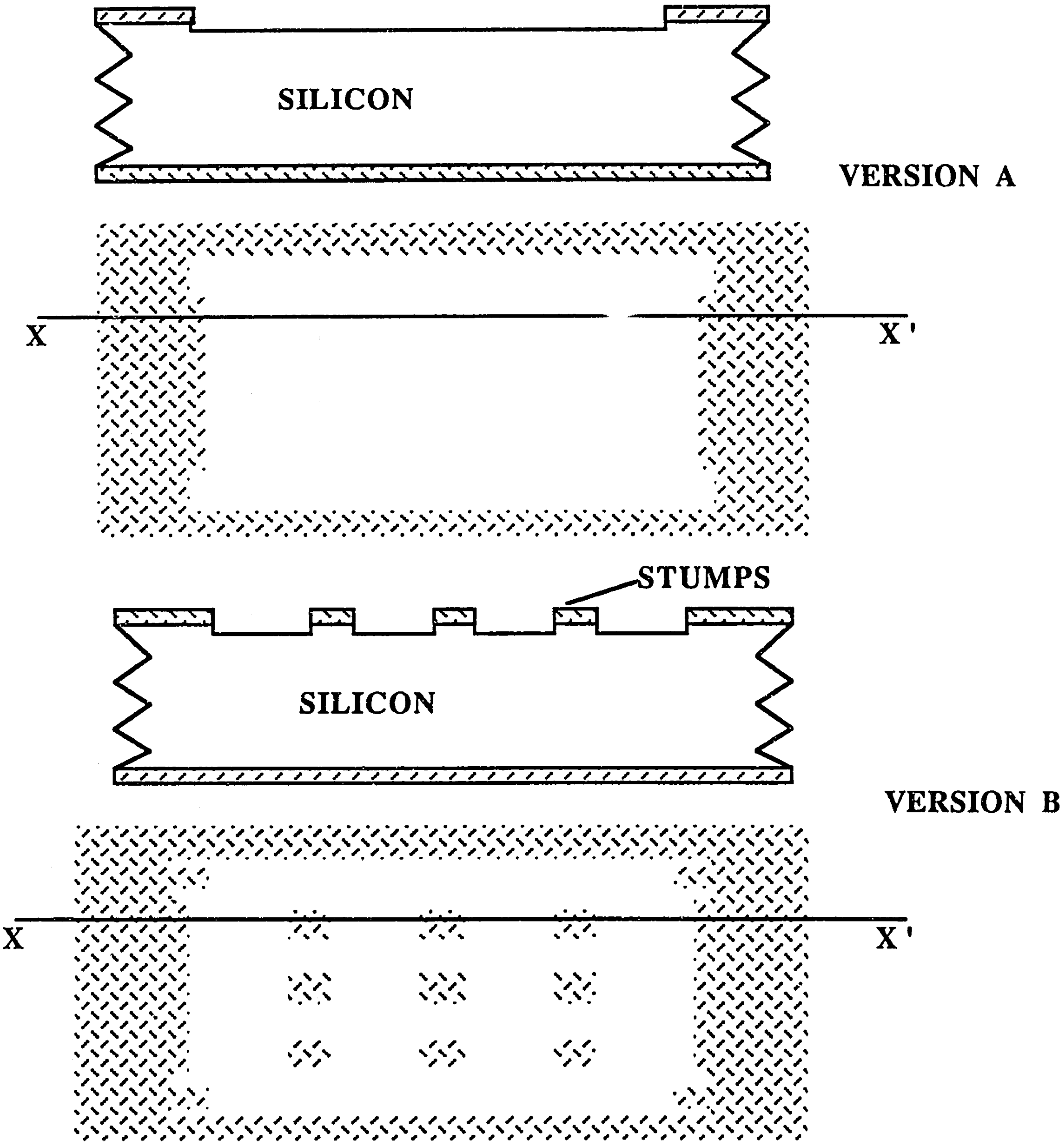

FIGURE 3-2: Pattern and Etch Oxide (Versions A and B).

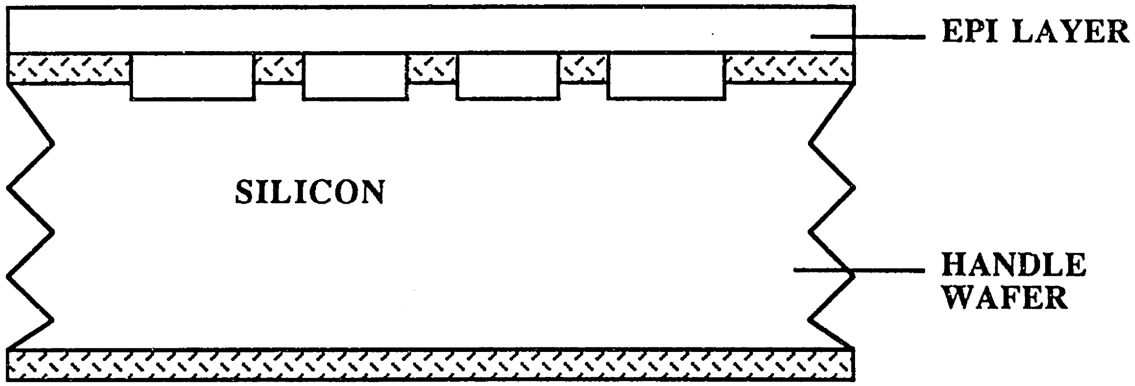

FIGURE 3-3: Wafer-Thinning

the contacts. After this, a layer of amorphous silicon is deposited over the wafer. The purpose of this is to passivate the surface and to protect the aluminum from etching in the release step of the floating-element when the wafer is immersed in hydrofluoric acid. The amorphous silicon is deposited using a plasma-enhanced-chemical-vapor-deposition (PECVD) system. A $1\mu m$ PECVD oxide is then deposited over the amorphous silicon layer to act as a masking material.

The wafer is then patterned in the next photolithography step to define the floating-element structure. The pattern is shown in Figure 3-6 and Figure 3-7(a) shows the pattern with respect to the other mask steps. The PECVD oxide is then plasma etched using resist as the mask and this is followed by the plasma etching of the silicon with the oxide as the mask(Figure 3-7(b)).

At this point, processing at the wafer level is completed and the wafer is diced into the individual chips. The releasing of the floating-element is done in hydrofluoric acid for the version B mask while the floating-elements using version A mask does not require this procedure since all the oxide has already been removed. Figure 3-8 is a scanning-electron-microscope (SEM) photograph of the floating-element that has been released. The surface is passivated with a layer of amorphous silicon and the shallow steps shown in the picture are the passivated aluminum lines. Figure 3-9 is an SEM showing the floating- element, located at the bottom center of the photo, in relation to the rest of the chip.

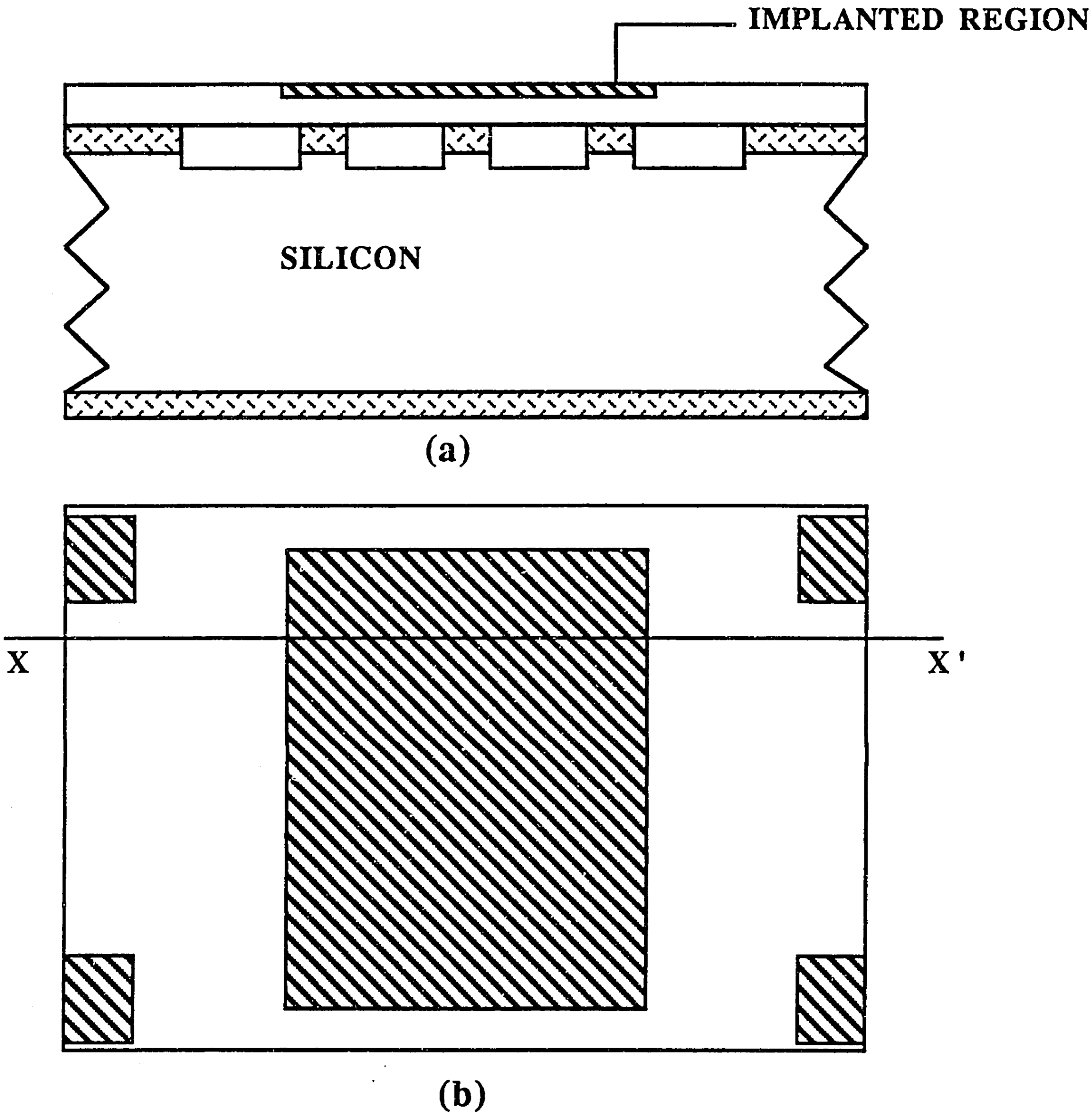

FIGURE 3-4: Ion-Implantation

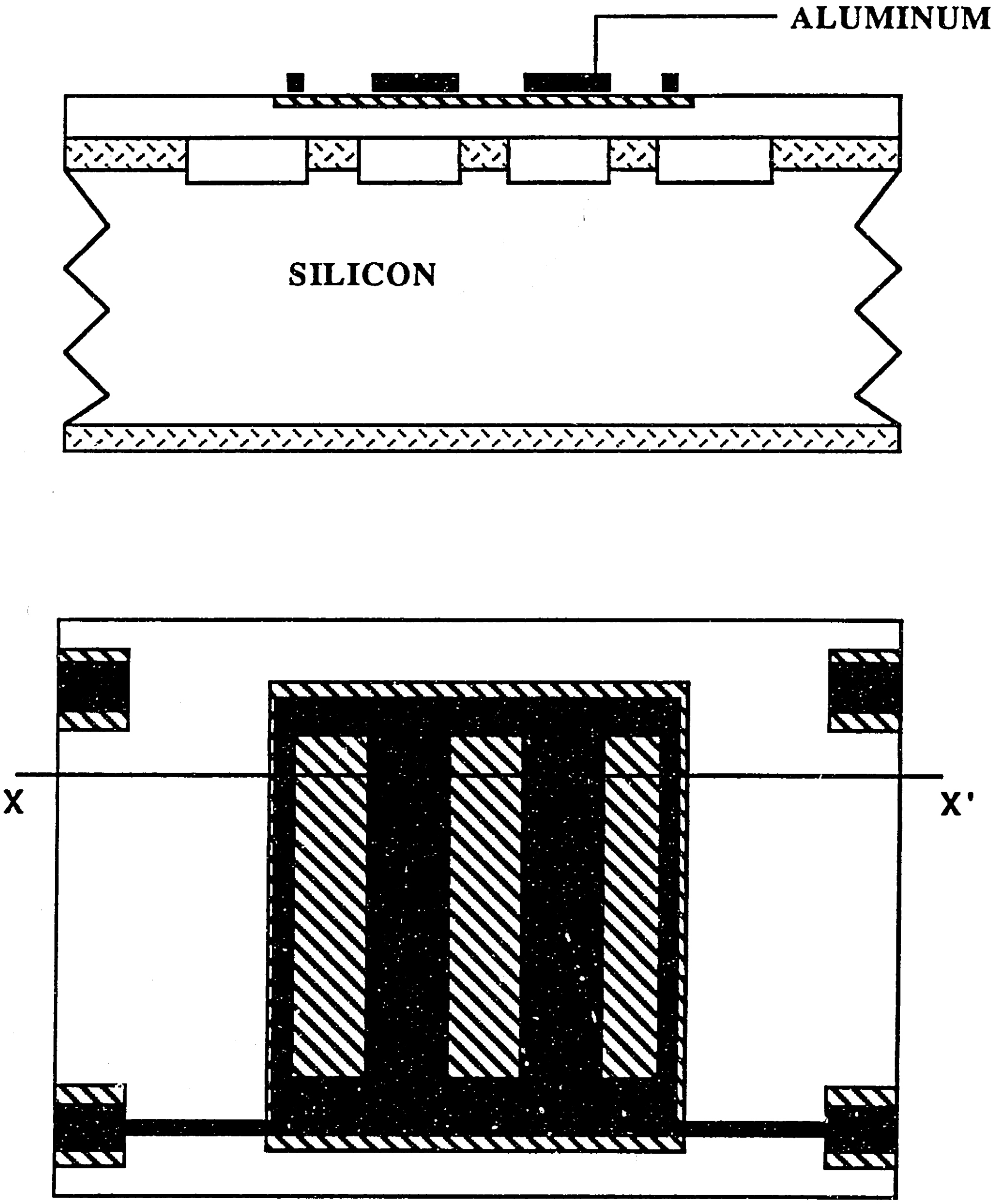

FIGURE 3-5: Deposit and Pattern Aluminum

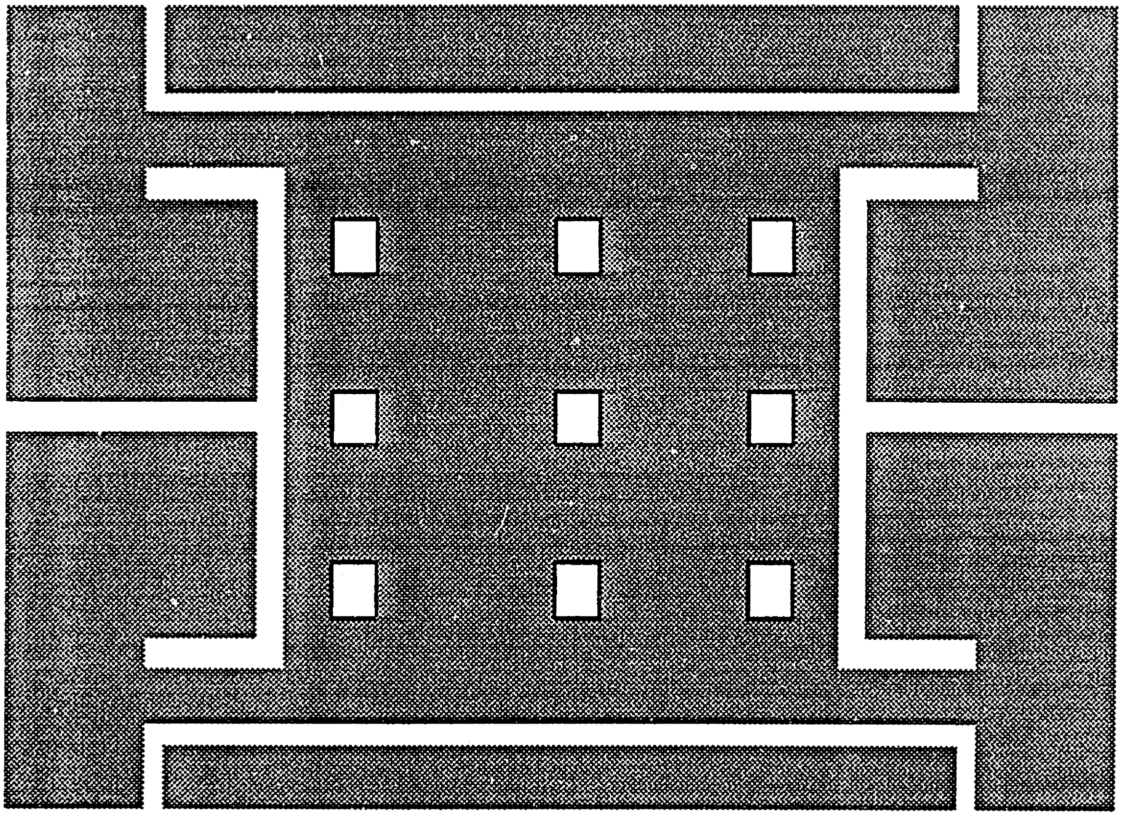

FIGURE 3-6: Silicon Trench Etch Pattern

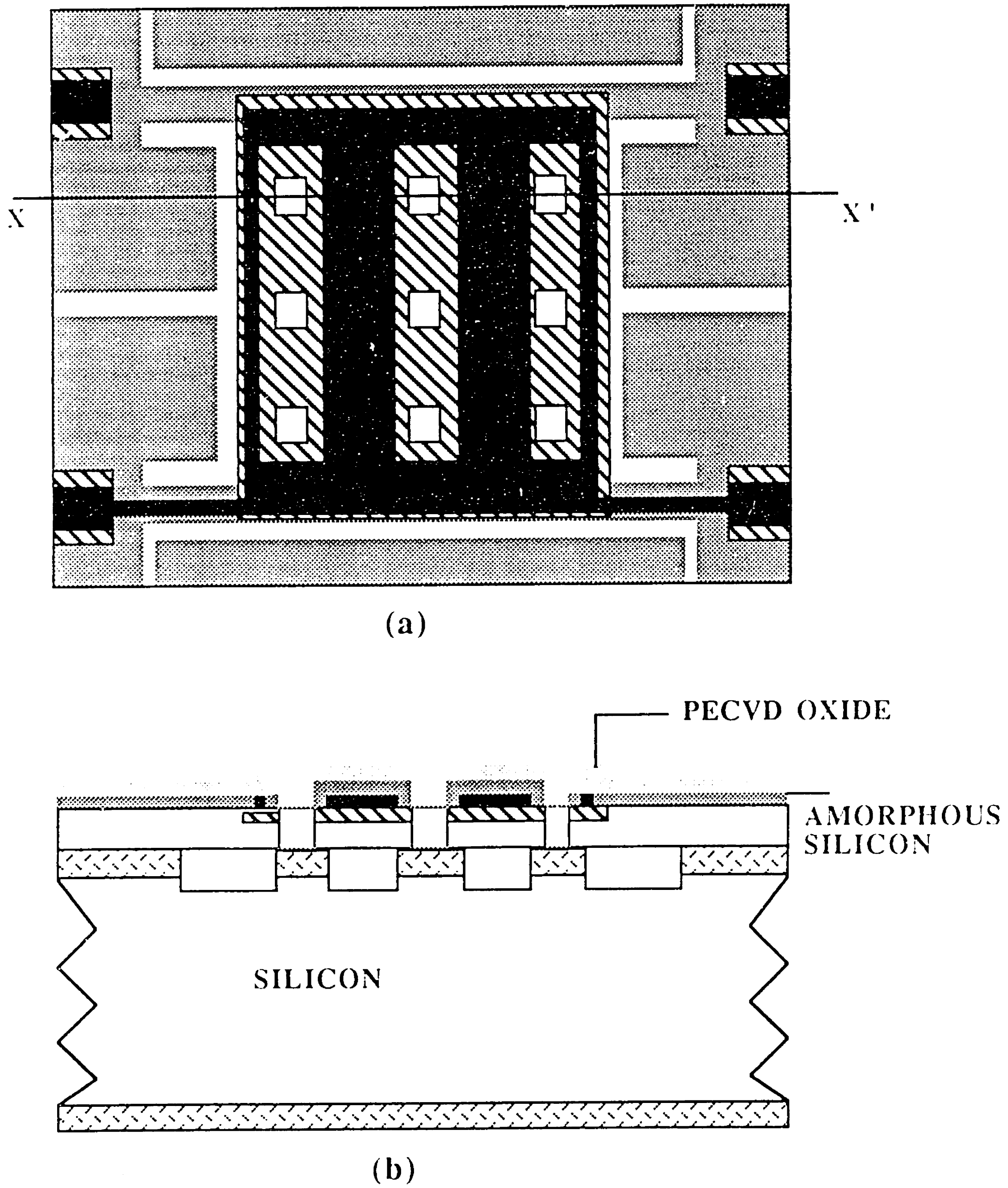

FIGURE 3-7: Silicon Trench Etching (a)Top View (b)Cross-Section

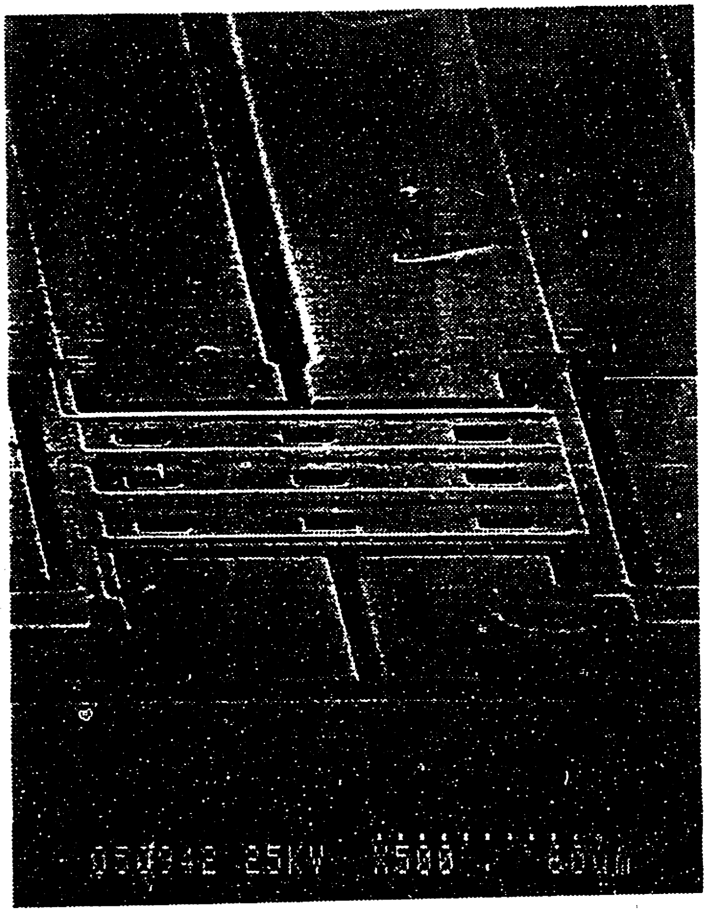

FIGURE 3-8: SEM of Floating-Element

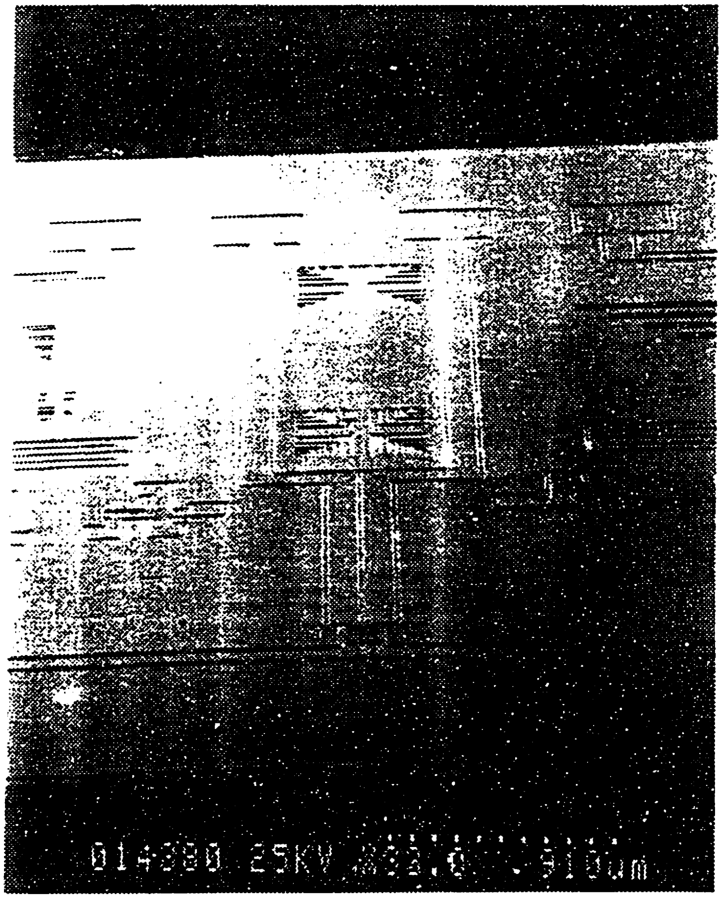

FIGURE 3-9: SEM of Sensor Chip

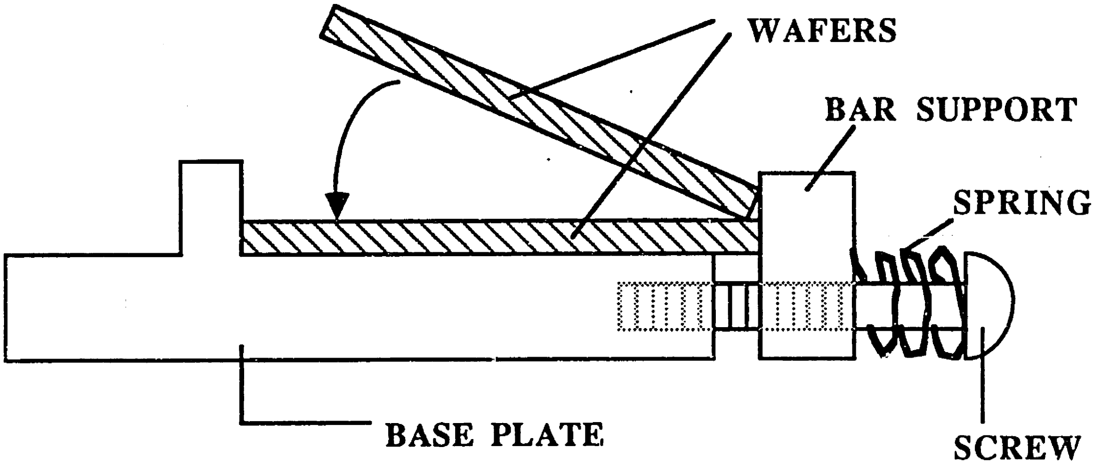

FIGURE 3-10: Bonding Jig

3.2 Wafer-Bonding

The mechanism of wafer-bonding has been introduced in section 1.3.1 and this section describes the procedure that has been adopted by us as part of a larger effort to fabricate microsensors using this technology. The process is done in the Technology Research Laboratory class 100 clean room which is inside the Microsystems Technology Laboratory (MTL) at MIT.

Wafers to be bonded are RCA cleaned and followed immediately by the hydration step consisting of a ten minute immersion in 3:1 H_2SO_4: H_2O_2 without any heating. Following this the wafers are dump- rinsed and spin-dried. Each pair of wafers are then placed into contact by using a jig constructed by co-worker Dan Sobek, shown in Figure 3-10. The jig is made of teflon and consists of a square plate with two posts and a separate bar support. The support is attached to the plate with a pair of screws that have springs inserted onto the shank. A wafer is placed polished side up with the flat resting on the bar. By adjusting the screws, a light amount of pressure is applied by the springs on the wafer which sits between the bar supports and the posts. A second wafer is then placed with the flat against the bar support and at an angle, as shown in the figure. This wafer is then released and allowed to fall and make contact with the first wafer. The purpose of the spring loaded screws and the bar are to align the flats together during the process. By allowing the wafer to fall into place in the manner described above air is expelled from between the wafers to improve the contact. A pair of tweezers are then used to press the two wafer firmly together and at this point, the wafers can be handled as a pair without separating. This contacting is followed by a high temperature cycle consisting of sixty minutes in dry oxygen at 1000°C. The temperature is ramped up from 600°C and at the end of the oxidation is ramped down to 800°C before removing the wafers. This is to ensure that no large temperature gradient exists between the oxide and the furnace ambient that may result in large thermal stresses. After the oxidation step, the wafers are now completely bonded.

A major issue regarding bonding is the presence of voids in the wafer. These are regions where bonding did not take place and may be due to particles trapped between the wafers, spikes that may arise in epitaxially grown layers or wafers that are not flat enough to make contact in these areas. Since the wafers are rigid, a small particle can result in large voids and as a result, a lot of attention is paid to ensure that the environment is as particle-free as possible. In order to check the quality of the bond, a wafer inspection system was constructed by co-worker Michael Huff, shown in Figure 3-11. It consists of of an infrared (IR) source, in this case a lamp, and a CCD camera that that is IR sensitive. The wafers, being transparent to infrared, will transmit these wavelengths to the camera. Any voids that exist would appear as interference fringes. The camera is connected to a monitor and a thermal printer to make copies of the image. Figure 3-12(a) shows a bad quality bond with plenty of voids and Figure 3-12(b) shows a picture of a good quality bond. The fringes near the flat did not bond because of the presence of the laser scribed identification numbers. For the wafers used in the shear-sensor process, we have been able to obtain good quality bonding in about 80% of the wafers. A good quality bond has at least 90% of the area bonded. As mentioned in section 3.1, the handle wafer has patterns on the oxide layer (Figure 3-2) and by inspecting them under the wafer inspection system and comparing them with wafers that do not have patterns, we are able to determine that the quality of the bonding is the same for both cases.

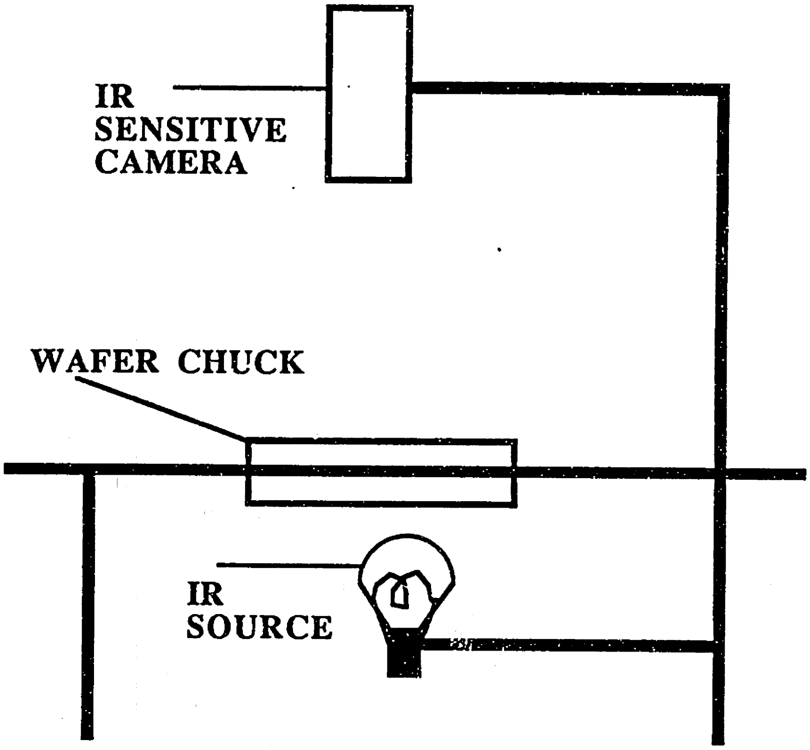

FIGURE 3-11: Wafer Inspection System

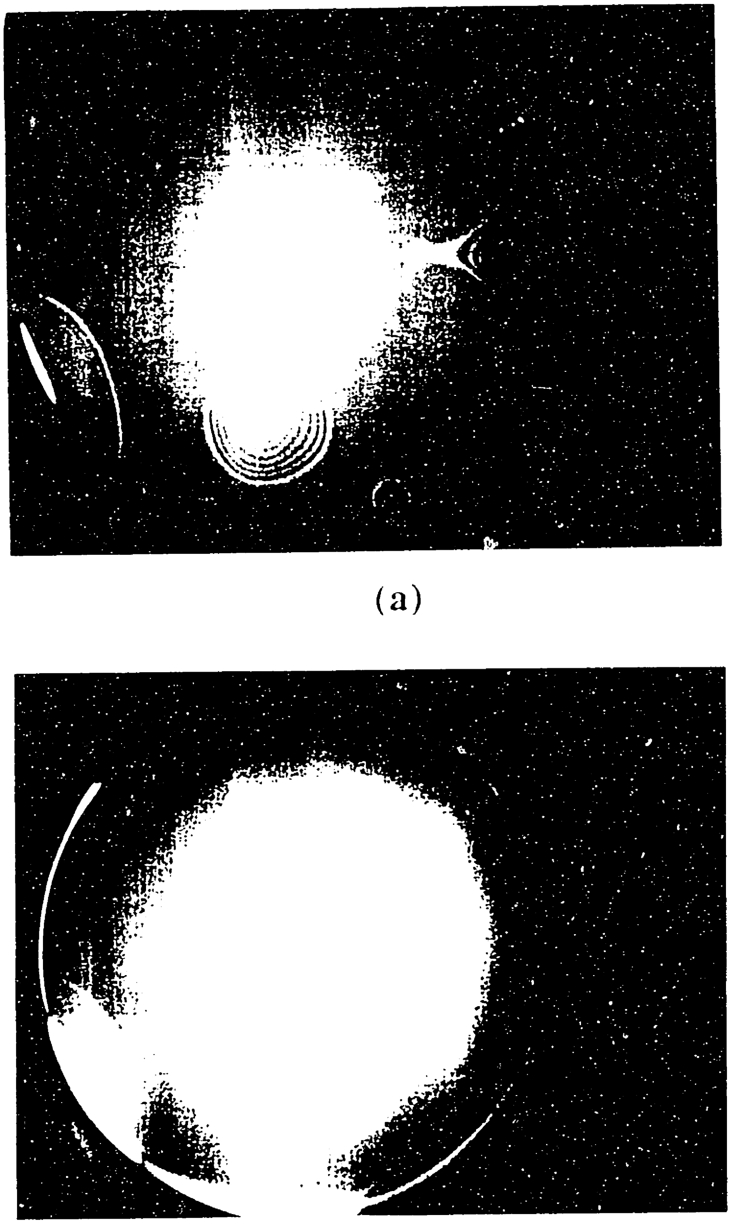
(a)

(b)

FIGURE 3-12: Bonding Quality (a)Voids (b)Good Bond

3.3 Wafer-Thinning

The device wafer used for the shear-sensor consists of a boron- doped layer with a lightly doped epitaxial layer grown on top of it (Figure 3.13(a)). These wafers were donated by Analog Devices. The boron layer is about 5μm thick and the doping profile is shown in Appendix B, with a peak of about $7 \times 10^{19} cm^{-3}$. The epi thickness is also 5μm. The etching process to thin the wafers consists of three steps as described below.

3.3.1 KOH Pre-Thinning

The bonded wafers are placed in polypropylene wafer cassettes and immersed in a stainless steel tub filled with KOH and the tub is is placed in a water bath with temperature control of ±0.1°C. The concentration of the KOH-water solution is 20% by weight prepared by dissolving KOH pellets in $18\mathrm{M}\Omega - cm$ de-ionized water. At this concentration, silicon has the highest etch-rate for a given temperature [32]. The temperature can be varied depending on the etch-rate desired and the amount of oxide that is available to passivate the handle wafer. The etch-rates for <110>silicon and silicon dioxide are [33]

$$R_{Si} = 7.86 \times 10^{9} e^{\frac{-0.56}{kT}} \quad \mu m/hr \tag{3.1}$$

$$R_{SiO_2} = 1.52 \times 10^{10} e^{\frac{-0.84}{kT}} \quad \mu m/hr \tag{3.2}$$

The etch-rates are in μm per hour and at high temperatures both R_{Si} and R_{SiO_2} increases with the ratio of $R_{Si} : R_{SiO_2}$ decreasing. Therefore, a thicker oxide is required to protect the wafer at elevated temperatures. For the sensor process, a temperature of 67°C was chosen, giving an etch rate of approximately 40μm per hour. This stage of the process is a timed etch and we would stop when the device wafer is 40 $\pm 5\mu$m thick (Figure 3-13(b)). The thickness is measured using a CaryCompar thickness comparator (LVDT).

3.3.2 CsOH p$^+$ Etch Stop

This part of the process utilizes the fact that alkaline solutions exhibit reduced etch-rates for heavily doped p$^+$ silicon, and we can use this to stop the etching at a desired thickness. KOH has higher etch rates than CsOH [8, 33] but only has

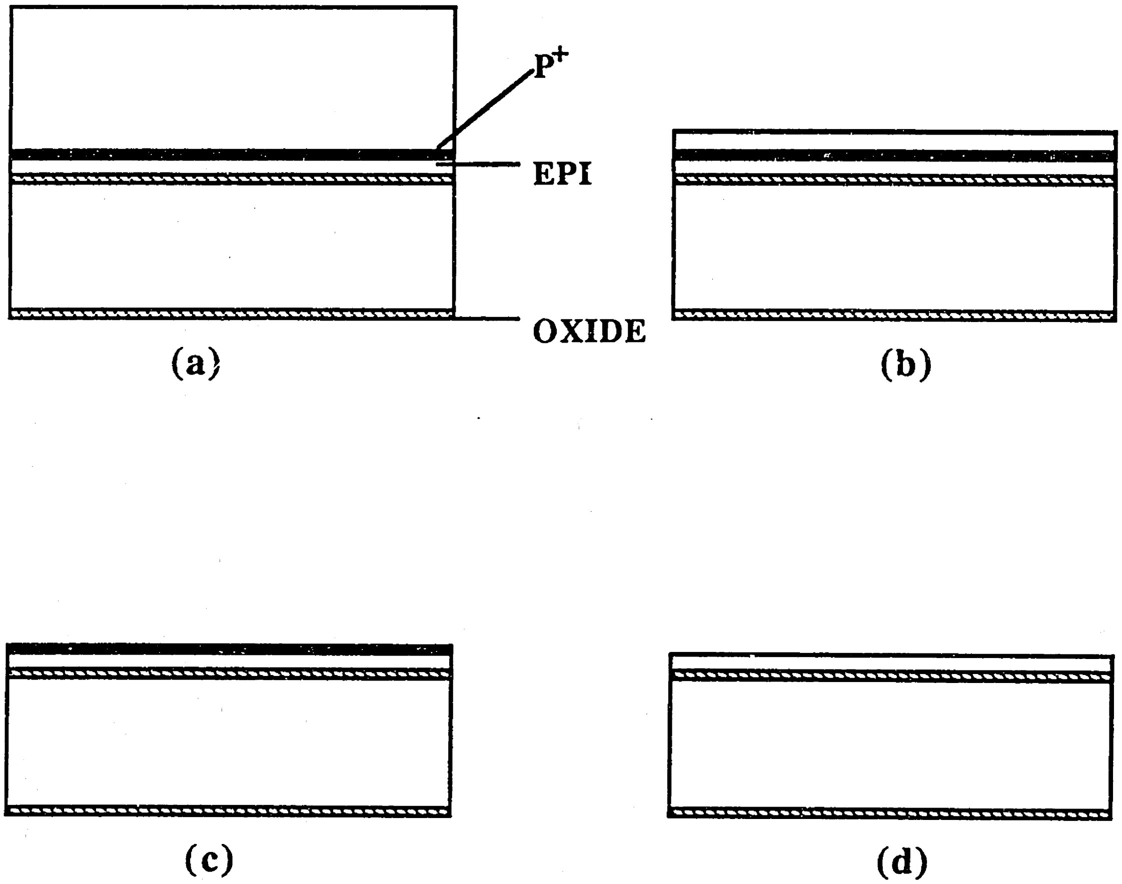

FIGURE 3-13: Wafer Thinning Process (a)Device Wafer with Epi (b)Pre-Thin (c)p^+ Etch Stop (d)p^+ Removal

significantly reduced etch-rates for doping $> 10^{20}cm^{-3}$ [32]. CsOH, on the other hand exhibit reduced etch-rates with doping $> 10^{19}cm^{-3}$. As a result, the pre-thin was done in KOH while the etch-stop was done in CsOH. The etch rate for <110>Si in CsOH at 60% concentration is

$$R_{CsOH} = 1.35 \times 10^{10} e^{\frac{-0.61}{kT}} \quad \mu m/hr \tag{3.3}$$

The etching was done in 60°C, 60% CsOH which has an etch-rate of 8μm per hour. When the p^+ region is exposed to the solution, etching is significantly reduced and this could be observed visually by the absence of bubbles in these areas. At this stage, large voids (if present) would have peeled off, exposing the underlying oxide. Once bubbling has ceased, the wafer was removed (Figure 3-13(c)). Slip planes and dislocations due to high boron concentrations could be observed on the surface as evidenced by a fine fabric-like texture. The roughness at this point was about 1000$\mathring{A}$ rms, as measured by a Dektak stylus profile measurement system.

3.3.3 Selective Removal of p^+ layer

Once the p^+ layer is exposed the etch stops and we could use another chemical formula to selectively remove the p^+ layer. Muraoka [34] has used a mixture of 8:3:1 CH_3COOH:HNO_3: HF. Etch ratios greater than 6000 with respect to lightly doped silicon have been reported. When the wafer was immersed into the solution, the solution turned brown indicating the presence of HNO_2. A brown stain appeared on the wafer when the process was completed indicating the presence of porous silicon in the lightly doped regions. The surface appeared much smoother compared to the p^+ etch-stop surface and the rms roughness is of the order of 100$\mathring{A}$. To remove the brown stain, a mixture of 97:3 HNO_3:HF [35] was used and this took approximately fifteen seconds. No changes were observed in the texture of the silicon film. At this stage, what remained was the lightly doped epitaxial layer on 1.4μm of oxide supported by a handle wafer (Figure 3-13(d)).

3.4 Ion-Implantation

The need for good ohmic contact between metal and silicon require a region of heavily doped silicon at the metal-silicon interface. For the shear-sensor wafers, the doping is n-type and as a result, the contact implant consists of arsenic at an energy of 80keV. At this energy, the projected range is close to the surface(500$\AA$). The dose used is $7 \times 10^{15} cm^{-2}$, making the surface heavily n-type. For the p-type wafers used in the devices to be discussed in chapter 5, the implant species is BF_2 at an energy of 20keV.

Masking material for the implant is photoresist that had been patterned. In order to prevent overheating in the resist that may cause difficulty in removing, the wafers are cooled using freon and the current is limited to less than 100μA. The resist is removed using an oxygen plasma in the asher.

The activation of the implants is done using a high temperature cycle. For the arsenic implants, the wafer is annealed at 850°C in dry oxygen for 1 hour. Because the silicon/SiO_2 segregation coefficient is > 1 [36] , the arsenic is rejected from the oxide and is concentrated at the surface. For the boron implant, activation is done at 900°C in nitrogen for 30 minutes. Boron has a segregation coefficient < 1 and any oxide grown would be depleted at the surface and therefore, a nitrogen ambient is required. The plots of the resulting implant profile after the anneal cycle simulated using Suprem for both types of implants are shown in Appendix C.

Since there are patterns underneath the 5μm film, gases are trapped in these patterned trenches. At elevated temperatures, the pressure is increased and there is an outward pressure acting on the film. A very thin film or a large pattern could result in pressure high enough to fracture the film or to plastically deform it, resulting in a permanently deformed surface. This effect has been observed by Huff [37]. In order to analyze whether we are below the critical temperature, we can calculate the pressure acting on the film. From [38], the plate deflection for circular membranes under pressure loading is

$$w = .662a^3 \left(\frac{qa}{Et}\right)^{1/3} \tag{3.4}$$

where a is the radius of the circle, q is the differential pressure, E is the Young's Modulus and t is the thickness of the film. The differential pressure could be calculated assuming the ideal gas law relation.

$$q = P_{Atm} - \frac{P_1 V_1}{V_1 - \Delta V_1} \tag{3.5}$$

For worst case result, we assume that the pressure is not relaxed ($\Delta V_1 \approx 0$). Therefore, the pressure at 900°C is $P_{900^oC} = \frac{0.8(1173)}{300} \approx 3.13 Atm$ or a differential pressure of

2.13 *Atm*. We have assumed that the residual pressure inside the cavity is 0.8 *Atm* [37] . Although the structure is not circular, we could again assume a worst case result by assuming a circle with the diagonal of the floating-element as the diameter. Therefore, $a = 84.9\mu\text{m}$. This gives a deflection $w \approx 1.06 \times 10^{-8}\mu\text{m}$ which is negligible compared to the $5\mu\text{m}$ thickness of the film.

3.5 Metal Passivation

A passivation film is needed to protect the aluminum lines from etching during the release step. The choice of material must take into consideration the following.

I. Deposition temperature must be below the melting point of metal and low enough to prevent diffusion of metal into silicon.

II. Step coverage needs to be conformal.

III. Residual stress of the film should be as low as possible.

IV. Ability to wire bond through the layer to make contact with the metal.

Based on these criteria, PECVD amorphous-silicon was chosen to passivate the metal because of its availability and evidence of its resistance to HF as reported by Tai [39]. Furthermore, this material is compatible with silicon and could be etched in the same step. The system used for this deposition was a Plasmatherm and the conditions of the deposition are given in Appendix D. The deposition temperature was 220°C, much lower than the sintering temperature of 375°C. We have also successfully bonded through this layer using an aluminum wedge bonder.

Initial test runs showed that while the film passivated the aluminum lines when immersed in HF, a longer duration in the acid resulted in attack of the aluminum lines near the trenches. This resulted from the native oxide layer that exists between the amorphous silicon layer and the single crystal silicon, where HF etches the native oxide and gradually attacked the metal. In order to overcome this problem, the wafers were dipped in 50:1 H_2O:HF for 20 seconds to remove any native oxide prior to entering the deposition chamber. This meant that a thicker metal was needed since the solution would attack the aluminum simultaneously. In the process, 5000Å of aluminum was deposited and it was estimated by SEM photos that about 3000Å of it remained after the HF dip. Further trial runs showed that this procedure allowed the aluminum lines to be passivated in excess of 10 minutes.

The deposited film for the sensors had a thickness of 5000$\AA$, measured by SEM and thinner layers could be attained in future runs. Figure 3-14 shows an SEM of a section of the chip where the native oxide has been underetched and the tensile stress of the amorphous silicon layer has caused it to bend upwards. The stress of this layer is discussed in section 3.7.

3.6 Silicon Plasma Etching

The trench etching is needed to define the floating-element and to isolate the metal lines that are at different voltages. A plasma-etching system was used and two different etching chemistries were experimented(SF_6 and CCl_4). For shallow trenches ($< 3\mu$m), the SF_6 based plasma was used because of its reproducibility and high selectivity with resist while for deeper trenches the CCl_4 based plasma was preferred because of its minimal lateral undercutting.

Figure 3-15 shows a shear-stress sensor that was etched using the SF_6 recipe. The etching conditions and parameters are given in Appendix E. The depth of the trench is 5μm and the mask used was the photoresist itself. It can be observed that a significant amount of lateral etching occurred during the process as evidenced by the sidewall angle. In order to determine the amount of lateral underetch, a wafer with 1μm of thermal oxide was patterned and etched down for about 10μm (Figure 3-16). The thin film at the top with the overhang is the oxide mask itself while the silicon that is etched is underneath. A large amount of bowing has occurred and the lateral etch was about 25 % of the trench depth. This results from the fact that the SF_6 etching mechanism is chemical in nature and as a result, is isotropic, leading to the undercutting [40]. The critical dimension in the shear-stress sensor is the etching of the tethers for the floating- element. With a width of 10μm and a depth of 5μm, lateral etching on both sides of the tether would amount to 50% undercut or only 5μm at the surface. This was unacceptable since the metal line width on the tether is also 5μm. Nevertheless, this recipe was used in the fabrication of the piezoresistor for calibration purposes (chapter 4) since the dimensions there were less critical and the trenches were only 1-3μm.

The CCl_4 recipe did not have any significant lateral etching and Figure 3-8 shows

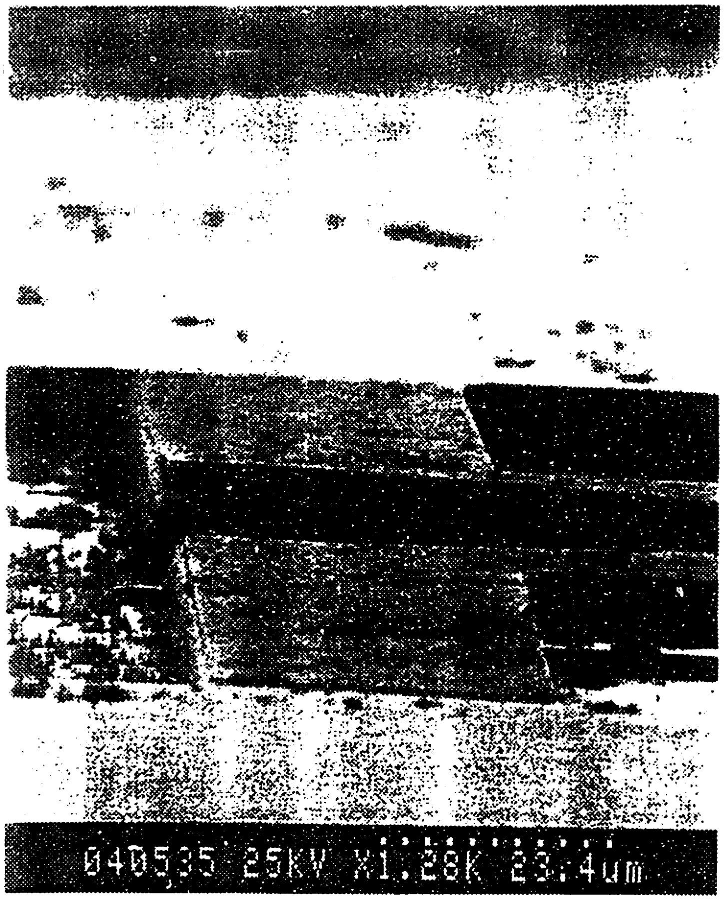

FIGURE 3-14: SEM of Amorphous Silicon Peeling

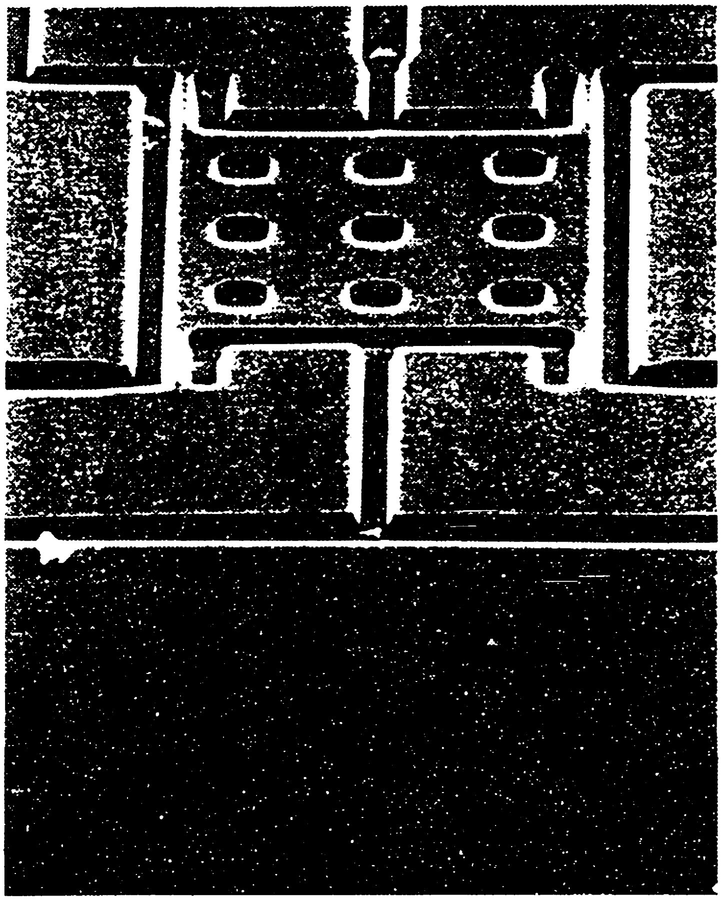

FIGURE 3-15: SEM of Trench Etch Using SF_6

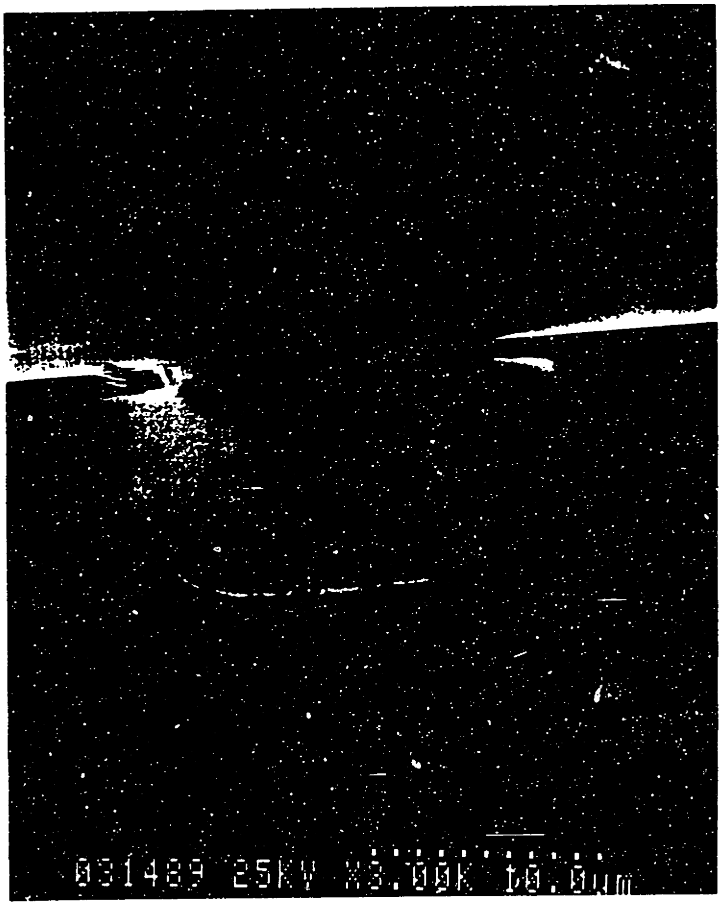

FIGURE 3-16: SEM Showing Undercutting Using SF$_6$

Table 3-1: Etching Data for SF_6 Recipe

Material	Etch Rate Å/min	Selectivity
Silicon	6900	
Photoresist	2700	2.5 : 1
Thermal Oxide	300	23 : 1

a shear-stress sensor that was etched using this recipe. Figure 3-17 is an SEM of a sensor that was sawed through the tethers and it can be observed that the sidewall angle is approximately 90°. The etching parameters are also given in Appendix E. It has been proposed that in chlorine containing gases [41], deposition of material on the surface of the trench wall masks the silicon from incoming reactive- ion species and ions. Other factors such as bias and pressure play a role as well but in chlorine gases, the chlorine ions react with silicon to form $SiCl_4$ and it has been reported [42] that $SiCl_4$ plays a major role in passivating the sidewalls.

While the etch is anisotropic, the disadvantages of this recipe are its reproducibility and sensitivity to wafer and etcher conditions. Sputtered material from the etcher or mask may redeposit on the wafer and inhibit etching, forming 'silicon towers'. Figure 3-18 is an SEM of a trench etch showing the 'towers'. This effect is known as micromasking and has been investigated by Horowitz and Hess [43, 44]. Finally, because the etch mechanism is mainly ion bombardment, the selectivity with respect to the mask is less favorable and for the 5μm process, a 1μm PECVD oxide mask was used. The oxide mask was etched using the patterned resist as the mask and the resist was then stripped before entering the chamber for the plasma etch. Clear trenches were obtained by ensuring that the etch chamber was clean. Alternatively, the wafer can be given a short timed etch using the isotropic SF_6 recipe right after the CCl_4 etch to remove the 'towers'.

In order to determine the selectivity of the silicon etch with respect to various types of masks, an experiment was carried out which consisted of patterning the mask and measuring the amount of etching that took place for both the silicon and the mask, measured with a Dektak. The experiment is described in Appendix F and Tables 3-1 and 3-2 summarize the results for both the SF_6 and CCl_4 recipe.

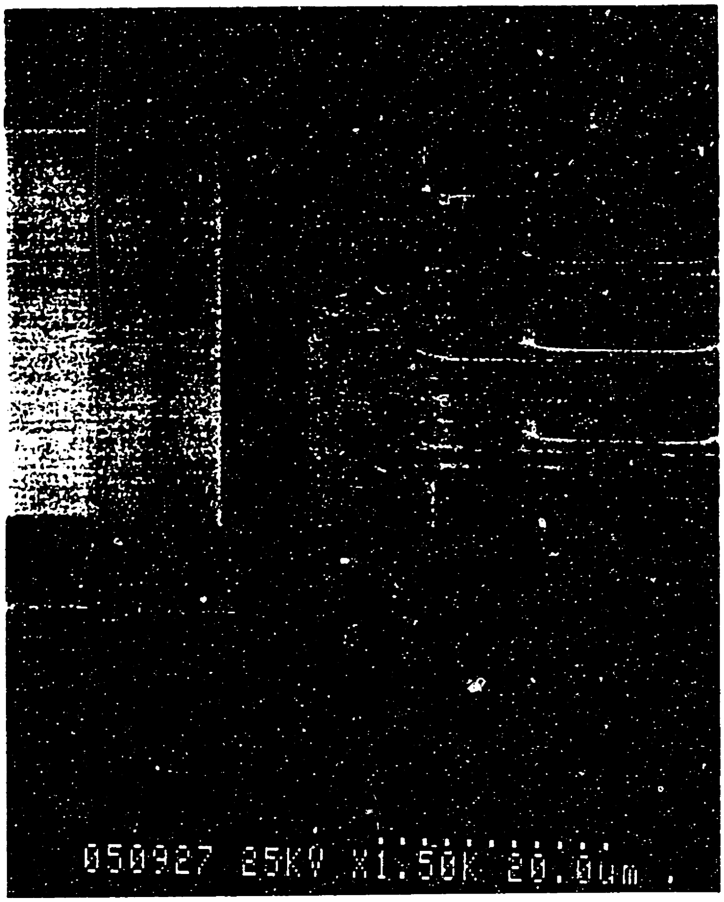

FIGURE 3-17: SEM of Trench Etch Using CCl_4

Table 3-2: Etching Data for CCl_4 Recipe

Material	Etch Rate Å/min	Selectivity
Silicon	4500	
Photoresist	3500	1.3 : 1
Thermal Oxide	730	6.2 : 1
PECVD Oxide	890	5.1 : 1

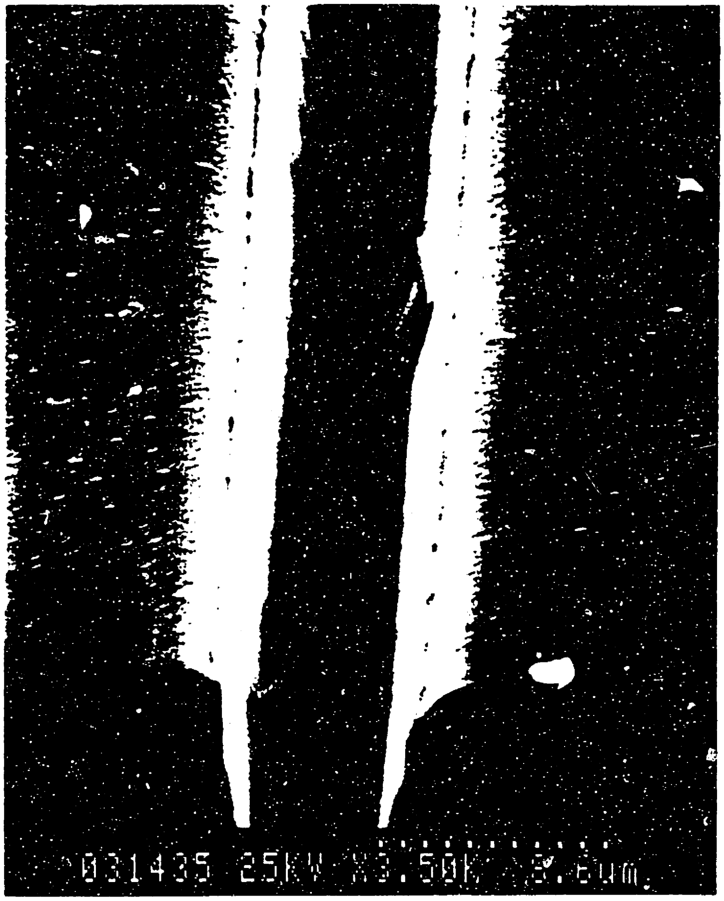

FIGURE 3-18: Silicon 'Towers' from CCl_4 Recipe

3.7 Sensor Release

This section describes the process of removing the sacrificial oxide layer underneath the floating-element. As described in section 3.1, there are two versions of the oxide mask. In version A where the oxide underneath the floating-element has been completely removed prior to bonding, no release step is necessary while in version B, a small amount of oxide remains and a release process is required. In version A devices however, the alignment of the trenches to the oxide pattern is critical and any offset would result in asymmetry in the device and a short release step is then required to free the entire element.

The wafers were diced into individual chips and released by a timed immersion of the chip in a 49% (by weight) HF solution, a 10 minute DI water rinse, 1 minute of immersion in methanol and drying with a nitrogen gun. The timed etch in HF depends on the amount of oxide that needs to be removed and the residual stress of the silicon film. Furthermore, HF that is exposed to the atmosphere gets depleted rapidly and that will affect the etch time as well. The DI rinse was done by diluting the HF solution in a cascade until all the HF was removed(10 minutes). This allowed a gradual dilution of the HF and prevented the floating-element from getting stuck to the silicon handle wafer due to surface tension. If the chip were withdrawn immediately from the HF solution, the silicon surfaces would de-wet, and the surface tension between the two surfaces that are close together would cause the clamping.

In order to determine the time required to undercut the oxide, several chips were etched at 30 second intervals and inspected under a microscope to see if the release was completed by examining the squares that were present on the chip. Figure 3-19 shows an SEM of the squares that were fabricated. When the oxide underneath the sensor is completely etched, the squares will be lifted off. Some devices were made without having any metal or amorphous silicon passivation and it was determined that the etch rate was approximately 1.5μm - 2μm per minute. The timed etch took about 4.5 to 5 minutes in this case. For the devices that had metal and amorphous-silicon passivation, HF immersion took only 1.5 minutes. Furthermore, the serpentine-resistor structure was also released and curled upwards (Figure 3-20). By using a micromanipulator to peel off the film , oxide can still be observed on the surface, shown in Figure 3-21. This indicates that the amorphous silicon layer is under tensile stress and when the oxide is released, a net upward bending moment exists that tends

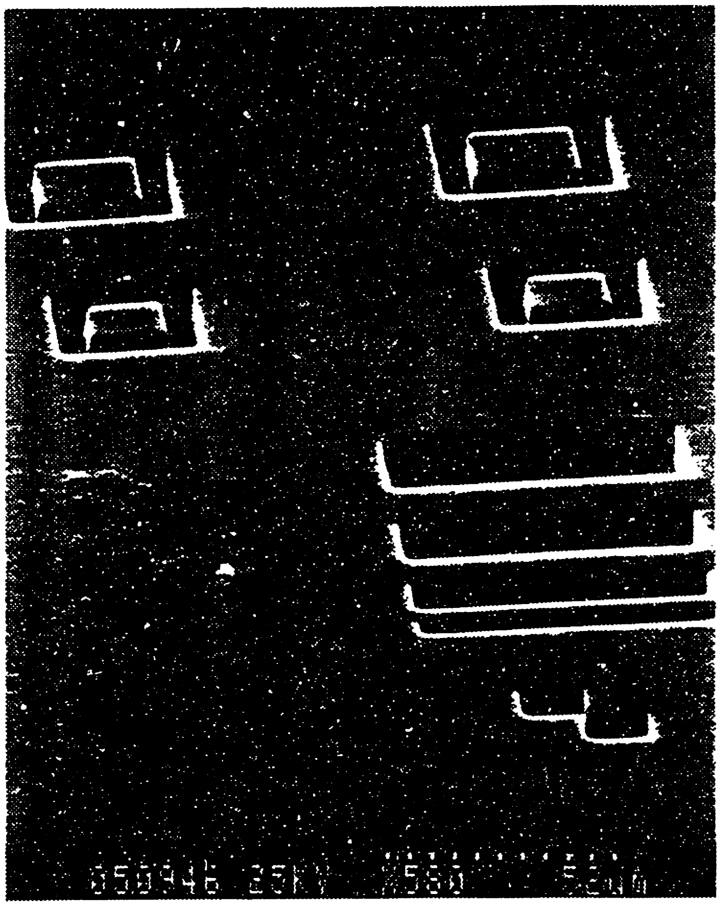

FIGURE 3-19: SEM of Squares for Release Endpoint

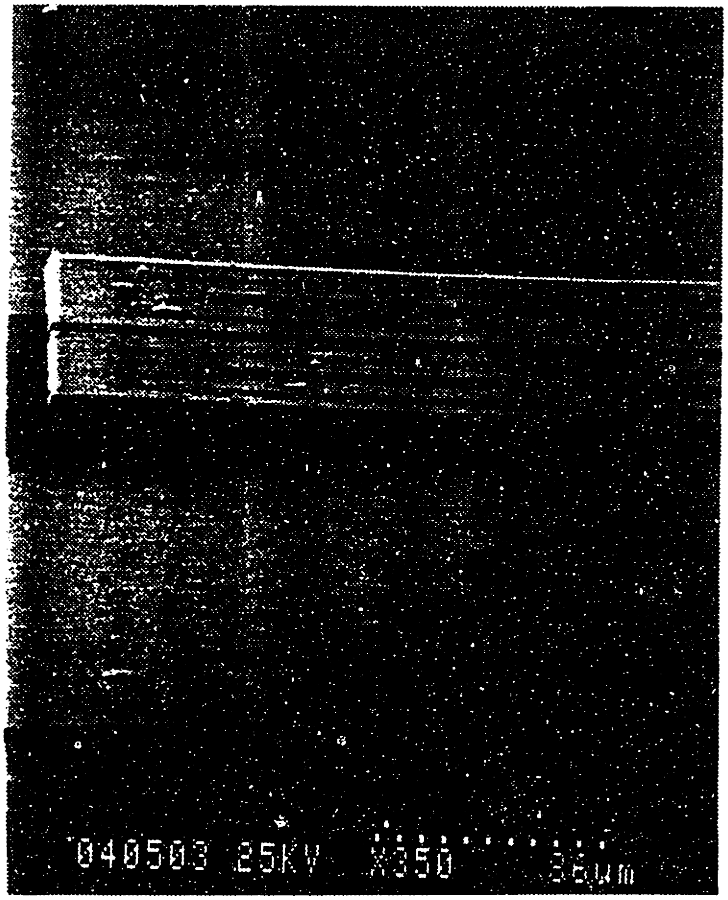

FIGURE 3-20: Peeling due to Stress in Amorphous Silicon

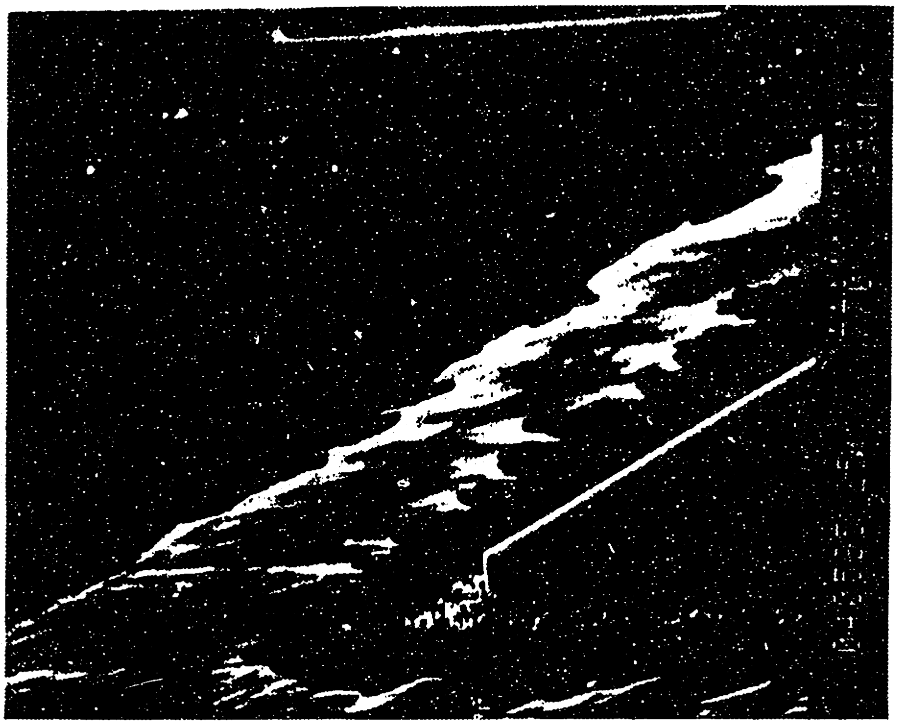

FIGURE 3-21: Oxide Underneath the Film

to accelerate the undercutting. We can calculate the amount of residual stress in the amorphous-silicon layer by using the model derived by Schmidt [1] for a composite cantilever beam. The radius of curvature of the beam is

$$\rho = \frac{L^2}{8\delta} \tag{3.6}$$

where L is the length of the beam, δ is the tip deflection and ρ is the radius of curvature. Measurement of the tip deflection was done using an interferometer and for the 100μm long cantilever structure, the tip deflection was 1.35μm, giving a radius of curvature of 925μm.

The stress in the amorphous-silicon is then related to ρ by

$$\sigma_{\alpha-Si} = \frac{t_{Si}^2}{6t_{\alpha-Si}}\left[\frac{E_{Si}}{\rho}\right]\left[1 + 4\frac{t_{\alpha-Si}E_{\alpha-Si}}{t_{Si}E_{Si}}\right] \tag{3.7}$$

We assume that $E_{\alpha-Si} \approx E_{Si} = 200GPa$, $t_{\alpha-Si} = 5000\AA$ and $t_{Si} = 5\mu$m. Therefore, $\sigma_{\alpha-Si} \approx 2.5 \times 10^9 Pa$ or $\approx 1\%$ of the Young's Modulus of silicon.

To minimize the amount of lateral undercutting, release using vapor HF was explored. The setup is shown in Figure 3-22 where the chip is suspended by a teflon plate with a machined hole, and the plate rests over a beaker of HF. The rectangular chip does not cover the hole entirely and the gaps allow the HF vapor to escape. Therefore, a smaller beaker is used to cap the entire plate to ensure that the HF vapor remains in the enclosure. It was found that this method helped eliminate the peeling problem but the amount of time required to release the sensor was dependent on the positioning of the chip over the plate and the angle of inclination. The time needed to fully release the device was between 3 to 5 minutes. If the chips were overetched, the structures would begin to peel.

Alternatively, the thickness of the amorphous-silicon layer could be made thinner (<1000 $\AA$) and the conditions of the deposition could be varied to reduce the amount of stress.

3.8 Electrical Properties Characterization

Section 3.8.1 presents the results of measurements done on the test structures using a HP4145 parameter analyzer with the measurements done at room temperature while section 3.8.2 shows the resistance vs. temperature data for the silicon film.

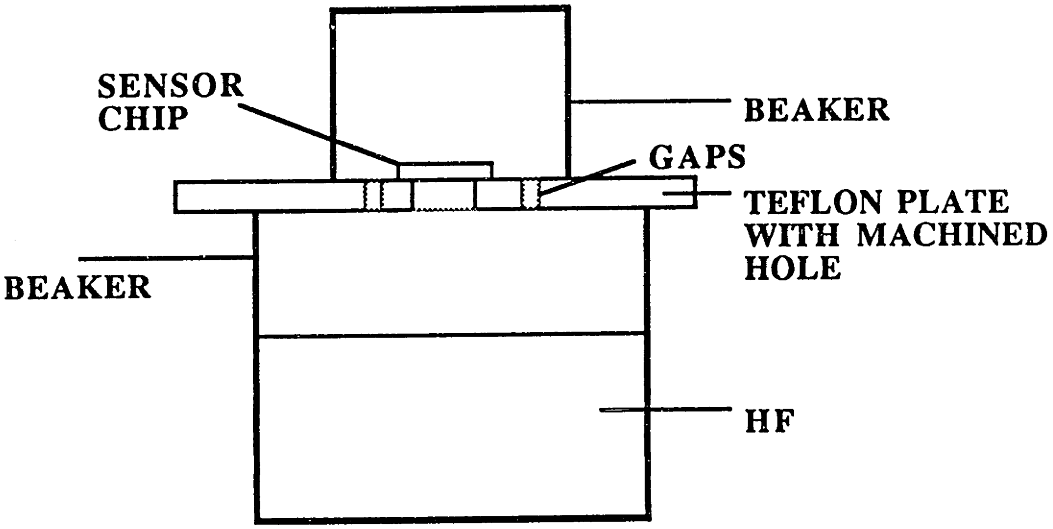

FIGURE 3-22: Vapor HF Set-Up

3.8.1 Test Structure Results

Van de Pauw

The sheet resistance is calculated from the relation

$$R_s = \frac{\pi}{ln2}\frac{V}{I} \;\; \Omega/\Box \tag{3.8}$$

The measured sheet resistance for the structure was $10.8k\Omega/\Box$. Using the film thickness of 5μm, the resistivity is $\rho_{Si} = 5.43\Omega cm$. From $\rho = \frac{1}{q\mu_n n}$ the doping concentration of the epitaxial film was $n = 7.7 \times 10^{14} cm^{-3}$ assuming $\mu_n = 1500 cm^2/V - s$

Serpentine Resistor

This structure consists of a 260 square aluminum line. The measured resistance was 22.8Ω, giving an aluminum sheet resistance of $R_{S_{Al}} = 8.7 \times 10^{-2}\Omega/\Box$. With a thickness of $3000\mathring{A}$, $\rho_{Al} = 2.6 \times 10^{-6}\Omega cm$.

Contact Resistance

The measured contact resistance of the 1600 μm^2 area was 1Ω. Multiplying by the area gave a value of $16{\times}10^{-6}\Omega cm^2$.

3.8.2 Resistance vs Temperature

The 5 square resistor was tested for its temperature dependence by heating the chip with a hot chuck with the temperature measured by a thermocouple. The experiment was done in the dark and the resistance was measured by a Keithley 179A Multimeter. Figure 3-23 shows the plot of the measurements up to 320°C. The resistor is linear up to 220° C before it rolls off indicating that the silicon film has gone intrinsic. From [29],

$$n_i = \sqrt{N_c N_v e^{\frac{-E_g}{2kT}}} \tag{3.9}$$

where n_i is the intrinsic carrier concentration, N_c and N_v are the effective density of states at the conduction and valence band respectively and E_g is the bandgap of silicon. At 493K, $n_i = 3 \times 10^{14} cm^{-3}$ and this is in good agreement with the results of the previous section.

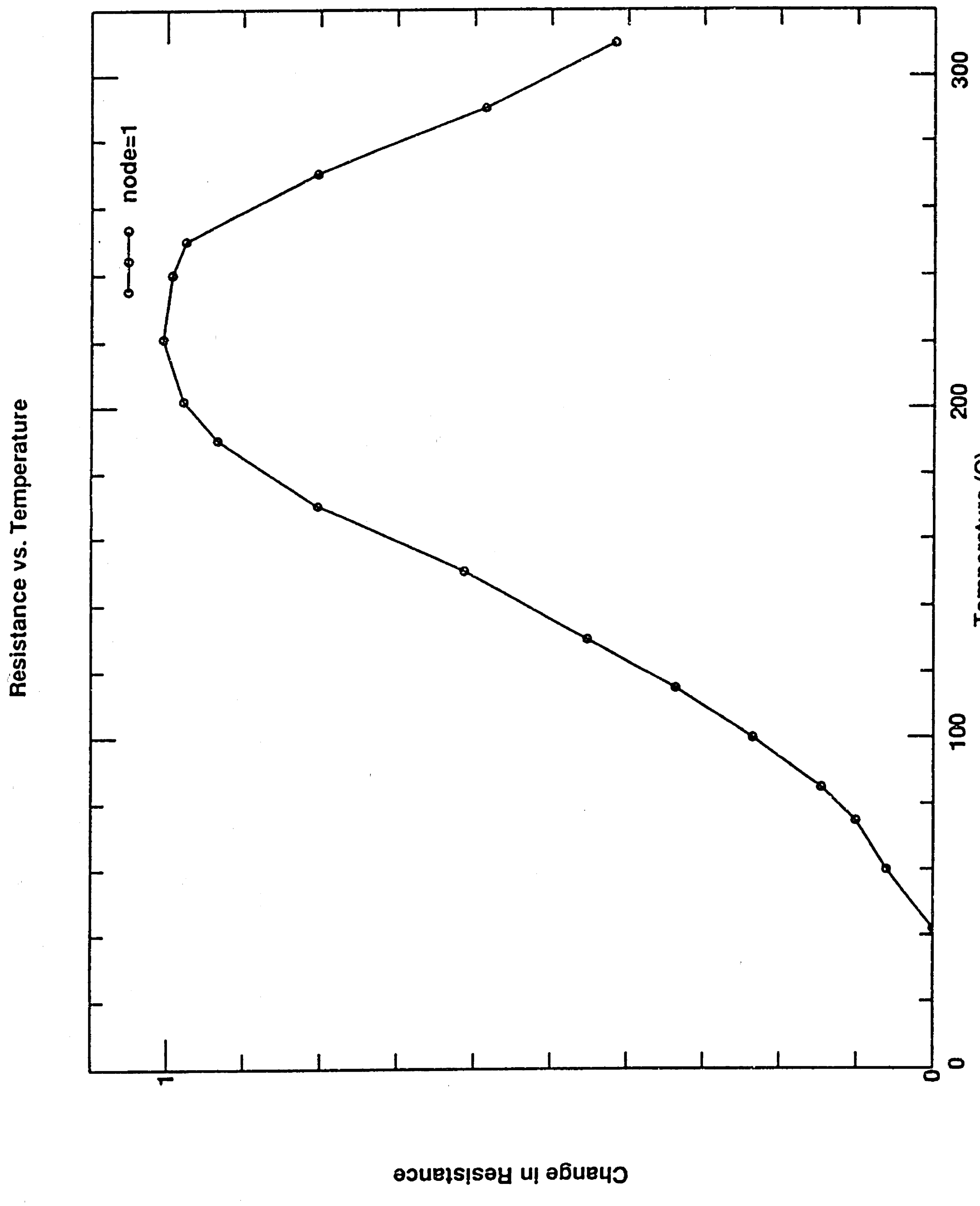

FIGURE 3-23: Plot of R vs. T

4

Piezoresistance Measurements

This chapter presents the results of experiments that were conducted to measure the gage factors of dielectrically isolated single crystal silicon. Section 4.1 introduces the method used to determine the gage factors and section 4.2 describes the fabrication process. The data for the measurements are summarized in section 4.3.

4.1 Experimental Method

The method described below is adapted from the work done by Burns [45] for the purpose of characterizing polysilicon piezoresistors. Figure 4-1 shows a top and side view of a cantilever with resistors mounted on the surface. If one end of the cantilever is clamped while the other end is deflected, the resistors experience a certain amount of strain that varies linearly with the tip deflection. The longitudinal strain is given by [46]:

$$\varepsilon_l = \frac{3d(a-x)h}{2a^3} \tag{4.1}$$

where d is the tip deflection, a is the distance from the clamped end to the free end, x is the distance from the clamped end to the resistors and h is the cantilever thickness. This equation is true for wide cantilevers, where the resistors are located far from the edge. As observed in the figure, there are three orientations of interest and they are located parallel, perpendicular and at 45° to the axis of the cantilever. For the longitudinal resistor the gage factor is given by

$$G_{par} = \frac{(\Delta R/R)_l}{\varepsilon_l} \tag{4.2}$$

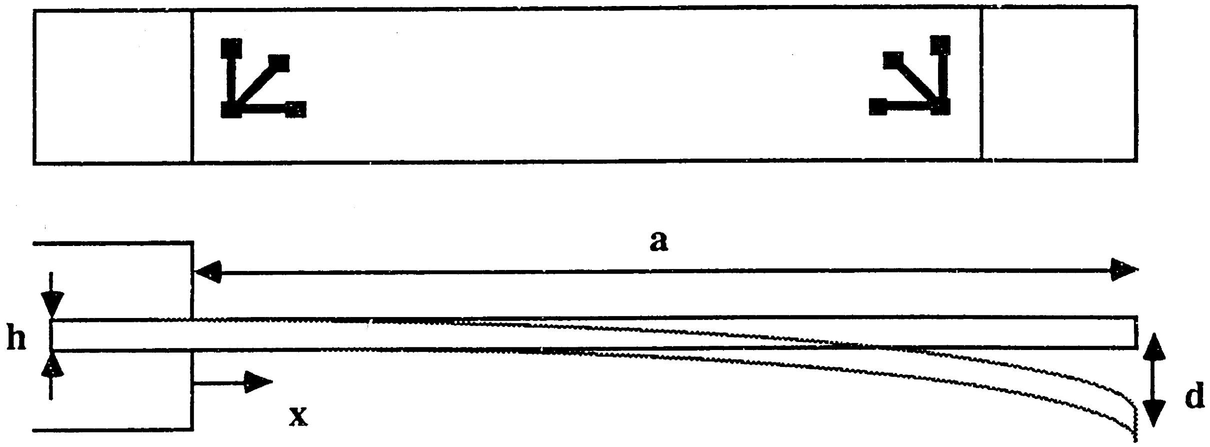

FIGURE 4-1: Cantilever Used for Measurement of Gage Factors

where $\Delta R/R$ is the fractional change in resistance for the longitudinal resistor. Similarly, the perpendicular gage factor, defined as the change in resistance for a structure strained transversely is given by

$$G_{per} = \frac{(\Delta R/R)_{tran}}{\varepsilon_l} \tag{4.3}$$

Finally, we can use the resistor oriented at 45° to determine the gage factor for shear strain. This resistor experiences both lateral and transverse strain in addition to the shear strain, therefore the gage factor is given by

$$G_s = \frac{(\Delta R/R)_s}{\varepsilon_l} - \frac{G_{par} + G_{per}}{2} \tag{4.4}$$

The measurements are done using an apparatus constructed by Rivenbark [47] as part of his Bachelor's thesis and has been successfully tested using p^+ bonded wafers. Each cantilever is mounted on an aluminum plate that has a milled recess and is fastened by a cap. Holes are drilled in the aluminum plate so that insulated copper wires can be fed through. An aluminum wedge bonder is used to make contact between the copper wires and the bonding pads. This plate is then inserted into a box assembly which has a micrometer mounted at the other end and serves to deflect the cantilever and to measure the amount of deflection.

4.2 Fabrication

Figure 4-2 shows the layout of the piezoresistor test structures for a full 4" wafer. It is a three mask process and there are seven cantilevers on each wafer with dimensions of 7cm × 1cm. Each cantilever consists of two sets of resistors located at each end and in each set there are three resistors with orientations parallel, perpendicular and at 45° to the longitudinal axis of the cantilever. Each resistor has dimensions of 10μm × 3000μm. Diagnostic structures are located at the center of each cantilever.

The fabrication process is similar to the floating-element process as described in section 3.1. A handle wafer is oxidized to obtain 1.4μm of oxide and is then bonded to a device wafer which is identical to the one used for the sensor fabrication. The device wafer is thinned following the steps described in section 3.3. This is followed by the first photolithography step to define the implant areas for the metal contacts. Prior to the implant the wafer is subjected to a timed (30 seconds) plasma etch using the SF_6 recipe. The purpose of this step is to create some topology on the wafer for future mask alignment. The implant specie is arsenic at an energy of 80keV and a dose of 7×10^{15}cm^{-2}. Figure 4-3 shows the cross sections of the wafer at the end of each photolithography step and Figure 4-3(a) illustrates the implant areas and the shallow trench caused by the timed etch. The resist is then stripped and the wafer is annealed at 850°C in dry oxygen for sixty minutes. This is followed by the deposition of 1μm of aluminum using electron-beam and the metal is then patterned in the second mask step (Figure 4-3(b)). Sintering is done at 375 °C in a nitrogen ambient. The resistors are then defined in the third mask step and etched using the CCl_4 recipe(Figure 4-3(c)). The detailed fabrication steps are given in Appendix A. The process described above is for the Bond-and-Etch-Back-Silicon-on-Insulator (BESOI) wafers, identical to the ones used for the sensor process. We have also fabricated piezoresistors on wafers that have been bonded and mechanically polished to a thickness of 3μm and Zone Melt Re-crystallized (ZMR) wafers. The fabrication steps for these wafers follow that of the BESOI wafers except that they do not need the bonding and wafer thinning steps. Also, since the mechanically polished wafers are p-type, the implant specie used was BF_2 at an energy of 20keV and a dose of $7 \times 10^{15} cm^{-2}$.

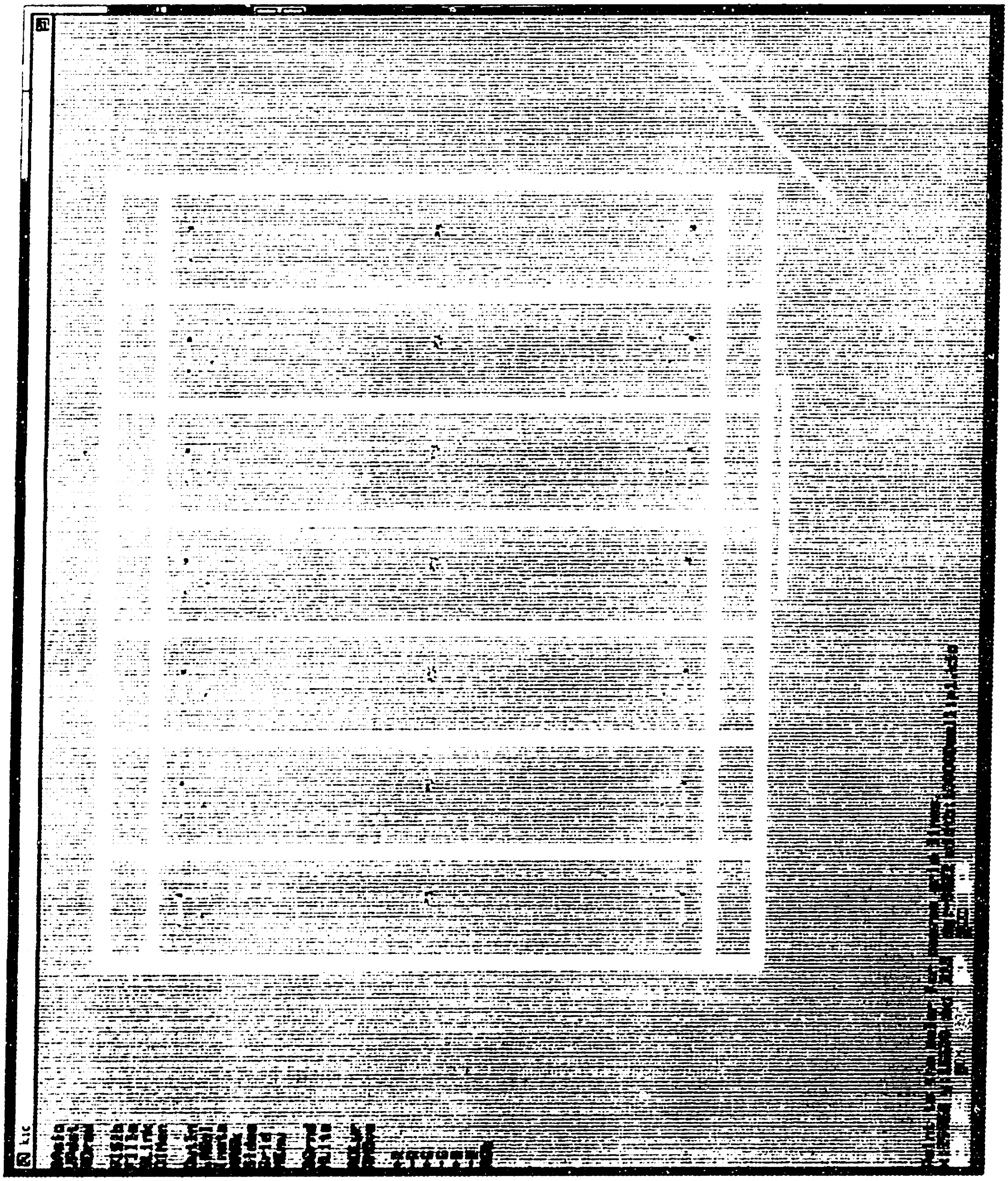

FIGURE 4-2: Layout of Piezoresistor Cantilevers

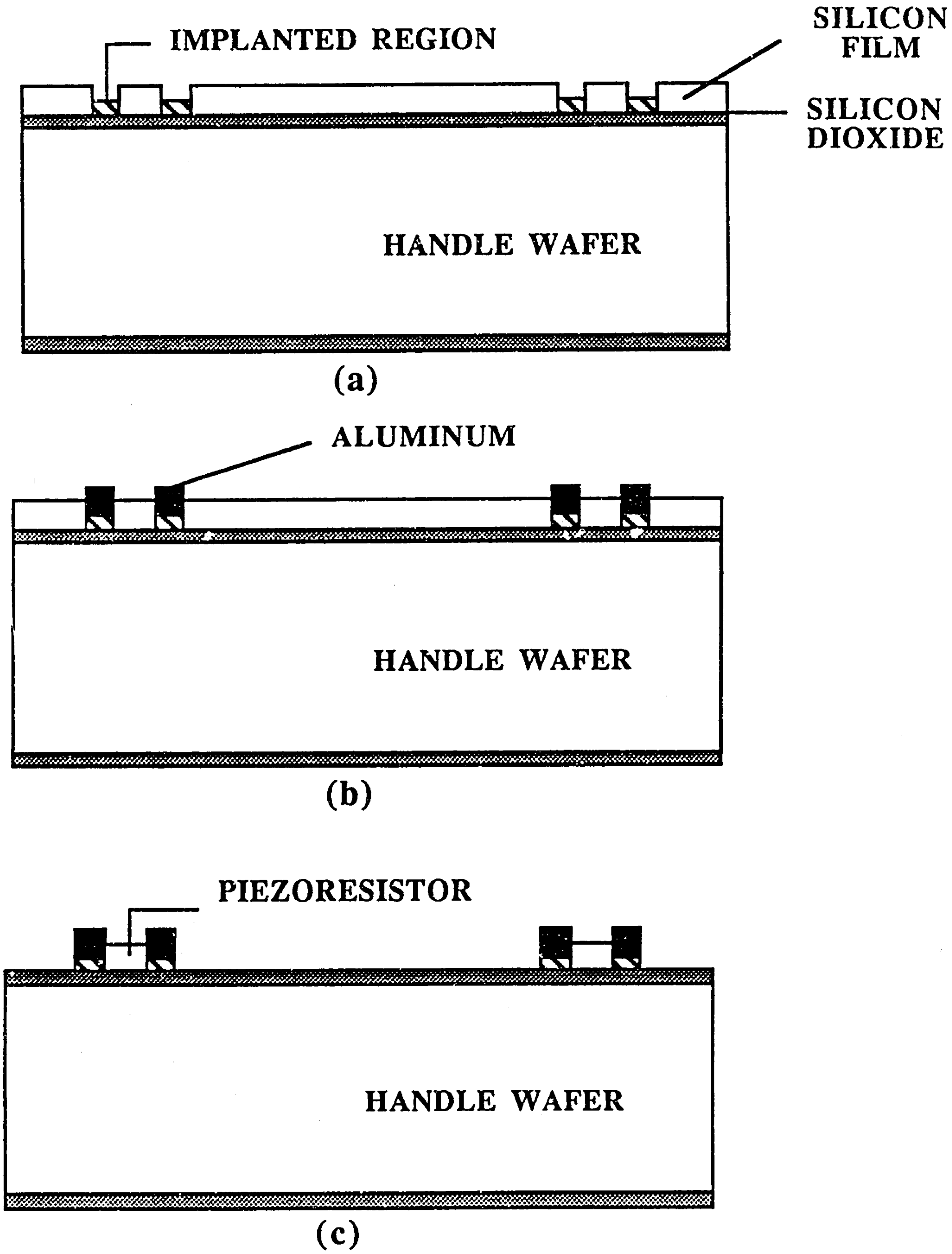

FIGURE 4-3: Fabrication Steps. (a)Ion-Implantation (b)Metal Pattern (c)Trench Etch

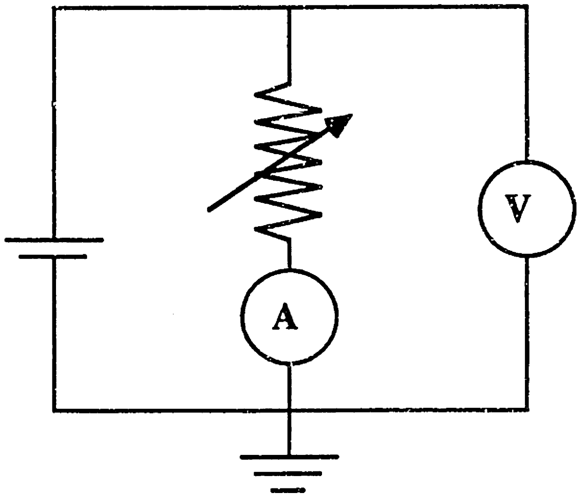

FIGURE 4-4: Circuit Schematic of Electrical Setup

4.3 Results

When the cantilever has been mounted and wire bonded, measurements can be obtained of the gage factors. Since these resistors are lightly doped and there are 300 squares in each of them, typical resistance values are in the order of 10MΩ. A 10V potential difference would only result in a current of 1μA and an ammeter with high sensitivity is required. The device also needs to be isolated from stray electromagnetic fields. As a result, all measurements are done in a Faraday cage and in the dark. Figure 4-4 shows the schematic of the setup. A HP4140B supplies both the voltage (0.1V - 10V) and an ammeter with pA sensitivity. The voltmeter is a Keithley TRMS 179A Multimeter. Before mounting the cantilever to the aluminum plate, the oxide on the substrate/backside of the cantilever is stripped in HF and silver paint is applied on the surface to provide electrical contact to the plate. The plate is grounded during measurements. The micrometer used is a Mitutoyo 350-712 and has micron sensitivity. The measurements are done at room temperature and the resistors have $< 100 >$ orientation.

4.3.1 BESOI Wafers

These are wafers used in the fabrication of the shear-sensor. They are n-type and the measured resistance of these devices are in the order of 3.5MΩ or 11.5k Ω/□. However, observations show that this value drifts upwards when the potential is continuously applied, and does not attain a stationary value. Further tests show that there is a significant amount of leakage from the 5μm silicon film through the oxide dielectric to the silicon substrate. This measurement is made with one of the bonding pads at positive potential and the substrate at ground potential. An I-V plot of the leakage is shown in Figure 4-5. Since the effect is non-linear the resistance cannot be determined. With a 1V potential difference, the leakage current is around 40nA for a bonding pad area of $1.96\times10^{-4}cm^2$ and this current scales according to the size of the pads. This gives us a value of approximately 200μA $/cm^2$. It has been speculated that [48] this phenomena may be caused by a 'cracked' oxide, created during the course of the fabrication. The resistance that is expected of the piezoresistors is 3.2MΩ and for a 1V potential drop, the current through the resistor is 300nA which is only an order of magnitude larger than the leakage current, partly explaining the drift that is observed in these devices. Because of this complication, no measurements can be made of the gage factors. The leakage needs to be investigated further and solved if circuits are to be fabricated using these wafers.

4.3.2 Mechanically Polished Wafers

These wafers are p-type and use wafer-bonding technology similar to ours except for the anneal cycle and the oxide thickness which is 1μm. Contrary to what is observed in the BESOI wafers, these wafers do not have any observable leakage as measured by the picoammeter. The measured resistance of these devices are of the order of 200MΩ and an I-V plot shows that the device is linear. However, it takes some time ($\approx$ 10 minutes) before the readings stabilize. At this point the current still drifts slightly but is stable enough for measurement purposes. Throughout the duration of the experiment, which was about 30 minutes, the drift in the current could amount to 1%. Once the reading stabilizes, the cantilevers are deflected to measure the resistance change. We apply a constant bias and measure the current before any strain is applied. The cantilever is then deflected by 0.5mm and the current is read. The cantilever is then unloaded again to ensure that the current has not drift.

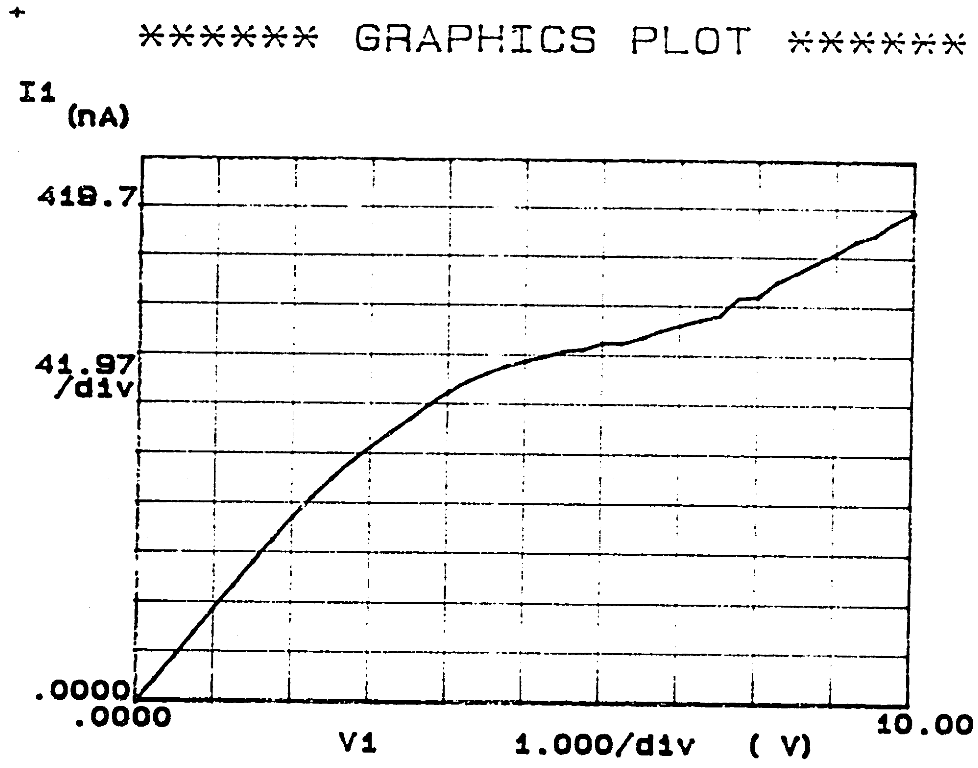

FIGURE 4-5: I-V Plot of Leakage Current

Table 4-1: Gage Factors for Mechanically Polished Wafer

Sample	G_{par}	G_{per}	G_s
# 1	143.5	-21.5	-49.5
# 2	138	-15.3	-51.6

Table 4-2: Gage Factors for ZMR Wafer

G_{par}	G_{per}	G_s
-63.1	-22.5	-6.1

The deflections are done in increments of 0.5mm up to 3.5mm, corresponding to a maximum strain of 8.8×10^{-4}. The change in resistance is then given by $\frac{I_o-I_F}{I_F}$ where I_o and I_F are the current before and during deflection. Figure 4-6 shows the change in resistance vs. strain plots of two samples that were measured and Table 4-1 shows their corresponding gage factors. The difference in these values can be accounted for by the inaccuracies in the measurements of the parameters given by equation 4.1.

4.3.3 ZMR Wafer

These laser recrystallized wafers have a 1μm dielectrically isolated film and are n-type with a 1.2μm thick oxide. The measured resistance is approximately 13MΩ and has a linear I-V characteristic. The resistors on this wafer also require some time to stabilize and the same method described in the above section is applied in the measurement of the gage factors. Only one of the seven cantilevers could be used in the processed wafer because the rest fractured during the diesaw and the wire bonding stage. Figure 4-7 shows the plots of the change in resistance vs. strain for the single cantilever and the gage factors are listed in Table 4-2. These values are lower than what is expected [28] of single crystal silicon for this low level of doping. Other reports [49, 50] also confirm this observation which is due to the imperfect crystalline structure of the film and the grain boundaries that still exist. The gage factors are therefore in between that found in polysilicon and single crystal films, depending on the conditions of the crystallization process.

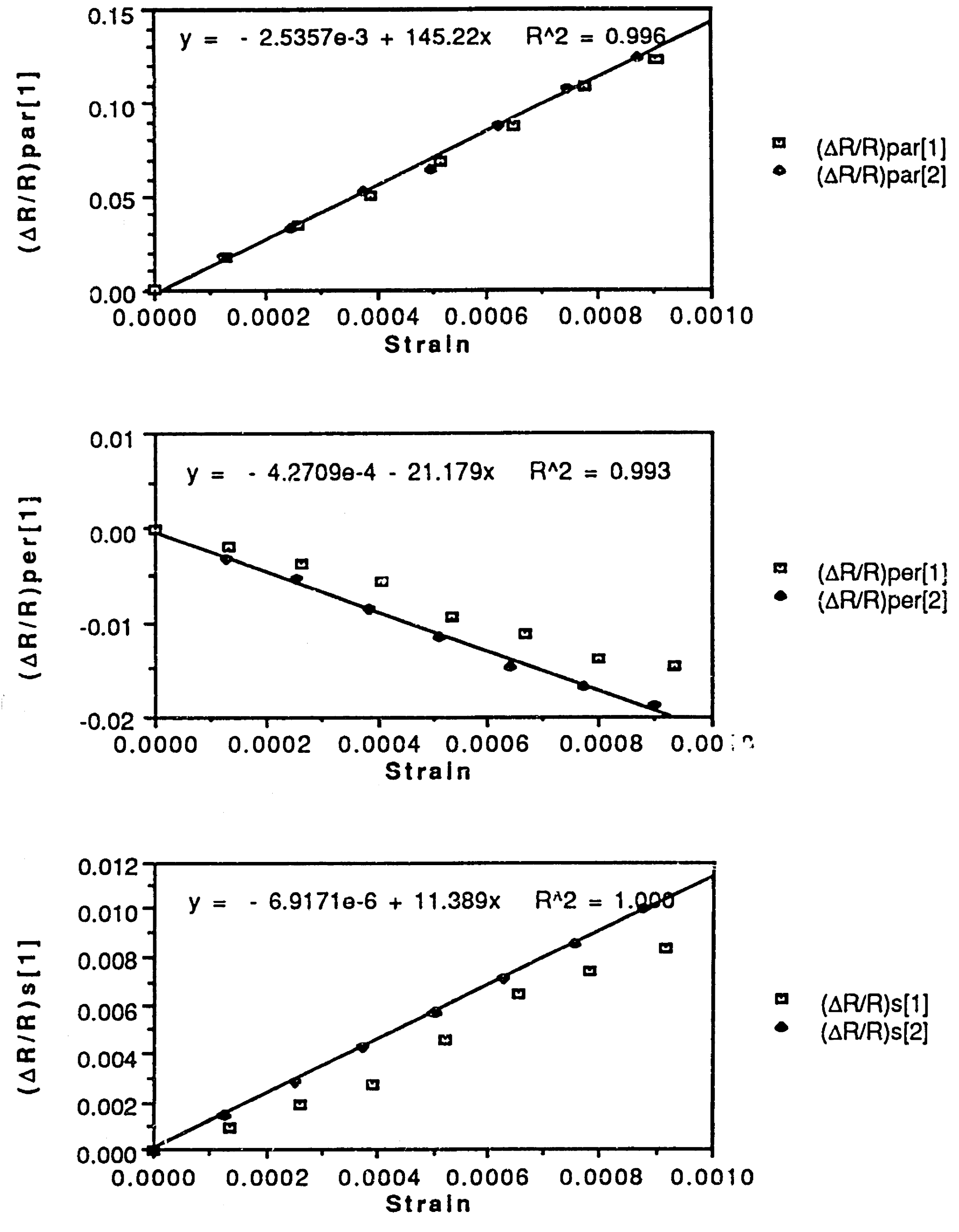

FIGURE 4-6: Change in Resistance vs. Strain Plots for Mechanically Polished Wafer

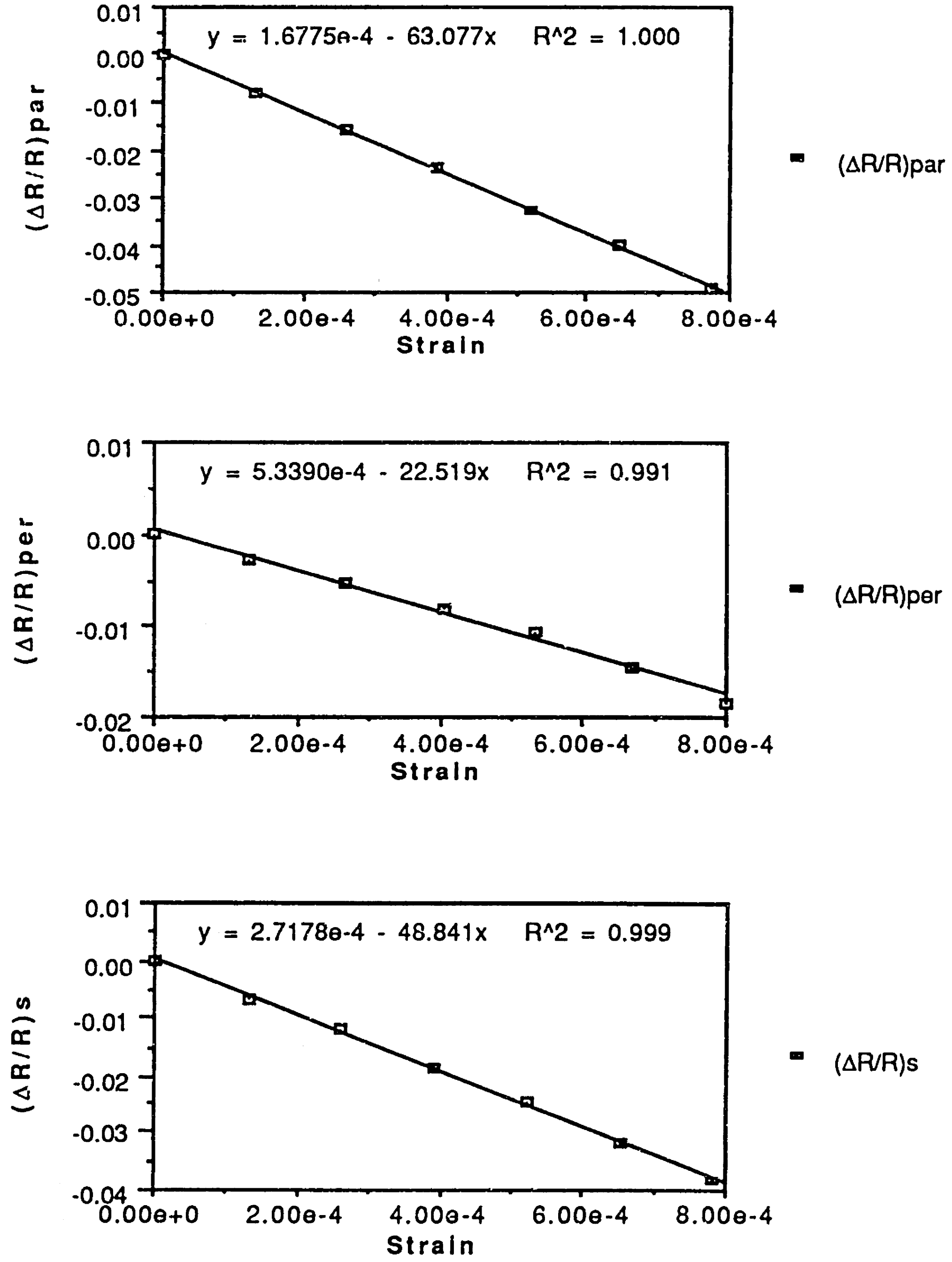

FIGURE 4-7: Change in Resistance vs. Strain Plots for ZMR Wafer

5

Sensor Testing and Calibration

Two categories of experiments are described in this chapter. The first is failure testing, which is to determine whether the sensor can be subjected to the environment in which it is designed for. The second is the calibration of the sensor itself. These two experiments are presented in two separate sections.

5.1 Failure Testing

5.1.1 Packaging

The goal of this experiment is to investigate the structural integrity of the floating-element after being exposed to an environment of elevated temperatures and pressures and in the presence of viscous liquid flow. These conditions are commonly found in a polymer extruder and a packaging scheme is required to insert the sensor into the wall of the extruder. This is accomplished by modifying the Dynasco pressure transducer that is currently being used in the extruder. Figure 5-1 shows a Dynasco transducer which consists of a rod that screws into the wall of an extruder. The tip has a diaphragm that deflects under applied pressure. The mechanical response is converted to electrical signals and wires are routed out through the center of the rod, which is partially hollow. In order to package the shear- sensor, we have a rod of the same dimensions with a milled recess at the tip so that the chip could be mounted flush with the surface. Figure 5-2 shows the dimensions of the recess located at the tip of the rod.

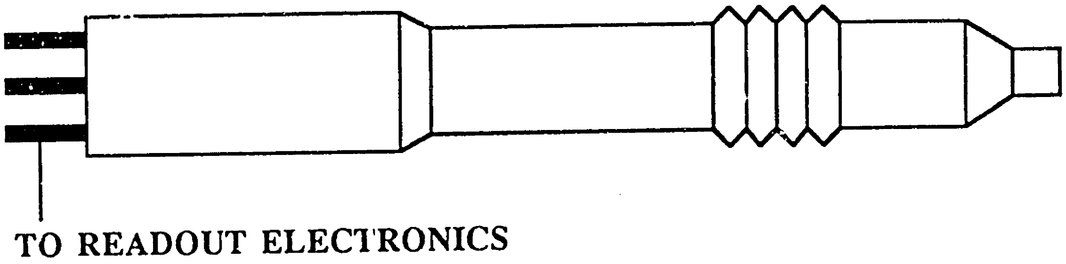

FIGURE 5-1: Side View of a Dynasco Pressure Transducer

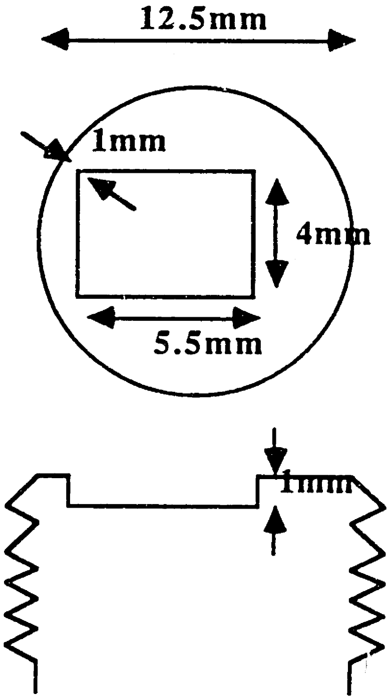

FIGURE 5-2: Physical Dimensions of the Milled Recess

Two such rods made of stainless steel were machined by 3M. A small amount of high temperature epoxy is applied to the recess, filling up half the depth and the sensor chip is placed in it. A razor blade is used to press the chip so that it is level with the tip and any excess epoxy that may be displaced out of the recess is removed. The package is then allowed to cure at room temperature for 24 hours and then placed in an oven at 150°C for 10 minutes to make sure that it is fully cured. Figure 5-3 shows a photo of the packaged sensor.

At this point, no electrical response are considered and wire leads are not brought out of the bonding pads. However, this scheme is flexible enough to be adapted to include the electrical response. This can be accomplished by drilling holes through the rod and bringing in the wire leads to the tip. A wire bonder is used to connect the bonding pads to the leads and epoxy is then applied to this area to protect the wires and pads.

5.1.2 Backfill

Prior to placing the package in the extruder, the space underneath the floating-element is filled with air. In the presence of a viscous liquid, this space may not be replaced by the fluid and at high pressures the floating-element may be pressed against the handle wafer due to the compressibility of air. This 'sticking' would result in erroneous readings for the sensor. As a result we would like to backfill the gap with a suitable liquid that is less compressible. This is done by sealing the mounted chip in a chamber and evacuating the chamber with a vacuum pump. Under a low enough pressure, the air underneath the floating-element will be evacuated as well. A liquid is then introduced onto the surface of the chip and the chamber is allowed to vent back to atmospheric pressure which forces the liquid to flow underneath the element. Figure 5-4 illustrates how this was achieved. The chamber is a stainless-steel tee fitting and the bottom end of it is capped. The bend in the middle is then attached to a Alcatel vacuum pump via copper tubings and control valves. A small amount of mineral oil is introduced into the inside of the chamber and the extruder package is screwed into the opening at the top. The chamber is then pumped down. We achieved a pressure of 7 mTorr, measured using a Pirani gauge, in less than a minute. The tee is then turned around 180° so that the package is facing down such that the mineral oil will flow to the surface of the chip. The pump is turned off and the chamber is vented back

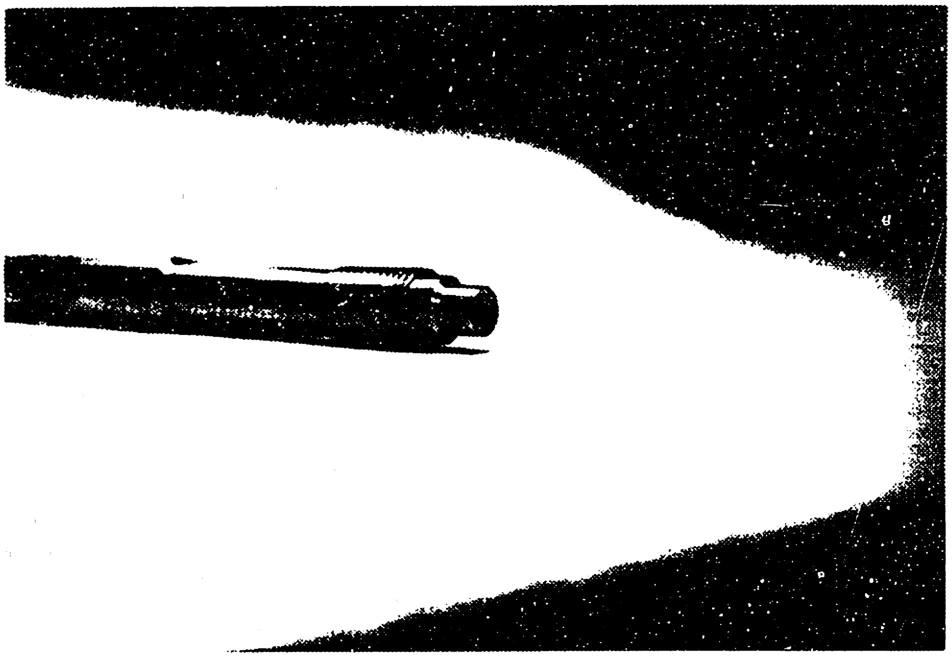

FIGURE 5-3: Photo of Packaged Sensor

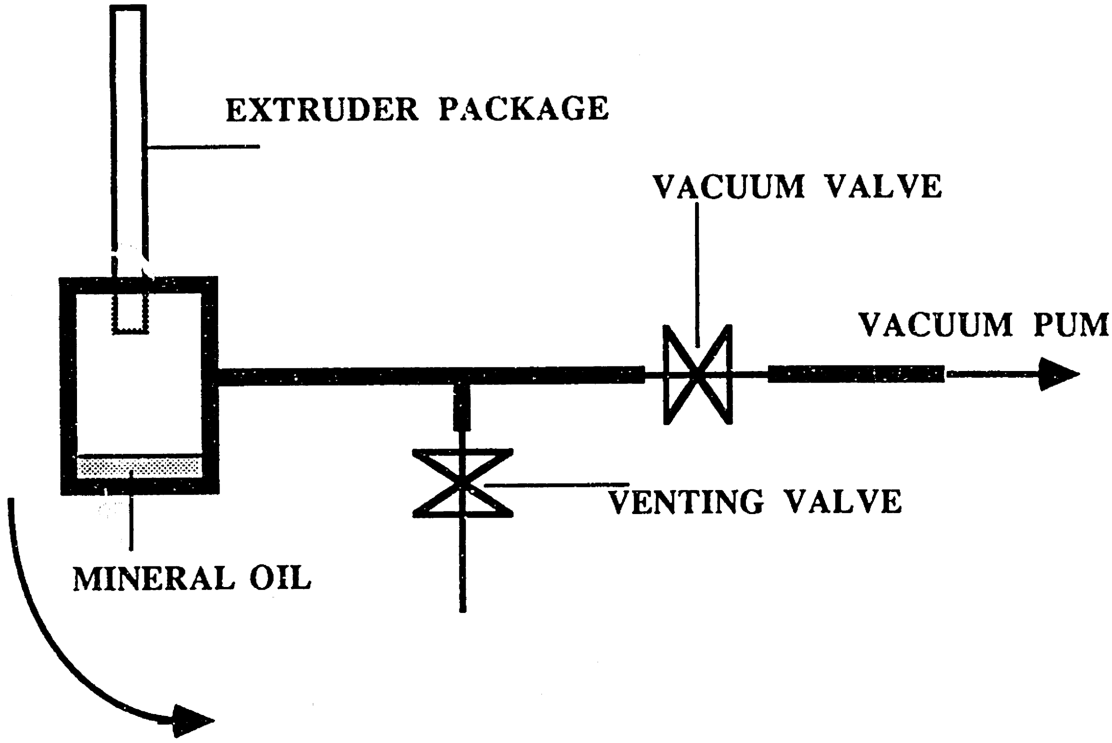

FIGURE 5-4: Apparatus Setup for the Backfilling Experiment

to atmospheric pressure. In a trial run using this system, the chip was mounted using silver paint instead of epoxy. After the backfill experiment, the chip was removed and inspected under the microscope. Using a micromanipulator, the floating-element was depressed and it could be observed that the mineral oil underneath the plate was being squeezed out via the trenches. Chips using the high temperature epoxy were then mounted on to the packages and backfilled using the same procedure. The packages are then capped to protect the chips and sent out to 3M to be inserted into an extruder.

5.1.3 Results

One of the two packages was used in the failure testing experiment. It was installed in an extruder and tested using polyethylene resin at 220 $^{\circ}C$ with the pressure ranging from 15.1 MPa to 45.5 MPa. The total time of the experiment was 50 minutes.

The package was removed, cleaned with acetone and inspected under the microscope. The floating-element, bridges and cantilevers were intact and under 100×

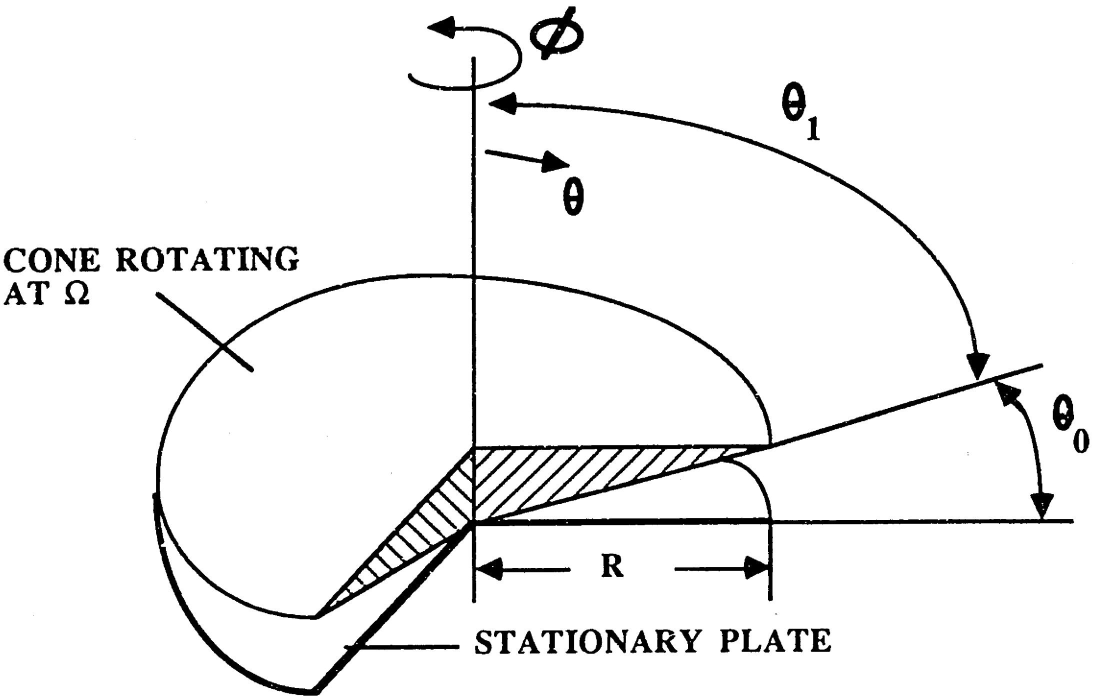

FIGURE 5-5: Cutaway View of the Cone-and-Plate Viscometer

magnification, no cracks or fracture lines were observed in these structures. The floating-element did not appear to be sticking to the substrate but some dark residue was observed in the square openings of the floating-element and in the trenches, possibly indicating the presence of the resin which has now replaced the mineral oil that had been used to backfill the chip.

5.2 Calibration

5.2.1 Design

The method used to calibrate the sensor is a cone-and-plate viscometer, shown in Figure 5-5. It consists of a rotating cone and a stationary flat plate with liquid in between. The apex of the cone is in contact with the plate and the cone spins at an angular velocity Ω. The angle between the plate and cone is θ_0 and is usually about $1/2^0$. In the analysis below, we will use spherical coordinates. The shear-stress $\tau_{\theta\phi}$ is

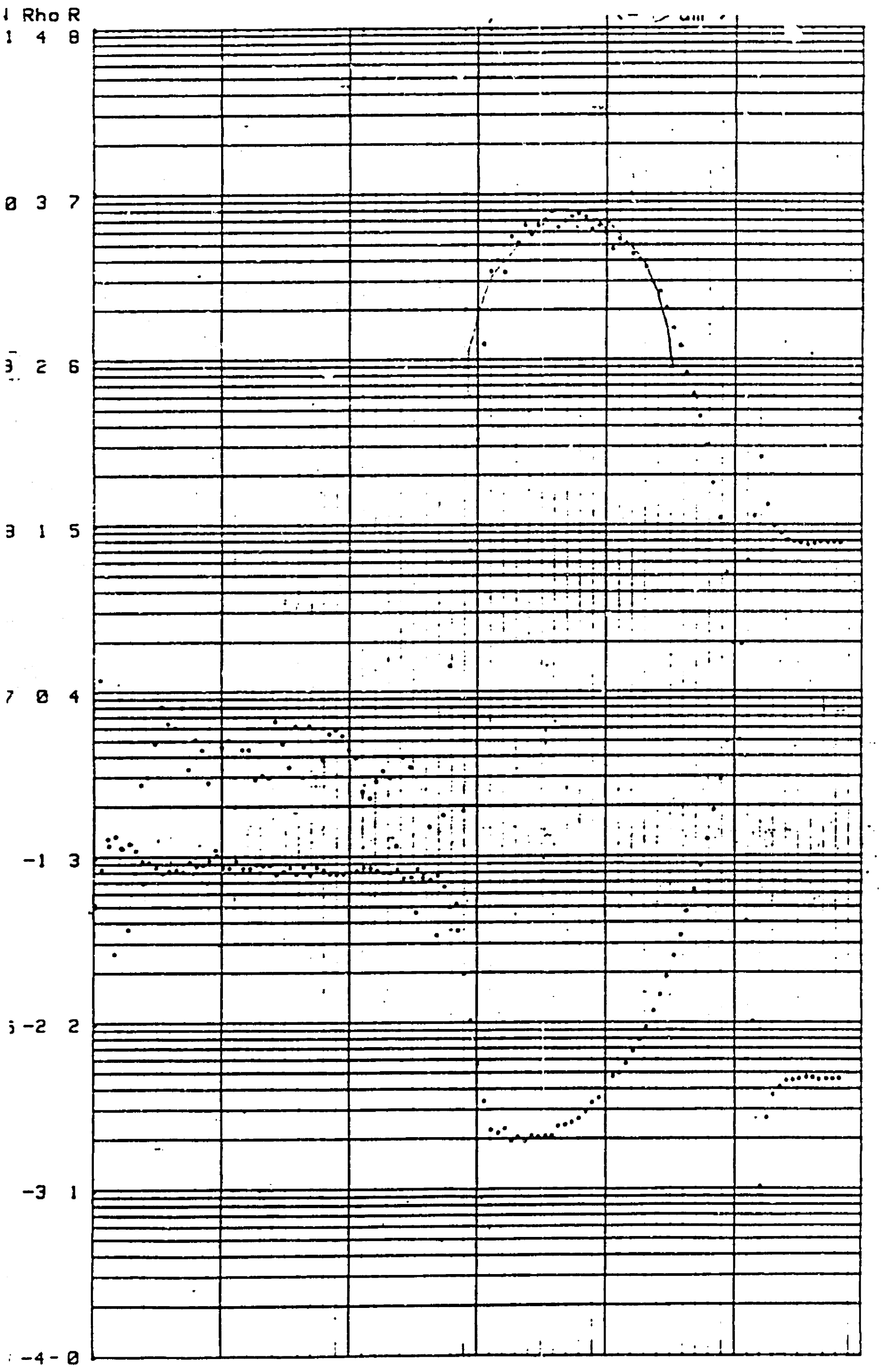

FIGURE B-1: Spreading Sheet Resistance Data

Appendix C

SUPREM Simulation

This appendix presents the results of SUPREM simulation done for the contact implants and annealing for the shear-sensor and piezoresistors. n-type wafers are implanted with arsenic at 80keV and a dose of $7 \times 10^{15} cm^{-2}$ using a resist mask. The annealing is done at $850^{o}C$ in dry O_2 for 1 hour. p-type wafers are implanted with BF_2 at 20keV and a dose of $7 \times 10^{15} cm^{-2}$ using a resist mask. Annealing is done at $900^{o}C$ in nitrogen for 30 minutes. Figure C-1 shows the results for the n-type wafers after the anneal with the line drawn at $500\AA$ representing the oxide growth during the high temperature cycle. Figure C-2 shows the corresponding result for the p-type wafers.

```
Net Chemical Impurity Profile
      14        15        16        17        18        19        20        21
  0.00 ===============================================*=======================
       !         !         !         !         !         !     *   !         !
       !         !         !         !         !         !        *!         !
  0.05 ============================================================*========*=
       !         !         !         !         !         !         !         *
       !         !         !         !         !         !         !         *
       !         !         !         !         !         !         !      *  !
       !         !         !         !         !         !         !  *      !
       !         !         !         !         !         !         !*        !
       !         !         !         !         !         !      *  !         !
       !         !         !         !         !         !*        !         !
  0.20 +---------+---------+---------+---------*---------+---------+---------+
       !         !         !      *  !         !         !         !         !
       !         !     *   !         !         !         !         !         !
       !         !*        !         !         !         !         !         !
       !         *         !         !         !         !         !         !
       !         *         !         !         !         !         !         !
       !         *         !         !         !         !         !         !
       !         *         !         !         !         !         !         !
       !         *         !         !         !         !         !         !
       !         *         !         !         !         !         !         !
       !         *         !         !         !         !         !         !
  0.40 +---------*---------+---------+---------+---------+---------+---------+
       !         *         !         !         !         !         !         !
       !         *         !         !         !         !         !         !
       !         *         !         !         !         !         !         !
       !         *         !         !         !         !         !         !
       !         *         !         !         !         !         !         !
       !         *         !         !         !         !         !         !
       !         *         !         !         !         !         !         !
       !         *         !         !         !         !         !         !
       !         *         !         !         !         !         !         !
       !         *         !         !         !         !         !         !
  0.60 +---------*---------+---------+---------+---------+---------+---------+
       !         *         !         !         !         !         !         !
       !         *         !         !         !         !         !         !
       !         *         !         !         !         !         !         !
       !         *         !         !         !         !         !         !
       !         *         !         !         !         !         !         !
```

Figure C-1: Arsenic Implant

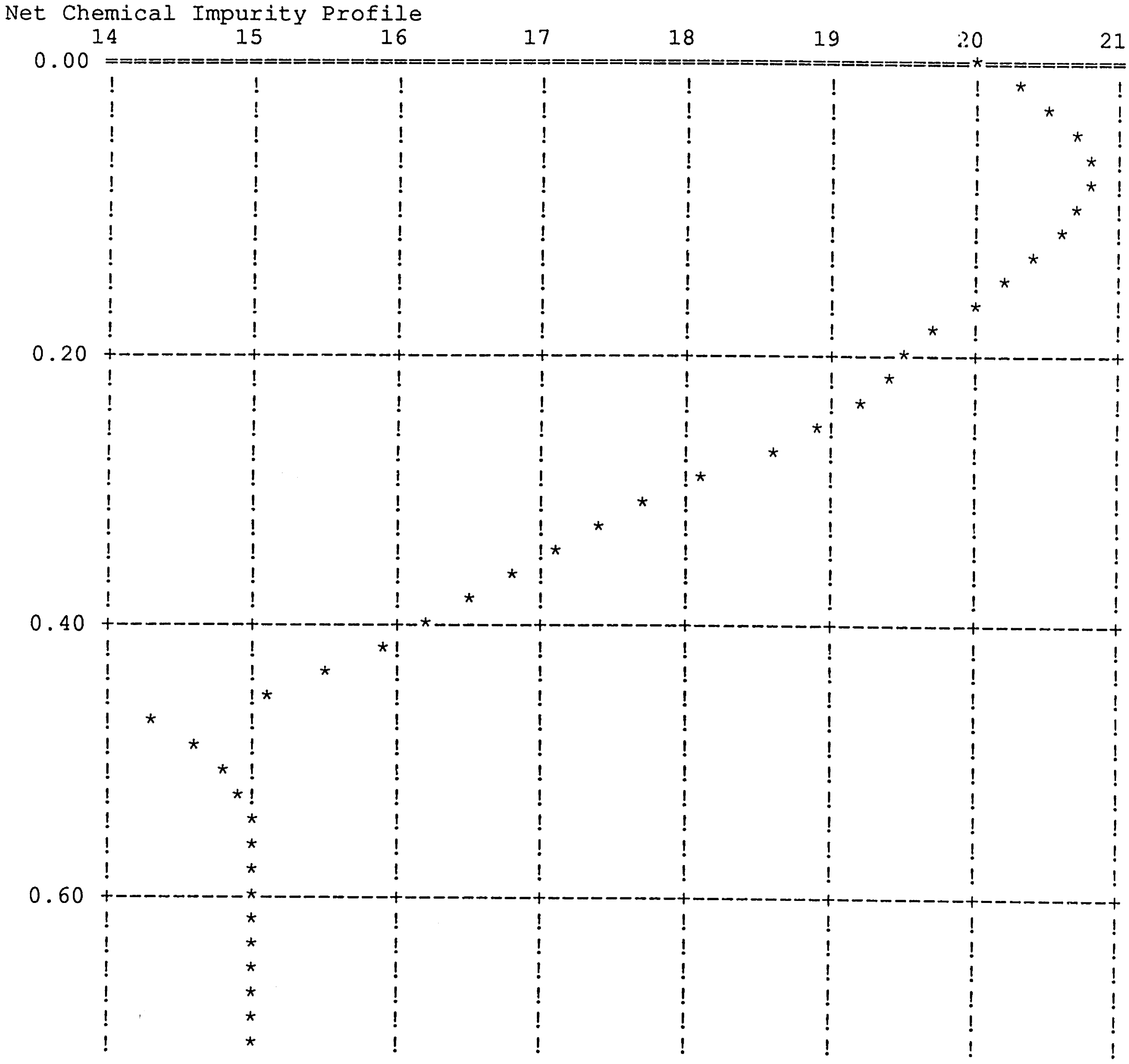

FIGURE C-2: BF_2 Implant

Appendix D

PECVD Deposition Parameters

This appendix presents the deposition parameters used for the deposition of SiO_x and amorphous silicon. The depositions are done with a Plasmatherm reactor in the Technology Research Laboratory (TRL) at MIT.

Table D-1: Deposition Parameters for PECVD SiO_x

SiH_4	5sccm
N_2O	110sccm
Frequency	13.56 MHz
Power	10 W
Temperature	300°C
Throttle Press.	150 mTorr
Deposition Rate	200 $\AA$

Table D-2: Deposition Parameters for Amorphous Silicon

SiH_4	20sccm
Frequency	13.56 MHz
Power	10 W
Temperature	220°C
Throttle Press.	350 mTorr
Deposition Rate	250 $\AA$

Appendix E

Plasma Etching Parameters

The parameters for the plasma etching of oxide and silicon are presented in this appendix. Recipe # 20 is the oxide plasma etch, recipe # 10 is the CCl_4 based silicon etch while recipe # 12 is the SF_6 based silicon etch. Recipe #10 and #12 are done in a LAM 490 etcher while recipe #20 is done in a LAM 590 etcher.

Table E-1: Oxide Plasma Etch. (Recipe # 20)

	Step # 1	Step # 2	Step #3	Step #4	Step #5	Step #6
Pressure	3 mTorr	3 mTorr	3 mTorr	3 mTorr	3 mTorr	3 mTorr
RF Top	0	50 W	0 W	900 W	0 W	800 W
Gap	0.5 cm	0.5 cm	0.36 cm	0.36 cm	0.38 cm	0.38 cm
O_2	100sccm	100sccm	0	0	0	0
He	200sccm	200sccm	125sccm	125sccm	125sccm	125sccm
CHF_3	0	0	30 sccm	30 sccm	28 sccm	28 sccm
CF_4	20 sccm	20 sccm	90 sccm	90 sccm	25 sccm	25 sccm
Time	Stable	6 sec	Stable	Time	Stable	Overetch

Table E-2: Silicon Plasma Etch (Recipe # 10)

	Step # 1	Step # 2	Step #3	Step #4	Step #5
Pressure	500 mTorr	500 mTorr	200 mTorr	200 mTorr	200 mTorr
RF Top	0	30 W	0 W	300 W	200 W
Gap	1.5 cm	1.5 cm	1.5 cm	1.5 cm	1.5 cm
CCl_4	0 sccm	0 sccm	130 sccm	130 sccm	130 sccm
O_2	200 sccm	200 sccm	20 sccm	20 sccm	20 sccm
He	100 sccm	100 sccm	70 sccm	70 sccm	130 sccm
Time	Stable	6 sec	Stable	Time	Overetch

Table E-3: Silicon Plasma Etch. (Recipe # 12)

	Step # 1	Step # 2	Step #3	Step #4	Step #5
Pressure	50 mTorr	450 mTorr	450 mTorr	250 mTorr	250 mTorr
RF Top	0	0 W	100 W	0 W	75 W
Gap	1.2 cm	1.2 cm	1.2 cm	1.2 cm	1.2 cm
SF_6	0 sccm	135 sccm	135 sccm	100 sccm	100 sccm
O_2	0 sccm	45 sccm	45 sccm	20 sccm	20 sccm
Time	Stable	Stable	Time	Stable	Overetch

Appendix F

Etching Selectivity Experiment

The selectivity etch ratios given in section 3.6 are determined by first patterning a silicon wafer with square patterns using the masking material and measuring the thickness of the mask, t. The wafer is then etched for a predetermined amount of time and the thickness of the resulting step is then measured, d. The mask is removed and the step is measured again, t'. All measurements are done using a Dektak. The etch ratio is then given by:

$$S = \frac{t'}{t - (d - t')} \tag{F.1}$$

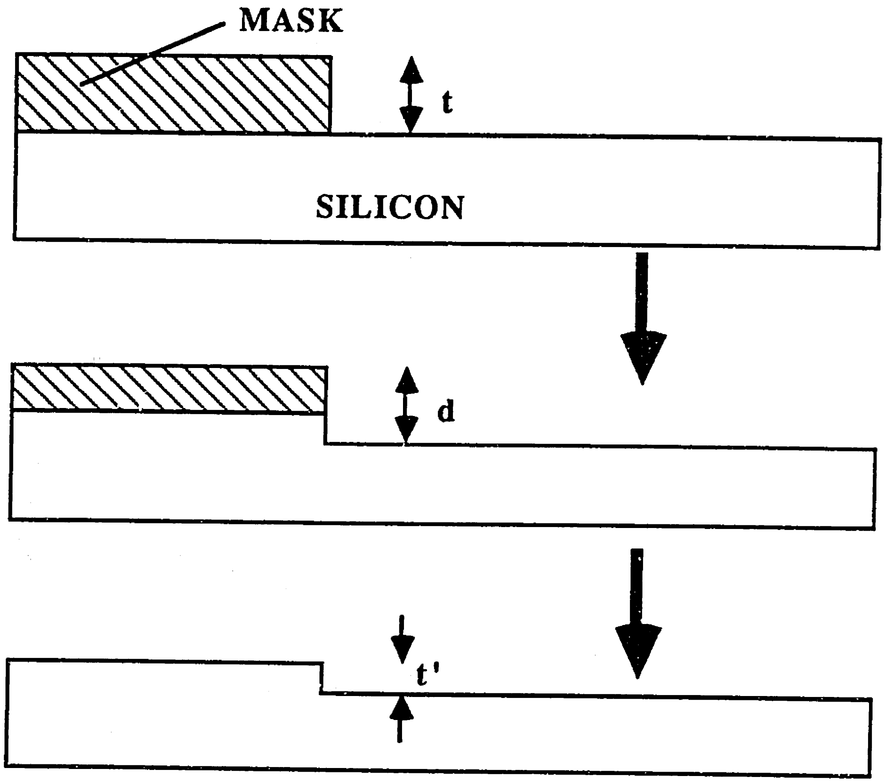

FIGURE F-1: Step Measurements to Determine Etch Selectivity

Appendix G

Torque and Velocity Equations for Viscometer

The equations derived in this appendix are used in the calibration of the sensor discussed in Chapter 5 of this thesis. The derivation is taken from Transport Phenomena by Bird, Stewart and Lightfoot. The equations are in spherical coordinates$(r,\ \theta,\phi)$ and refers to Figure 5-5. θ_0 is the angle between the cone and the stationary flat plate and θ_1 is $\pi/2 - \theta_0$. The equations are true for Newtonian fluids at 'creeping flow'.

Before we begin, we list out both the equations of motion in spherical coordinates and the components of the stress tensor for Newtonian fluids. The equations of motion in (r,θ,ϕ) are:

$$\begin{aligned}
&r - component \quad && \rho\left(\frac{\partial v_r}{\partial t} + v_r\frac{\partial v_r}{\partial r} + \frac{v_\theta}{r}\frac{\partial v_r}{\partial \theta} + \frac{v_\phi}{r sin\theta}\frac{\partial v_r}{\partial \phi} - \frac{v_\theta^2+v_\phi^2}{r}\right) \\
& && = -\frac{\partial p}{\partial r} - \left(\frac{1}{r^2}\frac{\partial}{\partial r}(r^2\tau_{rr}) + \frac{1}{r sin\theta}\frac{\partial}{\partial \theta}(\tau_{r\theta} sin\theta) + \frac{1}{r sin\theta}\frac{\partial \tau_{r\phi}}{\partial \phi} - \frac{\tau_{\theta\theta}+\tau_{\phi\phi}}{r}\right) + \rho g_r \\
&\theta - component \quad && \rho\left(\frac{\partial v_\theta}{\partial t} + v_r\frac{\partial v_\theta}{\partial r} + \frac{v_\theta}{r}\frac{\partial v_\theta}{\partial \theta} + \frac{v_\phi}{r sin\theta}\frac{\partial v_\theta}{\partial \phi} + \frac{v_r v_\theta}{r} - \frac{v_\phi^2 cot\theta}{r}\right) \\
& && = -\frac{1}{r}\frac{\partial p}{\partial \theta} - \left(\frac{1}{r^2}\frac{\partial}{\partial r}(r^2\tau_{r\theta}) + \frac{1}{r sin\theta}\frac{\partial}{\partial \theta}(\tau_{\theta\theta} sin\theta) + \frac{1}{r sin\theta}\frac{\partial \tau_{\theta\phi}}{\partial \phi} + \frac{\tau_{r\theta}}{r} - \frac{cot\theta}{r}\tau_{\phi\phi}\right) + \rho g_r \\
&\phi - component \quad && \rho\left(\frac{\partial v_\phi}{\partial t} + v_r\frac{\partial v_\phi}{\partial r} + \frac{v_\theta}{r}\frac{\partial v_\phi}{\partial \theta} + \frac{v_\phi}{r sin\theta}\frac{\partial v_\phi}{\partial \phi} + \frac{v_r v_\phi}{r} + \frac{v_\phi v_\theta cot\theta}{r}\right) \\
& && = -\frac{1}{r sin\theta}\frac{\partial p}{\partial \phi} - \left(\frac{1}{r^2}\frac{\partial}{\partial r}(r^2\tau_{r\phi}) + \frac{1}{r}\frac{\partial \tau_{\phi\phi}}{\partial \theta} + \frac{1}{r sin\theta}\frac{\partial \tau_{\phi\phi}}{\partial \phi} + \frac{\tau_{r\phi}}{r} - \frac{2cot\theta}{r}\tau_{\theta\phi}\right) + \rho g_\phi
\end{aligned} \tag{G.1}$$

The components of the stress tensor are:

$$\tau_{rr} = -\mu\left[2\frac{\partial v_r}{\partial r} - \frac{2}{3}(\nabla . v)\right]$$

$$\tau_{\theta\theta} = -\mu\left[2\left(\frac{1}{r}\frac{\partial v_\theta}{\partial\theta} + \frac{v_r}{r}\right) - \frac{2}{3}(\nabla . v)\right]$$

$$\tau_{\phi\phi} = -\mu\left[2\left(\frac{1}{rsin\theta}\frac{\partial v_\phi}{\partial\phi} + \frac{v_r}{r} + \frac{v_\theta cot\theta}{r}\right) - \frac{2}{3}(\nabla . v)\right]$$

$$\tau_{r\theta} = \tau_{\theta r} = -\mu\left[r\frac{\partial}{\partial r}\left(\frac{v_\theta}{r}\right) + \frac{1}{r}\frac{\partial v_r}{\partial\theta}\right]$$

$$\tau_{\theta\phi} = \tau_{\theta\phi} = -\mu\left[\frac{sin\theta}{r}\frac{\partial}{\partial\theta}\left(\frac{v_\phi}{sin\theta}\right) + \frac{1}{rsin\theta}\frac{\partial v_\theta}{\partial\phi}\right]$$

$$\tau_{\phi r} = \tau_{r\phi} = -\mu\left[\frac{1}{rsin\theta}\frac{\partial v_r}{\partial\phi} + r\frac{\partial}{\partial r}\left(\frac{v_\phi}{r}\right)\right]$$

$$(\nabla . v) = \frac{1}{r^2}\frac{\partial}{\partial r}(r^2 v_r) + \frac{1}{rsin\theta}\frac{\partial}{\partial\theta}(v_\theta sin\theta) + \frac{1}{rsin\theta}\frac{\partial v_\phi}{\partial\phi} \tag{G.2}$$

If the flow is entirely tangential, then v_ϕ is a function of r and θ and $v_r = v_\theta = 0$. From the stress equations, the only non-zero terms of τ are $\tau_{\theta\phi}$ and $\tau_{r\phi}$. Therefore, the three components of the equation of motion are

$$\begin{array}{ll} r - component & -\rho\frac{v_\phi^2}{r} = -\frac{\partial p}{\partial r} \\ \theta - component & -\rho cot\theta\frac{v_\phi^2}{r} = -\frac{1}{r}\frac{\partial p}{\partial\theta} \\ \phi - component & 0 = \left(\frac{1}{r^2}\frac{\partial}{\partial r}(r^2\tau_{r\phi}) + \frac{1}{r}\frac{\partial\tau_{\theta\phi}}{\partial\theta} + \frac{\tau_{r\phi}}{r} + 2cot\theta\frac{\tau_{\theta\phi}}{r}\right) \end{array} \tag{G.3}$$

Using the assumption of 'creeping flow', terms containing v_ϕ^2 are negligible and can be set to zero. Therefore, only the ϕ-component of the equation of motion needs to be considered. Next, we postulate that the velocity distribution will be of the form $v_\phi(r,\theta) = rf(\theta)$ since it satisfies the boundary conditions at both $\theta = 0$ and $\theta = \pi/2$. By this hypothesis that the angular velocity v_ϕ/r is independent of r, we find from equation G.2 that $\tau_{r\phi} = 0$.

When $\tau_{r\phi}$ is set to zero, we get the following ordinary differential equation for $\tau_{\theta\phi}$:

$$\frac{d\tau_{\theta\phi}}{d\theta} = -2\tau_{\theta\phi}cot\theta \tag{G.4}$$

Integration of this equation gives

$$\tau_{\theta\phi} = \frac{C_1}{sin^2\theta} \tag{G.5}$$

where C_1 is an integration constant. We can evaluate C_1 from the boundary condition at $\theta = \pi/2$ that the torque transmitted by the fluid to the plate is known to be $\mathcal{T}$. Therefore,

$$\begin{aligned}\mathcal{T} &= \int_0^{2\pi} \int_0^R \tau_{\theta\phi}|_{\theta=\pi/2} r^2 dr d\phi \\ &= (2\pi)\left(\frac{R^3}{3}\right)\left(\frac{C_1}{sin^2\pi/2}\right)\end{aligned}$$

Combining equations G.5 and G.6 then gives

$$\tau_{\theta\phi} = \frac{3\mathcal{T}}{2\pi R^3 sin^2\theta} \tag{G.6}$$

From equation G.2 we obtain the relationship between $\tau_{\theta\phi}$ and the gradient of v_ϕ/r. Inserting this expression into equation G.6, we obtain the following ordinary differential equation for the local angular velocity v_ϕ/r:

$$-\mu sin\theta \frac{d}{d\theta}\left(\frac{v_\phi/r}{sin\theta}\right) = \frac{3\mathcal{T}}{2\pi R^3 sin^2\theta} \tag{G.7}$$

By separating variables and integrating, we get the angular velocity distribution:

$$\frac{v_\phi}{r} = \frac{3\mathcal{T}}{4\pi R^3\mu}\left[cot\theta + \frac{1}{2}\left(ln\frac{1+cos\theta}{1-cos\theta}\right)sin\theta\right] + C_2 \tag{G.8}$$

The constant of integration C_2 is zero since at $\theta = \pi/2$, $v_\phi = 0$.

In order to relate the angular velocity to the rotation of the cone Ω we first evaluate equation G.8 for the special case that $\theta = \theta_1 = \pi/2 - \theta$ and $v_\phi = \Omega r sin\theta_1$.

$$\Omega sin\theta_1 = \frac{3\mathcal{T}}{4\pi R^3\mu}\left[cot\theta_1 + \frac{1}{2}\left(ln\frac{1+cos\theta_1}{1-cos\theta_1}\right)sin\theta_1\right] \tag{G.9}$$

Dividing equation G.8 by equation G.9 then causes $\mathcal{T}$ to be eliminated, and thereby we get v_ϕ in terms of Ω:

$$\frac{v_\phi}{r} = \Omega sin\theta_1\left[\frac{cot\theta + \frac{1}{2}\left(ln\frac{1+cos\theta}{1-cos\theta}\right)sin\theta}{cot\theta_1 + \frac{1}{2}\left(ln\frac{1+cos\theta_1}{1-cos\theta_1}\right)sin\theta_1}\right] \tag{G.10}$$

Based on these equations it can be seen that a)only one stress component $\tau_{\theta\phi}$ is important, b)the magnitude of $\tau_{\theta\phi}$ is very nearly constant throughout the fluid and c) end effects can be almost completely eliminated.

Appendix H

Calibration Package Design

The physical dimensions of the plates used for the calibration of the sensor are given in this chapter. The material is aluminum and Figure H-1 shows the dimensions for the bottom plate. Figure H-2 shows the dimensions for the top plate which has a milled recess for the mounting of the chip. The positioning of the recess and holes for the wire feedthroughs relative to the rest of the plate is given in Figure H-3.

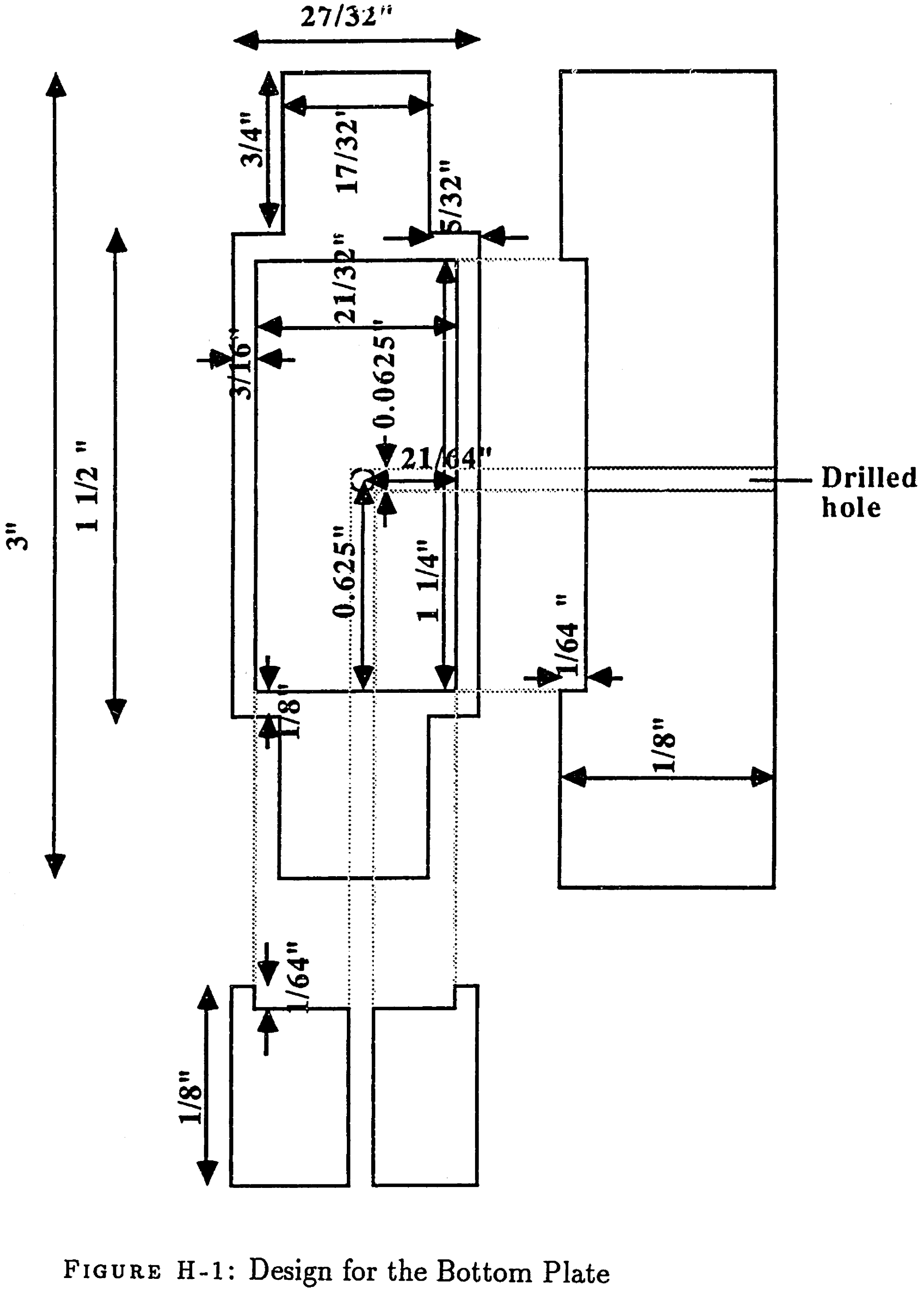

FIGURE H-1: Design for the Bottom Plate

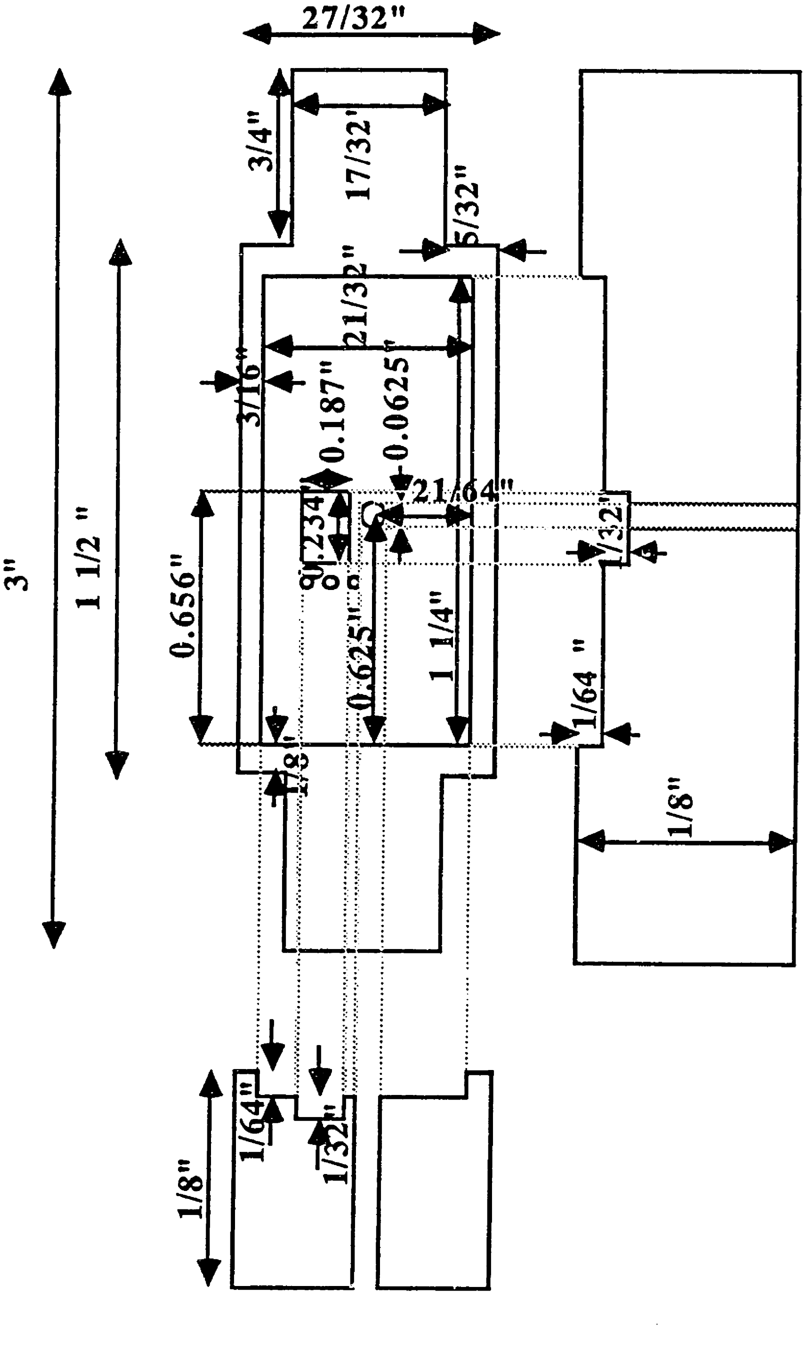

FIGURE H-2: Design for the Top Plate

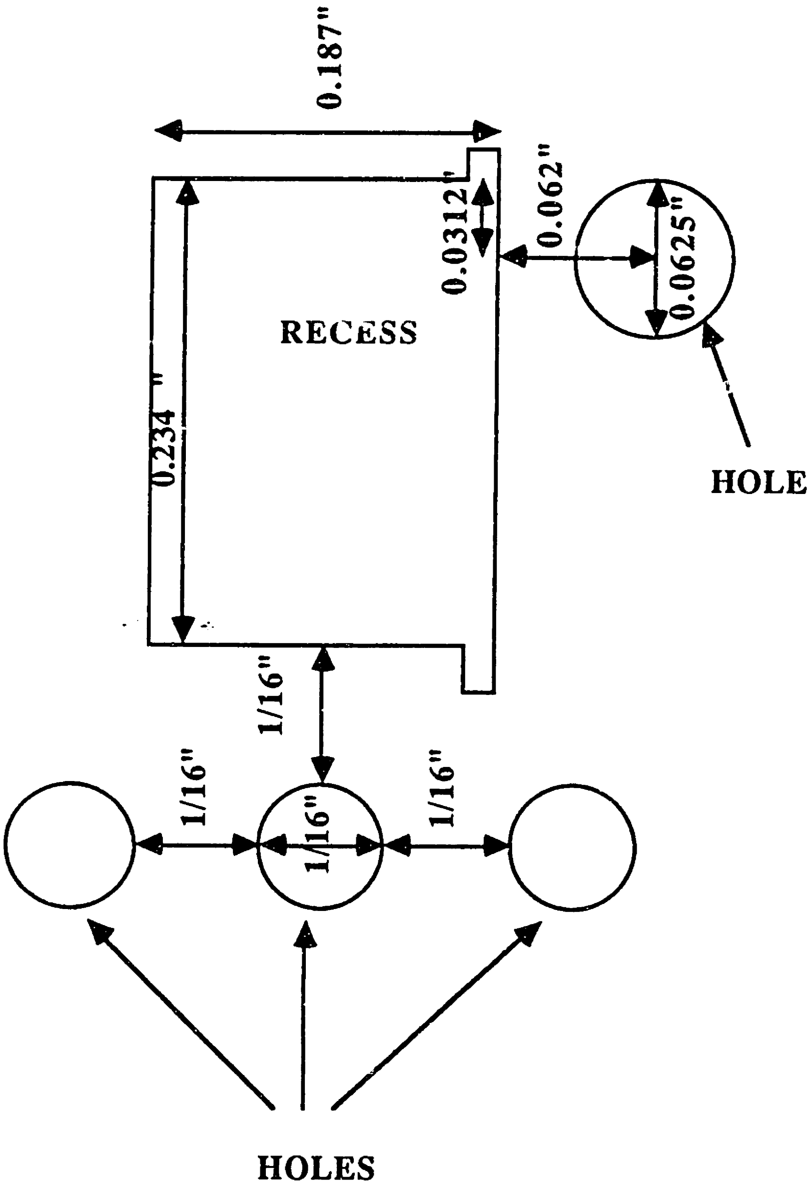

FIGURE H-3: Positions of the Recess and Holes

Bibliography

[1] M. A. Schmidt. *Microsensors for the Measurement of Shear Forces in Turbulent Boundary Layers.* PhD thesis, Massachusetts Institute of Technology, 1988.

[2] T. J. Hanratty and J. A. Campbell. Measurement of wall shear stress. In R. J. Goldstein, editor, *Fluid Mechanics Measurements.* Hemisphere Publ. Corp, 1983.

[3] K. G. Winter. An Outline of the Techniques Available for the Measurement of Skin Friction in Turbulent Boundary Layers. *Prog. Aerospace Sci.*, 18:1–57, 1977.

[4] J. B. Lasky. Wafer Bonding for Silicon-on-Insulator Technologies. *Appl. Phys. Lett.*, 48:78, 1986.

[5] J. Haisma, G. A. C. M. Spierings, U. K. P. Biermann, and J. A. Pals. Silicon-on-Insulator Wafer-Bonding Thinning Technological Evaluations. *Japanese Journal of Applied Physics*, 28:1426–1443, 1989.

[6] W. P. Maszara, G. Goetz, A. Caviglia, and J. B. McKitterick. Bonding of Silicon Wafers for Silicon-on-Insulator. *J. Appl. Phys.*, 64:4943, 1988.

[7] J. B. Price. Anisotropic Etching of Silicon with KOH-H_2O- Isopropyl Alcohol. In *Semiconductor Silicon, Electrochemical Society Softbound Proceedings Series*, pages 339–353, Princeton, NJ, USA, 1973.

[8] L. D. Clark Jr., J. L. Lund, and D. J. Edell. Cesium Hydroxide (CsOH): A Useful Etchant for Micromachining Silicon. In *Solid State Sensor and Actuator Workshop*, pages 5–8, Hilton Head Island, South Carolina, 1988.

[9] R. M. Finne and D. L. Klein. A Water-Amine-Complexing Agent System for Etching Silicon. *Journal of Electrochemical Society*, 114:965–970, 1967.

[10] M. J. Declercq, L. Gerzberg, and J. D. Meindl. Optimization of the Hydrazine-Water Solution for Anisotropic Etching of Silicon in Integrated Circuit Technology. *Journal of Electrochemical Society*, 122:545–552, 1975.

[11] M. Asano, T. Cho, and H. Muraoka. Application of Choline in Semiconductor Technology. *Electrochemical Society Ext. Abstr.*, 354:911, 1976.

[12] H. Seidel. The Mechanism of Anisotropic, Electrochemical Silicon Etching in Alkaline Solutions. In *Solid State Sensor and Actuator Workshop*, pages 86–92, Hilton Head Island, South Carolina, 1990.

[13] E. D. Palik, H. F. Gray, and P. B. Klein. A Raman Study of Etching Silicon in Aqueous KOH. *Journal of the Electrochemical Society*, 130:956–959, 1983.

[14] E. D. Palik, J. W. Faust, H. F. Gray, and R. F. Greene. Study of the Etch-Stop Mechanism in Silicon. *Journal of the Electrochemical Society*, 129:2051–2059, 1982.

[15] V. M. McNeil, S. S. Wang, K. Y. Ng, and M. A. Schmidt. An Investigation of the Electrochemical Etching of (100) Silicon in CsOH and KOH. In *Solid State Sensor and Actuator Workshop*, pages 92–97, Hilton Head Island, South Carolina, 1990.

[16] O. J. Glembocki, R. E. Stahlbush, and M. Tomkiewicz. Bias Dependent Etching of Silicon in aqueous KOH. *Journal of the Electrochemical Society*, 132:145–151, 1985.

[17] R. L. Smith, B. Kloeck, N. F. de Rooij, and S. D. Collins. The potential Dependence of Silicon Anisotropic Etching in KOH at 60 C. *Journal of Electroanalytical Chemistry and Interfacial Electrochemistry*, 238:103–113, 1987.

[18] T. Fujii, Y. Gotoh, and S. Kuroyanagi. DI-Piezoresistor by Wafer Direct Bonding. In *Technical Digest of the 7th Sensor Symposium*, pages 63–66, Japan, 1988.

[19] K. E. Petersen. Silicon as a Mechanical Material. *Proceedings of the IEEE*, 70:420–457, 1982.

[20] J. M. Gere and S. P. Timoshenko. *Mechanics of Materials.* PWS Engineering, 1984.

[21] L. Trilling and R. J. Hakkinen. The Calibration of the Stanton tube as a skin-friction meter. *Jahre Grenzschichtforschung*, 14:201–209, 1955.

[22] C. S. Smith. Piezoresistive Effect in Germanium and Silicon. *Phys. Rev.*, 94:42–49, 1954.

[23] W. P. Mason and R. N. Thurston. Use of Piezoresistive Materials in the Measurements of Displacements and Torques. *J. Acoust. Soc. Am.*, 29:1096–1101, 1957.

[24] W. G. Pfann and R. N. Thurston. Semiconducting Stress Transducers Utilizing the Transverse and Shear Piezoresistance Effects. *J. Appl. Phys.*, 10:2008–2019, 1962.

[25] Y. Kanda. A Graphical Representation of the Piezoresistive Coefficients in Silicon. *IEEE Transactions on Electron Devices*, ED-29:64–70, 1982.

[26] W. P. Mason. *Crystal Physics of Interaction and Processes.* Academic Press, New York, 1966.

[27] J. F. Nye. *Physical Properties of Crystals.* Clarendon Press, Oxford, Great Britain, 1957.

[28] O. N. Tufte, P. W. Chapman, and D. Long. Piezoresistive Properties of Silicon Diffused Layers. *J. Appl. Phys.*, 34:313–318, 1963.

[29] S. Sze. *Physics of Semiconductor Devices.* John Wiley & Sons, New York, New York, 1981.

[30] Y. Onuma and K. Sekiya. Piezoresistive Properties of Polycrystalline Silicon Thin Films. *Jap. J. Appl. Phys.*, 11:20–23, 1972.

[31] J. Y. W. Seto. Piezoresistive Properties of Polycrystalline Silicon. *J. Appl. Phys.*, 47:4780–4783, 1976.

[32] H. Seidel. The Mechanism of Anisotropic Silicon Etching and its Relenace for Micromachining. In *Proceeding of 4th International Conference on Solid-State Sensors and Actuators- Transducers '87*, pages 120–125, Tokyo, Japan, 1987.

[33] L. D. Clark Jr. and D. J. Edell. KOH:H_2O Etching of (110)Si, (111)Si, SiO_2, and Ta: An Experimental Study. In *IEEE Micro Robots and Teleoperators Workshop*, Hyannis(Cape Cod), Massachusetts, 1987.

[34] H. Muraoka, T. Ohashi, and Y. Sumitomo. Controlled Preferential Etching Technology. In H. R. Huff and R. R. Burghess, editors, *Semiconductor Silicon*, pages 327–338. Princeton, 1973.

[35] H. J. A. van Dijk and J. de Jange. Preparation of Thin Silicon Crystals by Electrochemical Thinning of Epitaxially Grown Structures. *J. Electrochemical Society:Solid-State Science*, 117:553–554, 1970.

[36] Sorab K. Ghandhi. *VLSI Fabrication Principles.* John Wiley & Sons, 1983.

[37] M. A Huff, M. S. Mettner, T. A. Lober, and M. A. Schmidt. A Pressure-Balanced Electrostatically-Actuated Microvalve. In *Solid State Sensor and Actuator Workshop*, pages 123–127, Hilton Head Island, South Carolina, 1990.

[38] S. P. Timoshenko. *Theory of Plates and Shells.* McGraw-Hill, New York, 1940.

[39] Y. C. Tai. PhD thesis, University of California-Berkeley, 1989.

[40] S. Wolf and R. N. Tauber. *Silicon Processing for the VLSI Era.* Lattice Press, 1987.

[41] M. Ameen, M. Monfils, Z. Hasan, and D. Gates. Silicon Trench Etching Made Easy. *Semiconductor International*, pages 122–128, September 1988.

[42] G. K. Herb, D. J. Reiger, and K. Shields. *Solid State Technology*, page 109, October 1987.

[43] C. M. Horowitz. *IEEE Transactions on Electron Devices*, ED-28:1320, 1981.

[44] D. W. Hess. *Solid State Technology*, page 192, April 1981.

[45] D. Burns. *Micromechanics of Integrated Sensors and the Planar Processed Pressure Transducer.* PhD thesis, University of Wisconsin, 1988.

[46] R. D. Cook and W. C. Young. *Advanced Mechanics of Materials.* Macmillan, New York, 1985.

[47] D. G. Rivenbark. Measurement and analysis of silicon direct-bonded piezoresistors. S.B. Thesis, 1990. Massachusetts Institute of Technology.

[48] M. A. Schmidt and M. A. Huff, 1990. Private Communications.

[49] H. Guckel and D. W. Burns. Laser-Recrystallized Piezoresistive Micro-Diaphragm Sensor. In *3rd International Conference on Solid-State Sensors and Actuators (Transducers '85)*, pages 182–185, Philadelphia, PA, 1985.

[50] J. Detry, D. Koneval, and S. Blackstone. A Comparison of Piezoresistance in Polysilicon, Laser Recrystallized Polysilicon and Single Crystal Silicon. In *3rd International Conference on Solid-State Sensors and Actuators (Transducers '85)*, pages 278–280, Philadelphia, PA, 1985.

[51] R. B. Bird, W. E. Stewart, and E. N. Lightfoot. *Transport Phenomena.* John Wiley & Sons, 1960.

[52] W. S. Fong, W. A. Peters, and J. B. Howard. Apparatus for determining high-temperature, high-pressure coal plastic behavior under rapid heating conditions. *Rev. Sci. Instruments*, 56(4):586–591, 1985.